Doctoral Thesis

For obtaining the Doctoral Degree
in the field of Optical Engineering from the

Technical University of Catalonia
UPC-BarcelonaTech

Department of Optics and Optometry
Faculty of Optics and Optometry

Device and Strategy for Surface Energy Measurement

Author:

Noemí Domínguez Álvarez

Thesis Directors:

Dr. José Arasa Martí
Dr. Cristina García Favrot

Terrassa, 2018

UNIVERSITAT POLITÈCNICA DE CATALUNYA
BARCELONATECH
Escola de Doctorat

Assessment results for the doctoral thesis

Academic year:

Full name

Doctoral programme

Structural unit in charge of the programme

Decision of the committee

In a meeting with the examination committee convened for this purpose, the doctoral candidate presented the topic of his/her doctoral thesis entitled _____.

Once the candidate had defended the thesis and answered the questions put to him/her, the examiners decided to award a mark of:

☐ FAIL ☐ PASS ☐ GOOD ☐ EXCELLENT

(Full name and signature) Chairperson	(Full name and signature) Secretary	
(Full name and signature) Member	(Full name and signature) Member	(Full name and signature) Member

_____, _____

The votes of the members of the examination committee were counted by the Standing Committee of the Doctoral School, and the result is to award the CUM LAUDE DISTINCTION:

☐ YES ☐ NO

(Full name and signature)	(Full name and signature)

Barcelona, _____

International doctorate mention

- As the secretary of the examination committee, I hereby state that the thesis was partly (at least the summary and conclusions) written and presented in a one of the languages commonly used in scientific communication in the relevant field of knowledge, which must not be an official language of Spain. This rule does not apply to stays, reports and experts from a Spanish-speaking country.

(Full name and signature)

Agradecimientos

En primer lugar, me gustaría agradecer a mi director de tesis, Josep, por la confianza depositada en mi para llevar a cabo esta tesis, por sus consejos, por transmitirme tantísimos conocimientos y por su apoyo moral en los momentos de montaña rusa. Y a Cristina, por todo el apoyo incondicional que me has dado durante este tiempo y otros tantos conocimientos experimentales que me has transmitido.

Agradezco a SnellOptics por darme esta oportunidad para poder crecer académica, profesional y personalmente. A Carles, por haber confiado en mí para llevarlo a cabo, por sus consejos y su apoyo durante estos años. A Pau y Manel, por compartir risas y sufrimiento durante este tiempo y también a Carme y Patri, que indirectamente forman parte de este pequeño gran equipo que somos.

Al TWI, por darme la oportunidad de realizar la estancia en el extranjero y de acogerme como si fuera una más de su equipo. A Géraldine, Alan, Nadia, Eu, Marta, Angelo y al resto del grupo de recubrimientos que me dejo, gracias por enseñarme tanto y ayudarme durante esos meses.

Al equipo de I+D de Sensofar Tech, especialmente a Carlos Bermúdez. Gracias de verdad por la paciencia y dedicación con la que me has ayudado y por hacer fácil lo que parecía imposible.

Gracias a María, por ser la mejor landlady que pude tener en Cambridge, por las guías turísticas y los grandes momentos que me hiciste pasar. Y a Juan. Mi 30 cumpleaños no habría sido lo mismo sin vosotros.

A mi madre, porque de verdad, sin ella esto no podría haber sido posible. Gracias por haberme apoyado siempre, en todo, por animarme a seguir adelante por muy duro y complicado que sea el camino y por haberme enseñado a ser quien soy.

A Rubén, por apoyarme siempre y ayudarme en todo lo que ha estado a su alcance. Por aguantar mis ataques de ira y estrés e intentar sacarme siempre una sonrisa. Por tu tranquilidad y serenidad en los momentos críticos y por compartir tu vida conmigo.

A Bea, porque we were born this way y nunca se está sola en el camino. Gracias por compartir esa locura que nos caracteriza y por dejarme que cuente siempre contigo, para lo bueno y para lo malo.

Y finalmente a mis amigos y a mi familia, por todos los buenos momentos que me habéis hecho pasar y por hacerme ver que puedo con todo, Luís, Íngrid, Jesús, Lidia, Noelia, Josema, Miguel, Laia, Javi, Arnau, Cristina S., Deivid, Fina, Marce, Nina, Raúl, y a los que me dejo, a todos, gracias.

Supervisors' Certificate

Dr. José Arasa Martí and Dr. Cristina García Favrot,

CERTIFY

that the work reported in the thesis entitled

Device and strategy for surface energy measurements

which is submitted by Noemí Domínguez Álvarez in fulfilment of the requirements for the degree of Doctor with the international Doctorate mention by the Universitat Politècnica de Catalunya (UPC) has been carried out under our supervision within the framework of the PhD program in Optical Engineering of the same university.

_____ _____

José Arasa Martí Cristina García Favrot

Contents

Contents V

List of figures IX

List of tables XV

1. Introduction 1

1.1. Introduction to surface energy 2

1.2. Goals 5

1.3. Ph.D. Thesis structure 6

2. State of the knowledge in the field 9

2.1. Introduction 9

2.2. State of the art 9

2.1.1 Contact angle calculation methods 9

2.2.1. Surface energy determination methods 18

2.2.2. Measurement techniques used by profilometers 23

2.2.2.1. Confocal technique 25

2.2.2.2. Interferometric technique 27

2.3. Benchmarking 32

2.3.1. Suppliers and devices to perform contact angle measurement and surface energy evaluation 32

2.3.2. Suppliers and devices to perform 3D non-contact profilometry measurements 35

3. Roughness and surface energy 39

3.1. Introduction 39

3.2. The Wenzel model 40

3.3. The Cassie Baxter model 44

3.4. Summary 50

4. Proposed mathematical method for measuring the contact angle 51

4.1. Introduction 51

4.2. Developed mathematical models to calculate the contact angle 52

4.2.1. Contact angle calculation with h and L 53

4.2.2. Contact angle calculation with h and V 53

4.2.3. Contact angle calculation with L and V 54

4.3. Evaluation of the error introduced in the calculation of the contact angle ... 54

4.3.1. Evaluation of the error introduced in the calculation of θ by the measurement of h and L 55

4.3.2. Evaluation of the error introduced in the calculation of θ by the measurement of h and V 56

4.3.3. Evaluation of the error introduced in the calculation of θ by the measurement of L and V 58

4.4. Summary 59

5. Measurement strategies 61

5.1. Introduction 61

5.2. Contact angle meter 61

5.3. Confocal device 65

6. Experimental measures 71

6.1. Introduction 71

6.2. Samples and measurements 71

6.3. DSA-100 experimental measurements 74

6.3.1. Contact angle and surface energy measurements 74

6.3.2. Repetabilty of the measurements 77

6.4. S-Neox experimental measures 78

6.4.1. Height, width and *Sdr* measurements 78

6.4.2. Repetabilty of the measurements 81

6.5. Evolution of the volume of the drop with time 83

6.6. Validation of the calculated contact angles 87
6.7. Correction of the effect of the roughness in the calculated contact angles 90
6.8. Contact angle calculation in naturally-structured samples 91
7. Surface energy evaluation 97
7.1. Introduction 97
7.2. Evaluation of the surface energy from the measurements performed with the S-Neox. 97
7.3. Validation of the surface energy calculation 99
7.4. Summary 100
8. Summary, conclusions and future work 101
8.1. Summary 101
8.2. Conclusions 102
8.3. Future work 105
A. Preliminary results with interferometric technic 107
B. Detailed mathematical models 113
B.1. Contact angle calculation with h and L 113
B.2. Contact angle calculation with h and V 114
Bibliography 117
Published work 125

List of figures

Figure 1.1 Schematic representation of the surface tension of a liquid.....3

Figure 1.2 Schematic diagram of the contact angle formed by a sessile liquid drop on a smooth solid surface at the intersection of the liquid-solid interface and the liquid-gas interface.....4

Figure 1.3 Schematic relationship between wettability and contact angles by sessile drop on a smooth solid surface for droplets of similar volume.....4

Figure 2.1 Schematic diagram of the Wilhelmy plate measurement method.....10

Figure 2.2 Schematic drawing of the measurement process performed by the Du Noüy ring method. 11

Figure 2.3 Sessile drop with contour recognition by the DSA software.....12

Figure 2.4 Schematic drawing of the height-width method to measure the contact angle. 12

Figure 2.5 Circle fitting performed on a sessile drop image by DSA software to measure the contact angle. 13

Figure 2.6 Schematic representation of the tangent method for contact angle measurement. Source: Kyowa.....14

Figure 2.7 Images of the same 5 µL water drop placed on a superhydrophobic surface, showing the different applied fitting models of the static contact angle. (a) Ellipse fitting; (b) circle fitting; (c) Tangent fitting and (d) Young-Laplace fitting. The figures include the simulation lines of the shape of the water droplets and the horizontal baselines. Source: [34].....16

Figure 2.8 Measurement of the advancing and receding angle by the extension/contraction method consisting in increasing and decreasing respectively the volume of the liquid drop. Source: Kyowa.....17

Figure 2.9 Schematic representation of a sessile drop placed on a tilted solid surface for the measurement of the contact angle with the sliding method. 18

Figure 2.10 Determination of the critical surface energy of the solid (γC) under measurement with different measuring liquids. 23

Figure 2.11 Representation of the behaviour of a smooth and a rough surface respectively when illuminated by a light source. The smooth surface leads to a specular reflection and the rough surface to a diffuse reflection. 24

Figure 2.12 Airy pattern obtained by a (a) conventional microscope and a (b) confocal microscope. Source: [58] 25

Figure 2.13 Axial response of microscope objectives with different numerical apertures. Narrower axial responses of high values of NA means less light coming from points out of focus. Source: [58] 26

Figure 2.14 Schematic representation of a confocal microscope. 26

Figure 2.15 Representative interference pattern from a flat surface. 27

Figure 2.16 Schematic representation of (a) Michelson interferometer and (b) Mach-Zender interferometer, which are double path interferometers. 28

Figure 2.17 Representation of a Twyman-Green interferometer. 29

Figure 2.18 Representation of an exemplary common path interferometer known as Sagnac interferometer. 29

Figure 2.19 representation of an exemplary wavefront splitting interferometer known as Fresnel's biprism. 30

Figure 2.20 Representation of a vertical scanning interferometer with different recorded interferograms at different positions of the sample and the corresponding surface reconstruction. 31

Figure 2.21 Representation of a phase shifting interferometer with different recorded interferograms and the corresponding surface reconstruction. 31

Figure 2.22 Representative devices from KRÜSS to measure the contact angle and the surface energy of a solid by means a (a) portable device and (b) Laboratory device. 33

Figure 2.23 Representative devices from KYOWA. (a) Portable device and (b) laboratory device both for measuring the contact angle, surface energy of a solid and the interfacial tension. 34

Figure 2.24 Representative devices from Dyne Testing. (a) Portable device for measuring the contact angle. (b) Laboratory device for measuring the contact angle, surface energy of a solid and the interfacial tension. 34

Figure 2.25 Attension Theta Topography from Biolin Scientific and Dyne Testing. First device which allows the correction of the effect of the roughness of the surface in the contact angle measurement with a single device, but with a displacement of the sample between measurement modules. 35

Figure 2.26 Exemplary 3D non-contact profilometers from Nanovea. (a) Portable device, (b) Laboratory device to scanning samples up to 1x1 m 36

Figure 2.27 Exemplary 3D non-contact profilometers from Sensofar. (a) Different configurations allows from portable to XXL systems of this device, (b) device devoted to measuring aspheric and free-form optics. 36

Figure 2.28 Exemplary 3D non-contact profilometers from Zygo. 37

Figure 2.29 Exemplary 3D non-contact profilometers from (a) Novacam and (b) Alicona. 37

Figure 3.1 (a) Schematic diagram of Wenzel's apparent contact angle on a rough surface where the liquid droplet wets completely the surface of the solid; (b) schematic representation of the real area (A_{rough}) and the projected area (A_{flat}) of the droplet to calculate the roughness ratio factor r. 40

Figure 3.2 Representation of the measured Wenzel's apparent contact angle θ_W as a function of the Young's contact angle θ_Y for r=1.2 as an exemplary value. 41

Figure 3.3 Representation of the intrinsic contact angle as a function of the roughness factor r for different apparent angles θ_W=30°, 60°, 90°, 120° and 150° in Wenzel's scenario. 42

Figure 3.4 Evaluation of the surface energy for a hydrophilic and a hydrophobic surface for water (γ_S water) and Diiodomethane (γ_S Diiodomethane) as measurement liquids, not taking into account the roughness of the surface, compared to the intrinsic surface energy value (γ_S). 43

Figure 3.5 (a) Schematic diagram of Cassie Baxter's apparent contact angle on two component materials; (b) schematic representation of a droplet sitting on trapped air bubbles f_V between the fractions of the material f_S which represents the lotus effect and its projected area (A_{flat}) on a smooth surface. 45

Figure 3.6 Representation of the Cassie Baxter's apparent contact angle θ_{CB} as a function of the Young's contact angle θ_Y for (a) r = 1.2 and f_S = 0.4, 0.6 and 0.8 as exemplary values, (b) f_S= 0.6 and r = 1.2, 1.4 and 1.6 as exemplary values. 46

Figure 3.7 Representation of the intrinsic contact angle θ_Y corresponding to a set of given Cassie Baxter's apparent contact angles as a function of the roughness factor r for of θ_{CB} = 30°, 60°, 90°, 120° and 150° and f_S = 0.4, 0.6 and 0.8. 47

Figure 3.8 Evaluation of the surface energy for a hydrophilic surface, where the roughness varies from 1 to 2 for f_S = 0.4, 0.6 and 0.8 comparing to the intrinsic surface energy value. 48

Figure 3.9 Evaluation of the surface energy for a hydrophobic surface, where the roughness varies from 1 to 2 for f_S = 0.4, 0.6 and 0.8 comparing to the intrinsic surface energy value. 49

Figure 3.10 (a) Image of a flower petal with a water drop stuck on its surface that represents a Wenzel scenario; (b) image of sliding water on a lotus leaf that represents a Cassie-Baxter's scenario. Sources: [87], [88] 50

Figure 4.1 Schematic representation of a drop placed on a (a) high wettability surface; (b) low wettability surface assuming that it is perfectly spherical. 53

Figure 4.2 Evaluation of the error introduced in the calculation of the contact angle, in both the hydrophilic and hydrophobic regime, by the parameters h and L, measured by the confocal device, for 2, 5 and 10µL as exemplary values of V. 56

Figure 4.3 Evaluation of the error introduced in the calculation of the contact angle, in both the hydrophilic and hydrophobic regime, by the parameters h and V, for 1, 1.5 and 2mm as exemplary values of L. 57

Figure 4.4 Evaluation of the error introduced in the calculation of the contact angle, in both the hydrophilic and hydrophobic regime, by the parameters L and V, for 1, 0.5 and 0.3 mm as exemplary values of h. 58

Figure 5.1 (a) Picture of the DSA-100 from KRUSS used to perform the contact angle measurements; (b) Image of a sessile drop acquired by the DSA-100. 62

Figure 5.2 Images of the same water drop placed on a hydrophobic solid surface, showing the different applied fitting models of the contact angle by the DSA-100 software and the mean values (MCA) obtained. (a) Circle, MCA=100.0°; (b) Ellipse, MCA=103.0°; (c) Height/width, MCA=100.9°; (d) Tangent, MCA=103.2° and (e) Young-Laplace, MCA=103.2°, fitting methods. The figures include the simulation lines of the shape of the water droplets and the horizontal baselines. 63

Figure 5.3 (a) Placement of the sample in the sample holder of the DSA and location of the water drops, (b) Comparison of the sharpness of the interface when a drop is placed on the edge and far from the edge of a hydrophobic sample. 64

Figure 5.4 (a) Picture of the S-Neox from Sensofar, (b) close-up of the sample placed on the sample holder of the S-Neox and the high accuracy syringe placing the measuring water drop on the sample. 66

Figure 5.5 (a) Extended surface topography of one of the measured samples with a 20X microscope objective, (b) top-view image of the liquid drop deposited on the sample, obtained with a 5X microscope objective and (c) dual topography of both the apex of the drop and the surface of the sample performed with a 10X microscope objective. 67

Figure 5.6 (a) Measurement of L of the drop by fitting a circle to the contour of the liquid drop in the image taken by the S-Neox. (b) Calculation of the *Sdr* parameter in the area filled by the liquid drop. 68

Figure 5.7 (a) 2D view of the dual topography of both the apex of the drop and the surface of the sample to measure the height of the drop from the profile obtained from the drawn line, (b) measured height of the drop. 69

Figure 6.1 Pictures of samples S1 through S6 used in this Ph.D. Thesis to validate the developed measurement method. 72

Figure 6.2 Pictures of the same 7 µL water drop placed on sample S12 with different fittings applied by the DSA-100 to calculate the contact angle: (a) circle, (b) Ellipse, (c) Height-width, (d) Tangent and (e) Young-Laplace fittings. 76

Figure 6.3 Plot of the evolution of the volume of a drop with time of both water and Diiodomethane as measurement liquids placed on a hydrophilic and a hydrophobic sample. 83

Figure 6.4 (a) Absorbance spectrum of water and (b) absorption cross-section of Diiodomethane. Sources: [94], [95]. 85

Figure 6.5 Spectral distribution of the three LED blue (460 nm), green (530 nm) and red (630 nm) and their corresponding dichroic filters as well for the white LED with which the S-Neox is equipped. Source: [93]. 85

Figure 6.6 (a) Optical image of a Photus plant, (b) surface topography of the Photus leaf measured by the S-Neox with a 50X microscope objective to obtain the *Sdr* factor; (c) optical image of Gerbera and a drop placed on the surface of a Gerbera's petal and (d) surface topography of the Gerberas's petal measured by the S-Neox with a 50X microscope objective to obtain the *Sdr* factor. 92

Figure 6.7 (a) Optical image of a rose and a petal with a drop placed on the surface. (b) surface topography measured by the S-Neox with a 50X microscope objective to obtain the *Sdr* factor. 94

Figure 6.8 SEM image of the surface of a petal rose where the entire pillar-structure can be seen. Source: [97] 94

Figure A.1 Schematic representation of the developed system based on a Twyman-Green interferometer in which an afocal system is placed in front of the detector. 107

Figure A.2 (a) Image of the developed experimental setup placed in a platform of 450x350 mm. (b) Flat mirrors, of 25 mm of diameter, used in the measurement a liquid drop profile, both placed in a plate of 75x120 mm. 108

Figure A.3 5.7x4.28 mm acquired images of the interference pattern created by (a) the superposition of the reflected laser light on the surface of both mirrors; (b) the superposition of the reflected LED light on the surface of both mirrors. 109

Figure A.4 (a) scheme of how the light illuminates the mirror and the dispensed liquid drop, (a) schematic representation of the reflection of the light by the surface of a liquid drop 110

Figure A.5 (a) 5.7x4.28mm image of the interference pattern created by the light reflected by both mirrors with the liquid drop placed on the field of view; (b) interference pattern created by the light reflected by the upper part of the liquid drop recombined with the light reflected by the reference mirror highlighting the dimensions of the interference pattern. 111

Figure A.6 (a) Magnified image of the interference pattern of the drop; (b) intensity profile obtained along the dotted line in (a). 112

Figure B.1 Schematic representation of a drop placed on a (a) high wettability surface; (b) low wettability surface assuming that it is perfectly spherical, with the parameters involved in the mathematical expressions. 113

List of tables

Table 4.1 Values of the errors introduced by the measurement of h (δh) and L (δL) by means the confocal device and the error introduced in the volume (δV) of the drop by means of the liquid dispenser. 55

Table 6.1 Summary of the hydrophobic measured samples indicating the supplier, the substrate material and the measurements performed with both the DSA-100 and the S-Neox. 73

Table 6.2 Summary of the hydrophilic measured samples indicating the supplier, the substrate material and the measurements performed with both the DSA-100 and the S-Neox. 73

Table 6.3 Superhydrophobic sample, indicating the supplier, the substrate material and the measurements performed with both the DSA-100 and the S-Neox. 74

Table 6.4 Summary of the mean contact angle value and its standard deviation obtained by the DSA-100 in hydrophobic samples. The software also calculates the surface energy and gives the total surface energy as well as its dispersive and polar components..... 75

Table 6.5 Summary of the mean contact angle value and its standard deviation obtained by the DSA-100 in hydrophilic samples. The surface energy is also calculated by the software and gives the total surface energy as well as its dispersive and polar components. 75

Table 6.6 Summary of the mean contact angle value for water as a measurement liquid and its standard deviation measured by the DSA-100 for the superhydrophobic sample (S12) obtained different fittings. 77

Table 6.7 Comparison of the mean contact angle values obtained by the 3-drops method and the ones obtained by the 12-drops method for samples S2 and S5. 78

Table 6.8 Summary of the mean values of h and L measured for three different 2µL drops of both water and Diiodomethane measured by the S-Neox on hydrophobic samples as well as the mean value of the *Sdr* of each sample. 79

Table 6.9 Summary of the mean values of h and L measured with the S-Neox for three different 2µL drops of both water and Diiodomethane on hydrophilic samples, together with the mean value of the *Sdr* of each sample. 79

Table 6.10 Summary of the mean values of h and L measured f by the S-Neox for three different 7µL water drops on superhydrophobic samples, together with the mean value of the Sdr. 80

Table 6.11 Calculated contact angle values and their standard deviation, for both water and Diiodomethane and the *r* factor for the set of hydrophobic samples. 80

Table 6.12 Calculated contact angle values and their standard deviation, for both water and Diiodomethane and the *r* factor for the set of hydrophilic samples. 80

Table 6.13 Calculated contact angle value and its standard deviation, for both water and Diiodomethane and the *r* factor for the superhydrophobic sample. 80

Table 6.14 Comparison of the mean h and L values obtained by the 3-drops method and the ones obtained by the 12-drops method for samples S2 and S5. 82

Table 6.15 Summary of the volume losses according to the wetting properties of the sample under study and the device with which the measurements are performed. 84

Table 6.16 Value of the different parameters involved in the calculation of the temperature increase of a drop of water illuminated by the green LED of the S-Neox during the time taken to perform the measurement. 86

Table 6.17 Comparison between the contact angles measured with the DSA-100 and the ones calculated by the developed measurement method using the S-Neox in hydrophobic samples. 87

Table 6.18 Comparison between the measured contact angles by the DSA-100 and the ones calculated by the developed measurement method using the S-Neox in hydrophilic samples. 88

Table 6.19 Comparison between the contact angle measured with the DSA-100 and the one calculated by the developed measurement method using the S-Neox in the superhydrophobic sample for water. 89

Table 6.20 Values of the contact angles corrected (θY) of the effect of the roughness of the surface according to Wenzel's model in hydrophobic samples for both water and Diiodomethane. 90

Table 6.21 Mean values of h and L measured with 4µL liquid drops and the value of the Sdr obtained by the S-Neox of the selected real samples. 93

Table 6.22 Correction of the contact angle value with the r factor according to Wenzel's model. 93

Table 6.23 Correction of the contact angle value with the r factor according to Wenzel's model. 94

Table 7.1 Surface energy values for water and Diiodomethane. 98

Table 7.2 Values of the total surface energy (Total SE) and its dispersive and polar components calculated from the corrected contact angles measured in the hydrophobic samples by means of the developed measurement method. 98

Table 7.3 Comparison between surface energy values corrected by the effect of roughness obtained by the developed measurement method and the ones calculated by the DSA-100. 99

1. Introduction

Within the past ten years, the coating community has witnessed a great increase in interest in nanostructured materials for a number of industrial applications, such as marine, aviation and wind blades. For example, the erosion sustained by surfaces of aircraft during routine flight increases fuel consumption by 5%, as do the corresponding CO_2 emissions. Also, wind turbines placed in the Nordic environment, suffer the generation of ice causing losses about 5-10% of electricity production and in sub-tropical warmer environment, fouling of the blade by insects can reduce the power production as much as 50% [1]. By the study and characterization of such nanostructured coatings, a better comprehension of their behaviour and an improvement of their performance can be achieved in order to solve, or at least improve, the problem of the loss of energetic efficiency in such situations.

As the European Union defines, a nanostructured material has at least one constituent at a characteristic length scale in the order of tens of nanometers or less [14]. Nanostructured coatings have properties different from homogenous materials due to the intentional inbuilt nanoscale features in their structure, which present some difficulties for characterization.

In this context arose the European project NATURAL "Standardized metrology of Nano-sTrUctuRed coAtings with Low surface energy" (FP7-NMP-2012-SME-6, 310397) which had clear objectives related with the topic concerned. The NATURAL project was focused on developing real-world, practical characterization methods for nano-structured coatings with a low surface energy for anti-fouling applications and/or for low friction applications. In both aspects, the measurement of the surface energy of the coating by the measurement of the contact angle is essential.

The standards body (ISO TC229) recognizes that there are no current procedures that relate the functional performance of a surface or coating to its nanostructure. However, it is recognized that the loss of the nanostructure frequently leads to a loss of performance. Therefore, project Natural aimed at relating surface nano-morphology to the functional performance and to enable the development of new methods for lifetime determination and, ultimately, prediction.

Within these actions, SnellOptics™ company, as an industrial partner of the project NATURAL, took the decision to improve its scientific knowledge in this field in order to take advantage of the new possible opportunities that could arise from this topic. As the means to acquire and incorporate this knowledge, SnellOptics™ applied for an industrial Ph.D. scholarship (project 2014 DI 047) which gave the opportunity of doing this industrial Ph.D. on this subject.

Specifically, this industrial Ph.D. Thesis "Device and strategy for surface energy measurement" is focused on the development and validation of a new measurement method able to simultaneously evaluate the surface energy and the structure of a surface by using a single device, which would provide a solution to the above exposed problem. The applicability of this new measurement method is mainly found in the field of development of new materials with specific functionalities for which both the microstructure and the chemical component should be differentiate when evaluating the wetting properties.

By using a device devoted to perform topographic measurements, we will measure some parameters that will allow us to calculate the contact angle of a solid surface by means of the mathematical expressions included in the developed measurement method. Furthermore, the device will allow the measurement of a parameter that evaluates the roughness of the surface under study. Thus, it will enable the correction of the effect of the roughness of the surface on the calculation of the contact angle according to Wenzel's or Cassie-Baxter models.

Moreover, until very recently no commercial device was available to perform both topography and contact angle measurements. The use of two different devices leads to a sample positioning uncertainty, implying that besides the time and resource consumption inherent to making two different measurements with two different devices, no assurance can be given that both measurements are performed on the same area on the sample and that the resulting calculated surface energy is correct. Therefore, we will evaluate the surface energy of a surface under study with less error than the achieved by current techniques.

The use of the confocal technique, which is completely different to those commonly used to evaluate the surface energy of solids, highlights the novelty of this Ph.D. Thesis and the inventiveness of the presented measurement method, which is also enshrined in the patent EP16001763. Needless to say, the possibility of performing contact angle measurements with an optical profilometer (in this case a confocal device) is, in itself, a significant accomplishment as it would eliminate the need for acquiring a specific instrument for the contact angle measurement for those laboratories already equipped with a confocal microscope.

This innovation opens the way, in a near future, to implement a system capable of relating the measurement of the contact angle and the measurement of the topography of the surface, and, thereafter to refine the accuracy of the determination of the surface energy of solid surfaces. This would be especially important for non-smooth samples, for which the impact of the topography on the contact angle is relevant.

1.1. Introduction to surface energy

Surface energy plays a major role in friction, lubrication and wear phenomena in contact materials and especially, in flow-surface interactions with liquids. Tribology [2], [3] is the science entrusted to evaluating these interactions between surfaces in relative motion. When a solid surface is faced with interfacing materials and environment, a resulting loss

of material from the solid surface could take place. This is known as wear and includes abrasion, friction, erosion and corrosion processes. In order to minimize the loss of material in these interaction situations, a modification of the surface properties is performed by applying a coating directly on the surface.

Surface energy is defined as the energy associated with the intermolecular forces at the interface between two media and it is also called surface free energy [4]. For solids and liquids the surface represents a higher energy state in comparison with the bulk.

For a solid, surface energy is defined as the excess of energy present at the surface of a material compared to the bulk. On the other hand, when a liquid phase is concerned, usually it is called surface tension. Since there is a persistent confusion between both definitions, surface tension can be defined easily as the force that the molecules of the liquid perform in order to minimize the surface area of the liquid and its magnitude is known as wettability [5] as Figure 1.1 shows.

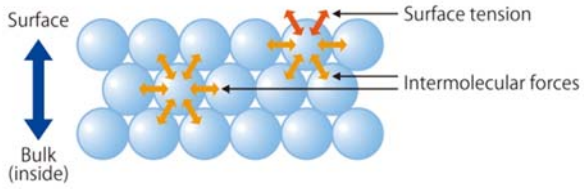

Figure 1.1 Schematic representation of the surface tension of a liquid.

The surface tension of a liquid results from an imbalance of intermolecular attractive forces, known as the cohesive forces between molecules. On the one hand, a molecule in the bulk of the liquid experiences cohesive forces with other molecules in all directions. Conversely, a molecule at the surface of a liquid experiences only net inward cohesive forces [6].

The ability of liquids to minimize their surface area leads to the formation of spheres while solids do not have this capability. The study of the wetting behaviour of solids by liquids acquires significant relevance since it establishes the foundations for surface energy measurement and its determination [7].

This interaction between the liquid and the solid surface in terms of the ability of the liquid to wet is described by the Young equation (1.1) [8] which assumes the surface to be homogeneous in the chemical composition and topographically smooth.

$$\gamma_S = \gamma_L \cdot \cos\theta_Y + \gamma_{SL} \tag{1.1}$$

where γ_S is the surface energy of the solid, γ_L is the surface tension of the liquid and γ_{SL} is the surface energy at the solid-liquid interface. Then, θ_Y is the Young contact angle defined as the angle formed by the intersection of the liquid-solid interface and the liquid-gas interface, also called the three-phase boundary, shown in Figure 1.2.

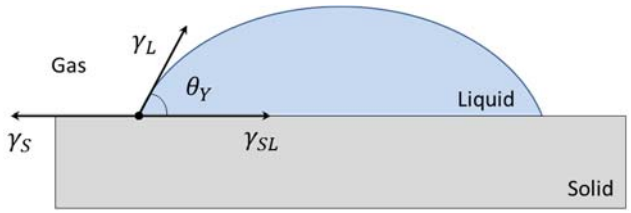

Figure 1.2 Schematic diagram of the contact angle formed by a sessile liquid drop on a smooth solid surface at the intersection of the liquid-solid interface and the liquid-gas interface.

All solids have specific surface energy values and the value of the contact angle will be different for different liquids. For a given liquid, as the surface energy of the solid decreases the contact angle increases, and therefore, the wettability is reduced as Figure **1.3** shows.

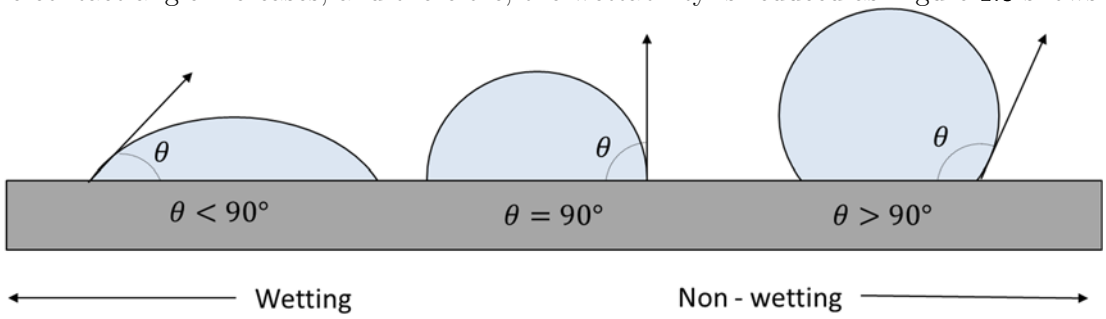

Figure 1.3 Schematic relationship between wettability and contact angles by sessile drop on a smooth solid surface for droplets of similar volume.

The existing direct relationship between the contact angle and the surface energy implies that the surface energy can be evaluated from measuring the contact angle, since its direct measurement cannot be performed [4], [9].

There are a wide variety of techniques to achieve the surface energy calculation [10] that will be introduced in next chapters. Some of them are based in the calculation of the surface tension of the liquid and then, the calculation of the value of the contact angle, such as Wilhelmy Plate [11] or the Captive Bubble method [12]. On the other hand there are others more recently developed as the drop-shape analysis methods [13] for direct calculation of the contact angle.

It is important to highlight that the measurement of the contact angle is often performed with at least two different liquids with specific properties. The explanation lays on the assumption that the surface energy of a solid is a sum of independent components associated with specific interactions which can be grouped into polar and dispersive components[14], [15]. The dispersive and polar parts of the surface tension of the liquids must be previously known to determine the surface energy of the solid. Depending on this fact, there are different models for calculating the surface energy depending on the interaction components of the surface energy [15]–[17].

1.2. Goals

The main objective of this Ph.D. Thesis is the development of a new measurement method able to evaluate the contact angle and the surface energy of rough, solid, hydrophobic surfaces with a single device based on optical profilometry.

The technology on which this device is based is known as confocal and it is devoted to perform topographic measurements. As this technique is completely different from the ones commonly used to perform these measurements, this Ph.D. thesis is also focused on demonstrating its validity and accuracy in the measurement of the necessary parameters for the calculation of the contact angle.

The advantage of using confocal microscopy for this application lies in its capability to measure the topography of a surface under study. With the measurement of this parameter, this Ph.D. thesis will prove that the evaluation of both the contact angle and further the surface energy performed by means of the presented measurement method is more accurate than the one presented in currently available commercials contact angle meters since we will correct the effect of the microstructure of the surface in their evaluation.

In order to reach the goals of this Ph.D. Thesis, the following steps have been completed:

1. Review of the currently available techniques and methods to perform contact angle measurements and surface energy evaluations. Furthermore, we also review the most common techniques used to perform topographic measurements.
2. Review of the effect of the roughness of a surface in the contact angle measurements and the further evaluation of the surface energy according with Wenzel's and Cassie Baxter's model.
3. Presentation of the mathematical models of the developed measurement method and evaluation of the minimum error made when applying these mathematics to the contact angle calculation assuming the drops are perfectly spherical.
4. Introduction to the measurement strategies to measure, on the one hand, the contact angle and the surface energy with a commercial contact angle meter and on the other hand, the height and the width of the liquid drop and the roughness factor of the surface under study by means of the confocal device.
5. Validation of the presented technique by analysing and comparing the contact angle values obtained by means of the commercial contact angle meter and those calculated with the mathematical model of the presented method using the parameters of the liquid drop measured by the confocal device. Furthermore, the correction of the effect of the roughness on the contact angle is also performed, on those samples were the validation is successfully performed.
6. Evaluation of the surface energy taking into account the roughness of the surface from the contact angle values calculated and corrected by means of the developed measurement method presented in this Ph.D. Thesis.

1.3. Ph.D. Thesis structure

This Ph.D. Thesis has been organized in 8 chapters, including this one, as follows:

Chapter 2 gives an overview of the main available methods for measuring the contact angle and the methods for the further evaluation of the surface energy. It also presents a glimpse of different techniques to perform topographic measurements by means of 3D non-contact optical profilometry. Lastly, this chapter includes a brief overview of the commercial setups available nowadays in the market to perform the previous measurements individually, and introduces a recently developed device to measure the surface energy and the structure of the surface but with a different methodology and technique.

Chapter 3 introduces the influence of the roughness of a surface in the measurement of the contact angle and the further evaluation of the surface energy. Different models to evaluate correctly the contact angle and the surface energy taking into account the roughness of a surface are presented as well as how we face this effect in this proposed measuring method.

Chapter 4 describes the proposed mathematical methods for calculating the contact angle based on the measurement of different parameters of a liquid drop placed on a horizontal solid surface. Three different mathematical methods are presented relating to different wetting measurement conditions and an evaluation of the introduced error in the calculation of the contact angle by the measurements of these parameters is also performed.

Chapter 5 presents the two different devices that were used in this study as well the measurement strategies used with each one. On the one hand, and in order to obtain reference values, a commercial contact angle meter, used to measure the contact angle on the solid samples with images taken in a side view configuration. On the other hand, the confocal device used to measure the set of parameters of the drop to calculate the contact angle with the proposed measurement presented in this thesis.

Chapter 6 provides the results of the experimental measurements performed with both the commercial contact angle meter and the confocal device. These measurements include the contact angle and surface energy calculated by the software of the contact angle meter as well as the measured parameters of the drop and the real area of the surface measured by the confocal device. The corresponding calculated contact angles applying the developed mathematical method will also be presented, as well as the roughness ratio factor calculated from the real area measured by the confocal device. A comparison between the contact angle values obtained with the commercial contact angle meter and the ones obtained by the confocal device will be made, proving the validity of the developed measurement method. Finally, the correction of the calculated contact angles will be performed according to Wenzel's model, only for those samples for which the validation of the calculated contact angles was successfully performed.

Chapter 7 provides the evaluation of the surface energy according to the OWRK method from the corrected angles of those samples where the validation of the calculated contact angles was successfully performed. A comparison will be made between these values of the

surface energies, taking into account the roughness of the surface, and the values obtained by the commercial contact angle meter, assuming a smooth surface. With this comparison, we will be able to confirm the validity of the developed measurement method in this Ph.D. Thesis to evaluate the surface energy of a solid surface taking into account the roughness of the surface.

Chapter 8 summarizes the work developed in this Ph.D. Thesis, outlines the conclusions obtained during the work performed in this Ph.D. thesis and discuss future perspectives of work.

Finally, two appendixes complete this Ph.D. Thesis with the previous studies performed with interferometry as the measurement technique and the detailed mathematical developed models.

2. State of the knowledge in the field

2.1. Introduction

This section outlines the context in which this PhD thesis is located. Firstly, in the state of the art, we will review the main methods used to measure the contact angle. Furthermore, a review of different methods to determinate the surface energy by means of the previous measurement of the contact angle will be made as well as a review of different techniques used to perform 3D non-contact topographic measurements, such as confocal technique and interferometry.

Secondly, we will present a brief overview of several available commercial devices nowadays in the market to perform contact angle measurements and the corresponding surface energy evaluation, proving the existing interest of the scientific community in the concerned topic of this Ph.D. thesis.

To finish, a brief overview of several suppliers of devices to perform contact angle meter and surface energy measurements will be introduced, as well as suppliers and devices of 3D non-contact profilometers currently available in the market.

2.2. State of the art

This section is divided in three different subsections. The first one covers the main methods used nowadays to perform contact angle measurements. The second section covers different methods developed to evaluate the surface energy by the previous measurement of the contact angle. Finally, the last subsection will cover the confocal and interferometry techniques as the main techniques used to perform topographic measurements by 3D non-contact profilometers.

2.1.1 Contact angle calculation methods

The topic of wetting plays an important role in many industrial processes, such as oil recovery, lubrication, liquid coating, printing, and spray quenching. In recent years, there has been an increasing interest in the study of superhydrophobic surfaces, due to their potential applications in, for example, self-cleaning, nanofluidics and electrowetting [18]. The measurement of the contact angle as a primary data in these applications, and also in this PhD thesis, is a key point in the determination of important parameters, such as the surface energy of a solid. This section will be based on the review made by Chau [19] in which different techniques for measuring the contact angle and their applications are compiled.

Measurements of contact angle have been reported since about the year 1800 with great variability found in these data. There are two different types of contact angles to be measured known as the static and the dynamic contact angles. On the one hand, static contact angles are measured when a droplet is standing on a horizontal surface and the three-phase boundary is not moving. On the other hand, when the three-phase boundary is moving, dynamic contact angles can be measured and are referred to as advancing and receding angles. It is important to highlight that the contact angle always depends on the properties of the liquid used to perform the measurements.

A wide range of techniques are available to measure the contact angle [19] and they are broadly classified into indirect force methods and direct optical methods. Indirect force methods include the Wilhelmy and the Du Noüy ring method. On the other hand, direct optical methods enclose methods such as circle, tangent and polynomial fitting as well as the height-width and the Young Laplace method, which will be detailed hereunder.

Starting by indirect force methods, the Wilhelmy method [20], [21] is originally devised for surface tension determination but it has been found suitable for measuring contact angle between a liquid and a solid and also the interfacial tension between two liquids. The method involves the determination of the force acting on a vertically immersed plate in a liquid as shown in Figure 2.1.

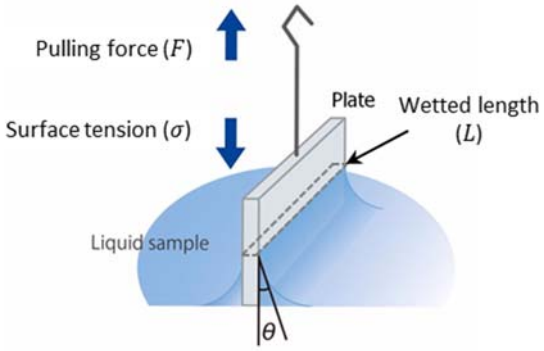

Figure 2.1 Schematic diagram of the Wilhelmy plate measurement method.

The plate touches the liquid surface or an interface while it is vertically suspended from a force sensor or tensiometer. The pulling force F that acts on the plate is measured by the tensiometer. By transposing the Whilhemy equation (2.1), the value of the contact angle θ can be obtained as long as the value of the surface tension σ is known.

$$\sigma = \frac{F}{L \cdot \cos\theta} \tag{2.1}$$

where the wetted length L of the plate is equal to its perimeter and must be constant along all the plate to not depend on the immersion depth.

Another similar method is the Du Noüy ring method [22]–[25]. As the name suggests, a ring made of platinum is used instead of the plate. The ring that is hanging parallel to the

liquid surface is sunk into it. Then, the ring is gradually drawn apart from the surface in a vertical direction as Figure 2.2 shows.

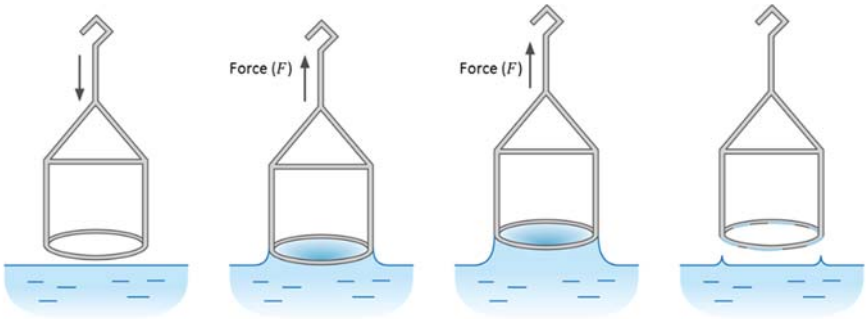

Figure 2.2 Schematic drawing of the measurement process performed by the Du Noüy ring method.

In this process, the surface tension of the liquid membrane that is hanging by the ring generates a force on the ring that changes as the ring is drawn farther. The maximum value of the force is used to determine the surface tension by means of equation (2.1), where, in this case, the wetted length L of the ring is the sum of the inner and outer circumference. It is important to highlight that this method needs a measurement correction [25], [26] since the weight of the liquid of the plate increases the measured force and also because the force maximum does not occur at the inside and outside of the lamella at the same time.

These two presented methods are the main ones covered by the indirect force method for measuring contact angles. These methods have evolved in such a way that the measurement of the force is performed with the help of an electronic force sensor and not by manual devices.

Different ways for measuring the contact angle are covered by direct optical methods. These methods are based on the use of a liquid drop that is placed on the solid surface to be measured. Commonly, the analysis of the drop is performed by drop shape analysis.

Drop shape analysis (DSA) [27], [13] is an image analysis method for determining the contact angle from a side-view image of a sessile drop. The method consists on acquiring an image of a drop placed on a solid surface from side-view commonly by means of a camera. The drop in contact with the solid surface assumes a spherical shape. The DSA software recognizes its contour by a grey-scale analysis of the image as shown in Figure 2.3.

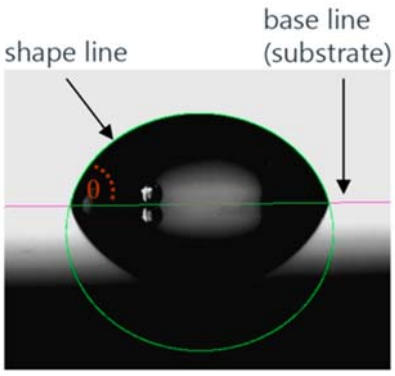

Figure 2.3 Sessile drop with contour recognition by the DSA software.

Once the drop shape function is calculated, the contact angle can be obtained from the angle defined between the contour and the solid surface base line.

Several methods are available for determining the contact angle in different ranges with different assumed drop shapes that will be discussed below. It is important to highlight that for all such methods the drop used should be small enough to allow to ignore the gravity effects [28].

One of the methods used by the DSA software to fit the contour of the drop to a given shape is the height-width method [29], also named as half-angle method. This method consists in assimilating the shape of the drop to a part of the outline of an imaginary circle as shown in Figure 2.4 Schematic drawing of the height-width method to measure the contact angle.

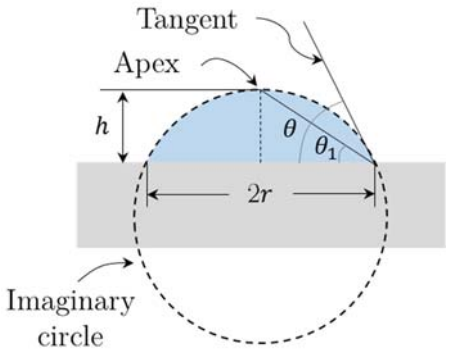

Figure 2.4 Schematic drawing of the height-width method to measure the contact angle.

The contact angle can be then calculated from the measurement of both the height h and width $2r$ of the circular arc. The height is obtained from the intersection of the straight lines connecting the left and right three-phase points and the apex of the drop against a solid surface. Concretely, this method is based on the measurement of three points: the two three-phase points and the apex of the drop.

From the geometric theorem, we known that in a circle, the relation $\theta = 2\theta_1$ is fulfilled, and then the contact angle is determined by equation (2.2).

$$tan\,\theta_1 = \frac{h}{r} \quad \rightarrow \quad \theta = 2 \cdot atan\frac{h}{r} \tag{2.2}$$

An alternative method to calculate the contact angle with the DSA software is the circle fitting in which the whole contour of the drop is evaluated. In this case, the shape of the sessile drop is also assumed to describe a circular arc on the surface as shown in Figure 2.5.

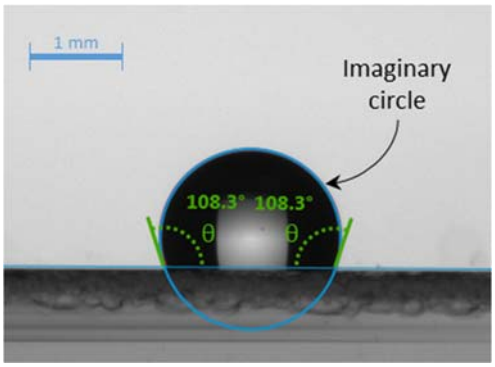

Figure 2.5 Circle fitting performed on a sessile drop image by DSA software to measure the contact angle.

The parameters of a circular arc equation are matched by software to the optically determined drop shape. In this case, the contact angle is defined by the intersection between the circular arc and the baseline defined by the solid surface. The main difference from the height-width method is that here, the whole contour of the image of the drop is evaluated instead of only three significant points. For this reason, this method is considered more reliable given that it is less susceptible to measurement errors. On the other hand, the more spherical is the drop, the more accurate the circle method.

Another similar method is the ellipse fitting in which the shape of the sessile drop is assumed to be a part of an imaginary ellipse and the parameters of an ellipse equation are matched to the optically determined drop shape.

A different method from the previous ones is the tangent fitting method [30]. In this method, the contour shape of the droplet is also assumed to be part of an imaginary circle. The tangent lines near the three-phase points are determined using the drop shape and the contact angle is defined as the intersection point between this tangent line at the three-phase point and the baseline defined by the solid surface as Figure 2.6 shows.

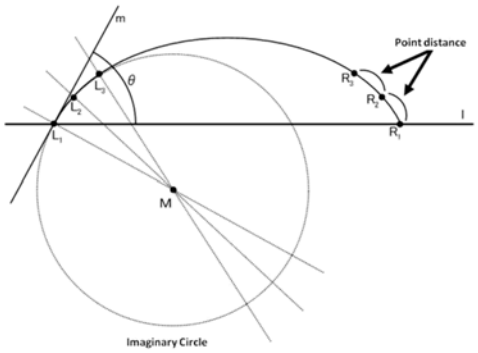

Figure 2.6 Schematic representation of the tangent method for contact angle measurement. Source: Kyowa.

The resulting contact angle is determined as the average of the contact angle measured at both sides of the drop. The left contact angle is determined as the angle between the tangent line m, obtained from the three arc points L_1, L_2 and L_3 forming the imaginary circle, and the drop baseline l. Likewise, the right contact angle can be obtained using points R_1, R_2 and R_3.

An exclusively fitting-based method to obtain the contact angle by the DSA is the polynomial fitting [31], in which a number of points from the contour of the drop, located near the three-phase point, are extracted and fitted by a polynomial for which the degree and the number of coordinate points should be adjusted. The contact angle is then obtained with the derivative of the polynomial.

On the other hand, Young-Laplace fitting [19], [32] changes slightly the way of measuring the contact angle from the analysis of a sessile drop. This method analyzes the drop shape based on the shape of an ideal sessile drop for which the curvature of its surface results only from the equilibrium of forces between the surface tension of the liquid and its weight. In this case, the gravity is the dominating force and the liquid fulfils the Young-Laplace equation (2.3).

$$\Delta p = \gamma_L \cdot \left(\frac{1}{R_1} + \frac{1}{R_2}\right) \tag{2.3}$$

This equation explains the relationship between the radii of curvature of the surface, R_1 and R_2 at each point, the surface tension of the liquid γ_L and the Laplace pressure Δp, i.e. the pressure difference across the interface, for a curved liquid surface. This means that the hydrostatic pressure resulting from the weight of the liquid affects the curvature of a sessile drop, which is under the effect of gravity. On the other hand, the radii of curvature of the surface changes as a function of the height of the drop. The Young-Laplace equation is solved by means of numerical analysis which determines the parameters of an equation system which models the shape of the sessile drop [33].

In a situation where the liquid drop is considered to be axisymmetric and the solid surface where it is placed is considered to be horizontal and homogeneous, the drop profile follows the well-known second-order differential equation (2.4) of Young-Laplace.

$$\left(\frac{1}{R_1}+\frac{1}{R_2}\right)=ch+\frac{2}{b} \tag{2.4}$$

Where R_1 and R_2 are the principal radii of curvature at any point on the drop, b is the radius of curvature at the apex and c corresponds to the capillary constant defined in equation (2.5).

$$c=\Delta\rho\cdot\frac{g}{\gamma_L} \tag{2.5}$$

The capillary constant relates the surface tension of the measurement liquid γ_L, the difference in density of the phases involved $\Delta\rho$ and the gravitational constant g.

In such a case, the Young-Laplace fit gives the best approximation between the theoretical and the real drop shape. Furthermore, it is suitable for calculating the surface tension of the liquid by knowing the drop image magnification and the density of the liquid used.

On the other hand, it can be applied also to drops whose shapes deviate from the elliptical form for large contact angles and volumes but it is not suitable for asymmetrical drops, for example, for the measurement of dynamic contact angles or for measurements on tilted surfaces.

To give a review of the most important methods used nowadays, it is of special interest to examine the work performed by X. Zhang et al. [34] in superhydrophobic surfaces.

Different fittings were performed for a sessile drop of water placed on a superhydrophobic surface, as shown in Figure 2.7, which is characterized by leading to contact angle values between much higher than 90°.

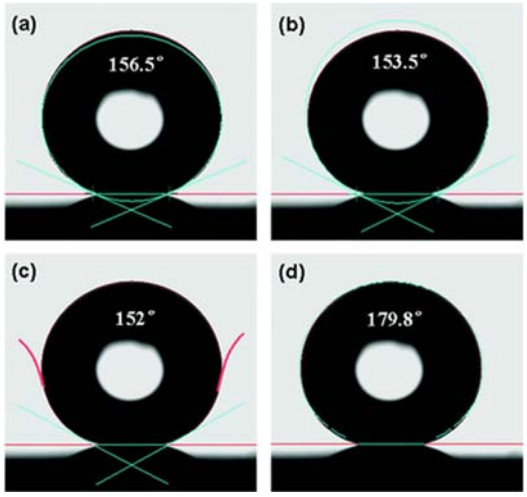

Figure 2.7 Images of the same 5 µL water drop placed on a superhydrophobic surface, showing the different applied fitting models of the static contact angle. (a) Ellipse fitting; (b) circle fitting; (c) Tangent fitting and (d) Young-Laplace fitting. The figures include the simulation lines of the shape of the water droplets and the horizontal baselines. Source: [34].

Comparing the fitted lines and the surface of the drop, it is easy to see that the best fitting is the one performed by the Young-Laplace fitting [Figure 2.7(d)]. This is due to the fact that the Young-Laplace fitting does not use only three points of the surface to calculate the contact angle between the drop and the surface but adjusts the parameters of an equation system which models the shape of the sessile drop making use of numerical analysis. Furthermore, the first three fittings give a contact angle around 156° while the Young-Laplace fitting the contact angle is larger than 179°. The difference is due to the deformation of the water drop by the effect of the gravity which is taken into account in the Young-Laplace method; hence it is more accurate than the other methods for modelling drops on superhydrophobic samples.

The methods presented so far are based on the analysis of the shape of static liquids drops. There are many applications that require time-dependent studies to evaluate different parameters of the surface such as roughness and heterogeneity [35]. Ideally, according to Young's equation, a single contact angle value is expected for a given system, although a range of contact angles is usually obtained instead. In these situations, the dynamic contact angles are a key point of the measurement.

The dynamic contact angle is the contact angle which occurs in the course of wetting or de-wetting a solid surface and is referred as advancing and receding angles, respectively. The advancing angle is measured at a surface repeatedly re-wetted and at several positions to minimize time effects such as evaporation. On the other hand, the receding angle is measured when de-wetting occurs and it is usually smaller than the advancing angle. These angles give the maximum and minimum values that the static contact angle can have on the surface and the difference is known as hysteresis.

Contact angle hysteresis arises from the chemical and topographical heterogeneity of the surface, solution impurities absorbed by the surface, or swelling, rearrangement or alteration of the surface by a solvent [36], [37] .

A criterion to be followed in choosing dynamic or static contact angle types of measurement is the technical wetting process intended for the surface. Dynamic processes, such as coating, are better modelled by dynamic measurements. On the other hand, static angles are more appropriate for evaluating quasi-static processes such as bonding in semiconductor technology.

Dynamic contact angles can be measured by different methods such as modifying the volume of a droplet or tilting the solid surface under study.

The measurement of the dynamic contact angle by changing the volume of a droplet is also called the extension/contraction method [38]. This method consists in inflating and deflating a sessile drop which is in contact with a solid surface by increasing and reducing its volume by means of a liquid dispenser as Figure 2.8 shows.

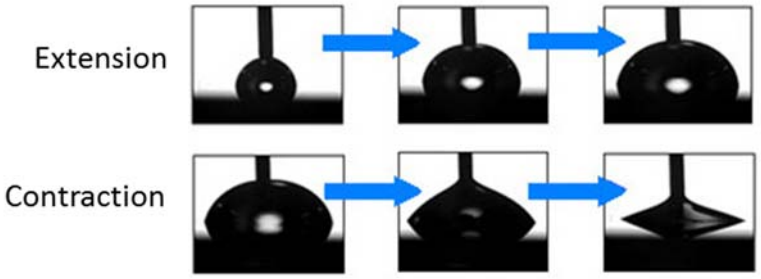

Figure 2.8 Measurement of the advancing and receding angle by the extension/contraction method consisting in increasing and decreasing respectively the volume of the liquid drop. Source: Kyowa

The advancing contact angle is measured while the volume is increased gradually, whereas the receding angle is measured while the volume of the drop is gradually decreased.

Another method to measure the dynamic contact angle is the sliding method which is based on tilting gradually the surface of the solid where the sessile drop is placed [39]. The advancing contact angle (θ_a) is measured at the front of the drop just before it starts to move, while the receding contact angle (θ_r) is measured simultaneously at the back of the drop as shown in Figure 2.9.

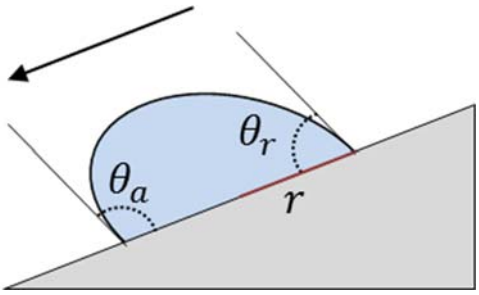

Figure 2.9 Schematic representation of a sessile drop placed on a tilted solid surface for the measurement of the contact angle with the sliding method.

This method is also used to obtain information about adhesion and slipperiness in solid-liquid interactions that cannot be obtained by the data from planar measurements.

Both methods are also performed by DSA and are included in the direct optical methods.

One of the methods belonging to the indirect force methods is also capable of measuring dynamic contact angles. This method is the Wilhemly and the measurement consists on slowly immersing and then withdrawing the solid. The advancing angle is determined during the wetting process and the receding angle during the de-wetting process [40].

After completion of the overview of the main methods available nowadays to perform contact angle measurements, it is important to take into account that, as we will discuss extensively in next chapter, properties of the surface such as the chemical composition or the surface microstructure have a relevant impact on the contact angle. We will consider them in the treatment of the contact angle data.

Next subsection will introduce different methods to evaluate the surface energy of a surface under study by the previous measurement of the contact angle performed by any of the methods already presented.

2.2.1. Surface energy determination methods

The determination of the surface energy of a solid surface is not a simple task. The surface energy of a solid cannot be directly measured and its value is calculated from a set of liquid/solid contact angles for a variety of liquids for which the value of the surface tension is known. There are several widely used theories for converting contact angle data into solid surface energy values which we will introduce next, based on the review made by M. Żenkienwicz [41].

The calculation of the surface energy of a solid surface can lead to different results, depending on the test liquids used for the measurement of the contact angle and on the surface energy theory chosen for analyzing the data. Below are described the most common methods for the calculation of the surface energy of a solid by means of the previous measured contact angles.

When a liquid drop is placed on a solid surface, the balance at the three phase contact point of solid, liquid and gas, is described by Young's equation (2.6) [8] assuming that the surface is chemically homogenous and topographically smooth.

$$\gamma_S = \gamma_L \cdot \cos\theta_Y + \gamma_{SL} \tag{2.6}$$

This equation describes the relation among the solid surface energy (γ_S), the contact angle (θ_Y), the surface tension of the liquid (γ_L) and the interfacial tension between the solid and the liquid (γ_{SL}). On the one hand, θ_Y, also known as Young's contact angle, corresponds to the intrinsic contact angle obtained by any of the previously presented methods assuming that the surface is chemically homogenous and topographically smooth. On the other hand, γ_L can also easily be obtained since it is a property of the liquids themselves. Conversely, γ_{SL} is a parameter that cannot be measured directly so more assumptions of the relationship between the different components must be sought and the term work of adhesion [42] has to be introduced.

Let us suppose a system in which two different phases are in contact. The work of adhesion W_{12} is the work required to separate these two adjacent phases 1 and 2 from one another, which can be in liquid-liquid or liquid-solid phase boundary. When one phase is wetted by another, the two previous surfaces disappear releasing energy due to the respective surface tensions γ_1 and γ_2. At the same time, work must be done in order to form the interface, referred to as interfacial tension γ_{12}. The work of adhesion is then described with equation (2.7).

$$W_{12} = \gamma_1 + \gamma_2 - \gamma_{12} \tag{2.7}$$

For a solid-liquid phase boundary, as in the case of interest, the work of adhesion W_{SL} can be written as (2.8)

$$W_{SL} = \gamma_L + \gamma_S - \gamma_{SL} \tag{2.8}$$

which in combination with (2.6) leads to the Young-Dupré equation (2.9), the basis of surface energy theories [43].

$$W_{SL} = \gamma_L(1 + \cos\theta_Y) \tag{2.9}$$

The basic assumption made above is reflected in the so-called equation of state (2.10).

$$F(\gamma_S, \gamma_L, \gamma_{SL}) = 0 \tag{2.10}$$

This equation represents the dependence of γ_{SL} on the properties of the solid and the measuring liquid, which can be rewritten as equation (2.16) shows.

$$\gamma_{SL} = F(\gamma_S, \gamma_L) \tag{2.11}$$

According to Dupré, the work of cohesion (W_C) is defined as the work done in dividing two phases and only depends on their surface energies or tensions (γ), so γ_{SL}=0. Then, equation (2.8) can be simplified as equation (1.1) shows.

$$W_C = 2\gamma \tag{2.12}$$

Berthelot [44] then introduced the following hypothesis shown in equation (2.13).

$$W_{SL} = \sqrt{W_{C_S} \cdot W_{C_L}} \tag{2.13}$$

The previous equation can be rewritten as shown in equation (2.14)

$$W_{SL} = \sqrt{2\gamma_S \cdot 2\,\gamma_L} \tag{2.14}$$

Combining equations (2.9) and (2.14) the relation shown in equation (2.15) which implies that the surface energy of a solid can be obtained directly from the previously measured contact angle as long as the surface tension of the liquids is known.

$$\gamma_L(1 + cos\,\theta_y) = 2\sqrt{\gamma_S \cdot \gamma_L} \tag{2.15}$$

In addition to Berthelot, numerous studies were carried out by many authors based on the equation of states, such as Antonow [35], [45] and Girifalco and Good [46]. However, the best known are the approaches derived by Neumann et al. from the studies carried out by the other authors [47].

The first approach is obtained from the fundamental thermodynamic relations taking into account intermolecular interactions [48]. The second approach is a modification of the Berthelot hypothesis and the third one is a further modification of the same hypothesis [47]. The results of these studies led to a controversy in the scientific community about the possibility of the division of the surface energy into individual components including the assumption that γ_{SL} is determined by various interfacial interactions that depend on the properties of both the measurement liquid and the solid.

At this point, different theories for surface energy calculation arose based on the partition of this quantity into components.

Fowkes [16] developed one of the first theories. He was a pioneer in assuming that the surface energy of a solid is a sum of independent components, related with specific interactions represented by equation (2.16).

$$\gamma_S = \gamma_S^d + \gamma_S^p + \gamma_S^h + \gamma_S^i + \gamma_S^{ab} + \gamma_S^o \tag{2.16}$$

Where $\gamma_S^d, \gamma_S^p, \gamma_S^h, \gamma_S^i$ and γ_S^{ab} are the dispersion, polar, hydrogen, induction and acid-base components of the surface energy of a solid respectively, and all the remaining interactions are included in γ_S^o. Fowkes mainly carried out studies in which two-phase systems were involved and only dispersion interactions appeared, resulting in an expression to calculate the surface energy corresponding to the solid-liquid interaction, shown in equation (2.17).

$$\gamma_{SL} = \gamma_S + \gamma_L - 2\sqrt{(\gamma_S^d \gamma_L^d)} \tag{2.17}$$

This equation can also be written as equation (2.18).

$$0.5\gamma_L(1 + cos\,\theta_Y) = \sqrt{\gamma_S^d \gamma_L^d} \tag{2.18}$$

This equation allows the calculation of the surface energy of a nonpolar solid ($\gamma_S = \gamma_s^d$). Furthermore, if the measuring liquid can be characterized only by the dispersion interaction ($\gamma_L = \gamma_L^d$) the previous equation can be simplified to equation (2.19).

$$\gamma_s = 0.25\gamma_L(1 + cos\,\theta_Y)^2 \tag{2.19}$$

From these equations, the dispersive surface energy component of any solid can be determined as long as the dispersive component of the measuring liquid and the contact angle are known.

This method is being used for the determination of the surface energy of polymeric materials [49], and particularly recommended for nonpolar materials, always keeping in mind that this method is based on the independence and the additivity of both dispersion and polar interactions.

The next theory arose from the study performed by different authors. Concretely, Owens-Wendt-Rable & Kaeble (OWRK) [15] went further and stated that all the different interactions presented by Fowkes, excluding the dispersive one, can be associated with the polar interaction. This fact is represented in the OWRK equation (2.20).

$$\gamma_{SL} = \gamma_S + \gamma_L - 2\left(\gamma_S^d \gamma_L^d\right)^{0.5} - 2\left(\gamma_S^p \gamma_L^p\right)^{0.5} \tag{2.20}$$

When combined with Young's equation, the OWRK equation can be written as (2.21).

$$0.5\gamma_L(1 + cos\,\theta) = 2\left(\gamma_S^d \gamma_L^d\right)^{0.5} - 2\left(\gamma_S^p \gamma_L^p\right)^{0.5} \tag{2.21}$$

Since this method considers two main interactions, at least two liquids with known dispersive and polar parts of the surface tension are required. A liquid with a dominant polar component is used as one measuring liquid and a liquid with a dominant dispersive component is used as the other one. In this way, the contact angle is measured using these two measuring liquids and the unknowns γ_S^d and γ_S^p will be solved.

The OWRK method is one of the most common methods for surface energy calculations and it is usually used to investigate the polar and dispersive interaction effect on wettability and adhesion processes. In particular, the contact between surfaces of different polarity and the effect of the change in polarity can be assessed and optimized in processes such as printing, painting, bonding and hydrophobic or hydrophilic coating. The most common polar liquid used in many studies is water, followed by Glycerol and Formamide, and the dispersive one is Diiodomethane as well as α-bromonaphthalene. Thus, the set water-diiodomethane is used most frequently as the measuring liquids.

Wu [50], [51] follows the idea provided by the OWRK method, which consists on dividing the surface energy of a solid into two components, the polar and the dispersive part. In order to calculate the surface energy from the contact angle data, the interfacial

tension γ_{SL} must be determined. Based on the Fowkes method, the interfacial tension is calculated based on the surface energy of the solid γ_S and the surface tension of the liquid γ_L and the similar interactions between the phases which are interpreted as the harmonic mean of the dispersive γ^d and polar part γ^p of the surface energy of the solid or the surface tension of the liquid (2.22).

$$\gamma_{SL} = \gamma_S + \gamma_L - 4\left(\frac{\gamma_S^d \gamma_L^d}{\gamma_S^d + \gamma_L^d} + \frac{\gamma_S^p \gamma_L^p}{\gamma_S^p + \gamma_L^p}\right) \tag{2.22}$$

This equation can be written also in combination with Young's equation to relate the different component with the contact angle (2.23).

$$0.25\gamma_L(1 + cos\,\theta) = \left(\frac{\gamma_S^d \gamma_L^d}{\gamma_S^d + \gamma_L^d} + \frac{\gamma_S^p \gamma_L^p}{\gamma_S^p + \gamma_L^p}\right) \tag{2.23}$$

This method also requires the use of two liquids with the known dispersive and polar components in order to calculate both components of the surface energy of the material, γ_S^p and γ_S^d.

This method is often used for calculating the surface energy of polymers with low surface energy. The set of liquids which is also commonly used are water-diiodomethane. From a theoretical point of view, the geometric mean is more accurate than the harmonic one.

Another theory is the one developed by Van Oss-Chaudhury-Good [52]–[55]. This method is based on the acid-base approach for calculating the surface energy of a solid from the contact angle with several liquids, dividing the dispersive part of the surface energy into a Lewis acid part (+) and a Lewis base part (-).

The interfacial tension is also the unknown parameter and it is then calculated based on the surface tension of the liquid γ_L, the surface energy of the solid γ_S and the interactions between phases. In contrast to the previous method, these interactions are interpreted as the geometric mean of a dispersive part γ^d and the corresponding acid parts γ^+ and base parts γ^- of the surface tension or the surface energy of the solid (2.24).

$$\gamma_{SL} = \gamma_S + \gamma_L - 2\left(\sqrt{\gamma_S^d \gamma_L^d} + \sqrt{\gamma_S^- \gamma_L^+} + \sqrt{\gamma_S^+ \gamma_L^-}\right) \tag{2.24}$$

The surface energy can then be obtained according to equation (2.25).

$$0.5\gamma_L(1 + cos\,\theta)\left(\sqrt{\gamma_S^d \gamma_L^d} + \sqrt{\gamma_S^- \gamma_L^+} + \sqrt{\gamma_S^+ \gamma_L^-}\right) \tag{2.25}$$

Since there are three unknown quantities, γ_S^d, γ_S^- and γ_S^+, this method requires the use of three different liquids to measure the contact angle of the studied material. One dispersive liquid and two polar liquids with known acid and base parts should constitute the three measuring liquids.

This method is one of the most recently developed methods in the field of calculating the surface energy of solids. The information given about the surface properties is more

accurate, but it is very sensitive to small variations in the contact angle measurement or to the properties of the liquids used.

Lastly, the method developed by Zisman [56] is rather different from the previous methods since it determines the so-called critical surface energy γ_C. This method defines the critical surface energy of a solid as being equal to the value of the surface tension of the highest surface tension liquid that will completely wet the solid, with a contact angle of zero. The value of γ_C differs from γ_S and it is not divided into dispersive and polar components.

The value of the critical surface energy is determined by measuring the contact angle between several different measuring liquids and the solid surface under study. Then, a plot is constructed having the cosine value of the contact angle ($\cos\theta$) in y-axis and the values of the liquid tension of the measuring liquids (γ_L) in the x-axis as shown in Figure 2.10.

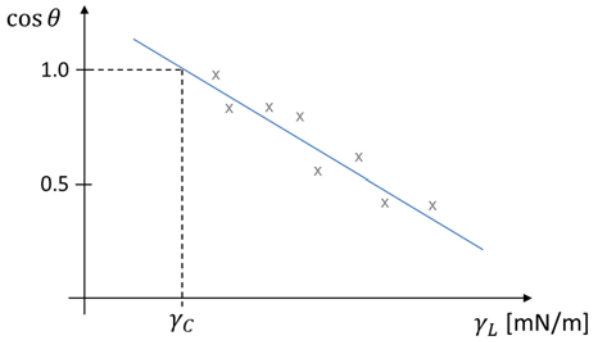

Figure 2.10 Determination of the critical surface energy of the solid (γ_C) under measurement with different measuring liquids.

Usually, the Zisman method works best for non-polar surfaces and it is noted that the interaction between the phases is not taken into account.

After the overview of the different available methods to evaluate the surface energy of a solid by the previous measurement of the contact angle, the next step consists in introducing the main techniques used nowadays to perform topographic measurements. As in this Ph.D. Thesis the measurement of the contact angle will be performed with a developed measurement method that uses a topographic device, specifically a profilometer, a brief overview of these techniques will be made.

2.2.2. Measurement techniques used by profilometers

When characterizing a surface, distinction must be made between methods for evaluating the nanoscale to atomic scale and methods for evaluating the microscale, more especially if surface roughness is involved. On the one hand, physicists and physical chemists often require details at the molecular level which are provided by methods such as low-energy electron diffraction, molecular-beam methods, field-emission and field-ion microscopy, scanning tunneling microscopy and atomic force microscope [57]. On the other hand, engineering and manufacturing surfaces companies are only interested in

characterizing at microscopic level. In such cases, the use of microscopic methods, mechanical or optical, are sufficient. Such methods include coordinate measuring machines and the stylus contact profiler and are also capable to measure geometrical parameters of the surfaces.

The measurement of the roughness of surfaces can be divided into two main groups. The methods based on direct contact between the device and the sample under test and the non-contact methods. The benefit of the noncontact method is that the device does not damage the sample since there are no mechanical parts touching the sample.

Contact methods include the scanning probe microscopes, i.e. scanning tunneling microscope and atomic force microscope, the coordinate measuring machines and the stylus contact profilers. Among the noncontact methods, we can differentiate between two different techniques. First, the single point technique in which techniques such as triangulation, confocal, confocal chromatic and interferometry are included. Second, the imaging techniques in which fringe projection deflectometry, holography as well as confocal and interferometry are included. All these cited noncontact methods are considered to be optical methods which are based on the utilization of a light wave to illuminate the surface under test and the analysis of the light reflected by the surface to obtain the information of interest.

When speaking of reflected light, it is important to differentiate between surface types. The reflection of the light can be specular, diffuse or both, and depends on the kind of surface that is being illuminated. As shown in Figure **2.11**, when the light illuminating a surface is specularly reflected, the surface is considered microscopically smooth. On the other hand, if the reflection is diffusive in many directions, this means that the surface is considered microscopically rough.

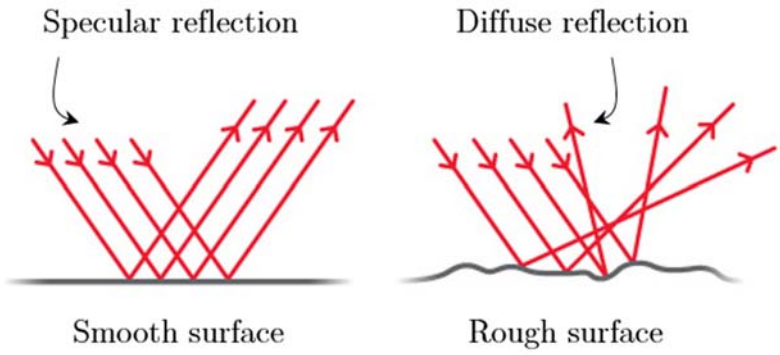

Figure 2.11 Representation of the behaviour of a smooth and a rough surface respectively when illuminated by a light source. The smooth surface leads to a specular reflection and the rough surface to a diffuse reflection.

In this last case, due to the fact that each ray meets a part of the surface which has a different orientation, the normal vector at the point of incidence is different for different

rays. Subsequently, when the individual rays reflect off the rough surface according to the laws of reflection, they scatter in different directions.

As we introduced previously, this Ph.D. Thesis falls within the field of the confocal technique, specifically in the use of a device based on the confocal technique to obtain the contact angle and the further evaluation of the surface energy of a solid surface in the same measurement area. In this section, we will therefore outline the main characteristics of the confocal technique as well as its strengths in non-contact topographic measurements comparing with other available techniques.

This section will also include a detailed explanation about the interferometric technique. The reason why we emphasized this technique is that at the begging of this Ph.D. Thesis, we intended to use interferometry as the measurement technique. As detailed in Appendix A, we needed to change to the confocal technique mainly due to the limitations of interferometry for the requirements of the presented developed method.

2.2.2.1. Confocal technique

The confocal technique [58] is based on illuminating only the area that is in the focal point of the lens, which is a small zone of the sample to be imaging. The confocal technique is a double pass technique in which the optical surfaces are crossed two times. For example, in conventional microscopies, which are single pass techniques, the image of a point light source corresponds to its corresponding Airy disk. On the other hand, when working with confocal microscopies the image of the same point light source corresponds to the image of the Airy disk, this means a narrower diffraction pattern, as shown in Figure 2.12.

(a) (b)

Figure 2.12 Airy pattern obtained by a (a) conventional microscope and a (b) confocal microscope. Source: [58]

According to Rayleigh's criterion, the resolution of a microscope is defined as the minimum distance between two points that can be distinguished in an image, this means when the first minimum of one of the Airy disks coincides with the central maximum of the adjacent Airy disk. This technique is characterized by creating an image of a sample only with light coming from points of the sample that are in focus so the axial response plays an important role. The axial response is defined as the response of the system to take measurements in the z-direction, i.e. in the direction of propagation of the light, consequently, the numerical aperture (NA) of the microscope objective is also involved.

The narrow axial response allows obtaining better detailed images because the light coming out of the focal point will not be detected and therefore, the use of microscope objectives with high NA will improve them. The dependence of the axial response with the NA of the optics is shown in Figure 2.13.

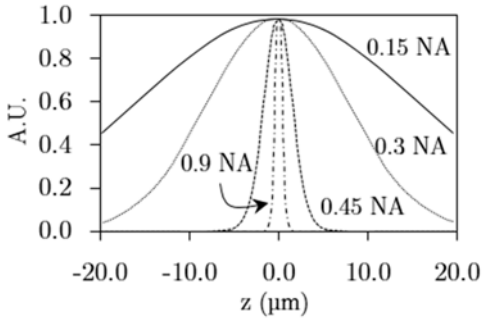

Figure 2.13 Axial response of microscope objectives with different numerical apertures. Narrower axial responses of high values of NA means less light coming from points out of focus. Source: [58]

If the optics of the system has a small NA, the axial response will be wide and the resolution of the final image will decrease considerably. It is important to highlight that a narrow axial response, i.e. high NA, and a small pinhole are very good tools to improve the images given by a confocal system.

A confocal image is a very high contrast image obtained by this technique in which only the parts of the sample that are in focus are illuminated at a time, which means that only these parts are in the focal plane. Due to this fact, the final image, which is a composition of all the different taken images of parts that are in focus, is a really contrasted image and it has much more resolution than an image taken with a conventional microscope.

A representative confocal microscope is shown in Figure 2.14. Usually, a confocal microscope uses a point source such as a LED and the light coming from it first passes thought a beam splitter and subsequently by a microscope objective. Only the areas of the sample that are at the focus plane will be illuminated and this light will be reflected back to reach the detector.

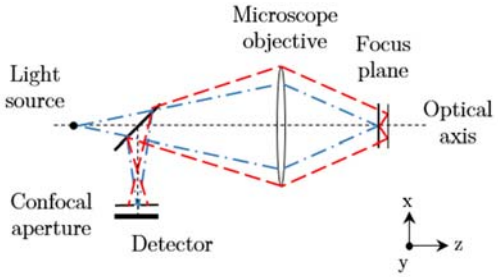

Figure 2.14 Schematic representation of a confocal microscope.

The beam splitter will guide the light reflected by the sample to the detector, which has a confocal aperture in front of it. In case there is light reflected by the sample which is not in focus, the confocal aperture will reject this light helping to finally obtain a more detailed image.

By scanning the sample in the z direction, different parts of the sample will be in focus at a time, which will allow the generation of 2D profiles of the sample if it is also scanned in x or y direction. In addition, it can generate 3D surface images if the sample is both scanned in x and y direction. With the further processing of these 3D surface images one can obtain any surface texture parameter found in ISO 25178 [59] such as the roughness of the surface and the real measured area which takes into account the roughness of the surface.

The confocal technique is widely used in biological science, such as cell biology, genetics and medicine but its strength lies in surface characterization.

Once the confocal technique introduced, now is time to present the interferometry, as it was the basis at the begging of this Ph.D. Thesis.

2.2.2.2. Interferometric technique

Interference is an optical effect, which can occur when two or more light beams are superimposed. There are some conditions to be fulfilled in order to achieve interference such as the spatial and temporal overlap of both light beams, which must be coherent and non-perpendicularly polarized.

Interferometers [60], [61] are optical devices which use the effect of interference to measure distances. Typically, a single input beam is used, which is split into two identical beams by means of an optical device such as a beam splitter. Each of these beams travels a different path through each arm of the interferometer and then recombine before arriving at a detector. The difference in distance travelled by each beam, called optical path difference, causes a difference in the relative phase of the two beams that is responsible for the creation of an interference pattern, shown in Figure 2.15. In the case where both beams are in phase, the resulting interference will be constructive (white) and on the contrary, the interference will be destructive (black).

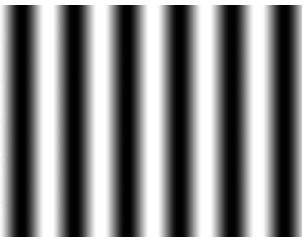

Figure 2.15 Representative interference pattern from a flat surface.

This cycle of the destructive and constructive interference causes the intensity of the recombined light to undergo a cyclic variation. One cycle of variation in intensity from

light to dark occurs every time the optical path difference (OPD) between beams reaches half a wavelength ($\lambda/2$) of the light used. In this way, the OPD can be measured as equation (2.26) shows.

$$OPD = \frac{\lambda}{2}N \tag{2.26}$$

where N is the number of fringes passed.

Currently, there are available a wide range of interferometers that can be organized by a variety of criteria. The most common one consists in grouping them into double path or common path interferometers and wavefront or amplitude splitting interferometers.

In a double path interferometer, the reference beam and the sample beam travel along different paths. Once they are perturbed by the interaction with the sample under test, the sample beam together with the reference beam recombine, forming an interference pattern from which the information about the surface under test will be extracted. Double path interferometers include the well-known Michelson interferometer as well as the Twyman-Green interferometer and the Mach-Zender interferometer, both shown in Figure 2.16.

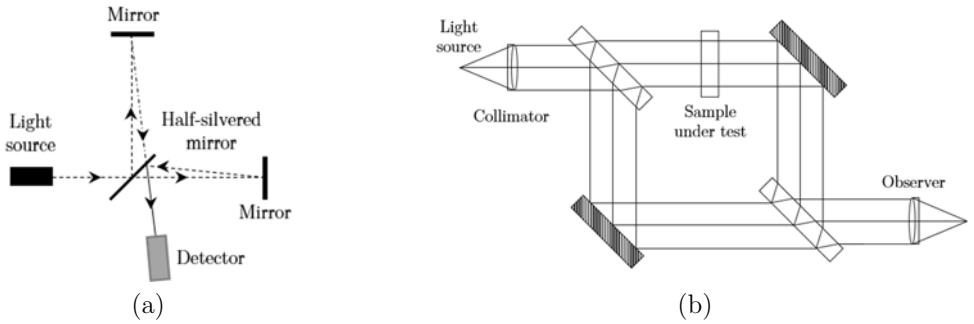

Figure 2.16 Schematic representation of (a) Michelson interferometer and (b) Mach-Zender interferometer, which are double path interferometers.

At the begging of this Ph.D. Thesis we were focused on the development of a measurement device based on a basic Twyman-Green interferometer, as the one shown in Figure 2.17, which is also classified as a double path interferometer. In this device, the interferometric pattern will result from the recombination of the reflected light on a reference and from the sample under test.

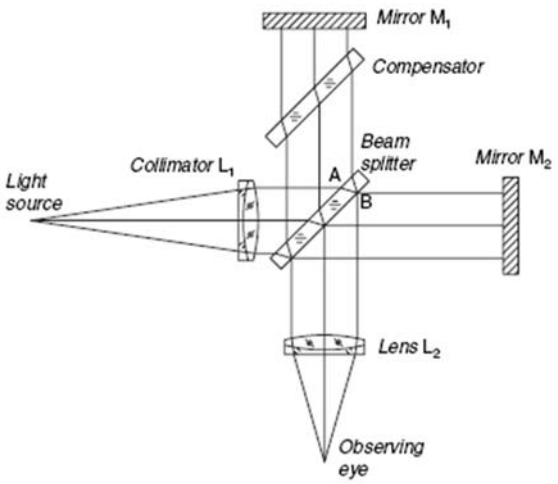

Figure 2.17 Representation of a Twyman-Green interferometer.

A common path interferometer [61] is a device in which the reference beam and the sample beams travels along the same general path. The optical path difference between the reference and the sample beam is zero in the center of the field of view, thus enabling the use of white light. In most common-path interferometers both the reference and the sample beam are affected by the aberrations and the interference is produced by the shearing of a beam with respect to the other. The shape of the aberrated wavefront is obtained by computation.

Sagnac interferometers, as the one shown in Figure 2.18, include devices such as scatter plates, Fresnel's biprisms, lateral shearing interferometers and Zernike phase contrast microscopes.

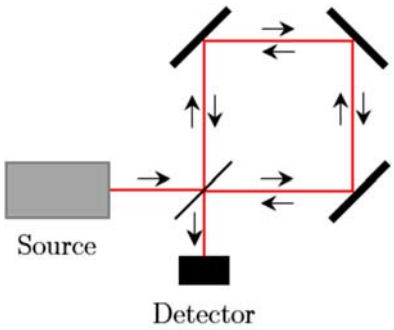

Figure 2.18 Representation of an exemplary common path interferometer known as Sagnac interferometer.

Regarding a different aspect of interferometers, they can be divided between wavefront splitting interferometers and amplitude splitting interferometers. Wavefront splitting interferometers divide the light wavefront coming from a point or a narrow slit. When the two parts of the wavefront travel through different paths, they recombine creating the interference pattern. Young's interference experiment and Lloyd's mirrors are examples of

these types of interferometers. In addition, the Fresnel's biprism, as shown in Figure 2.19 and the Rayleigh interferometer are included in this type of interferometers.

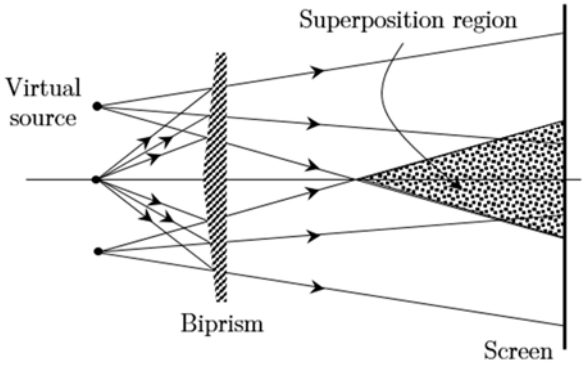

Figure 2.19 representation of an exemplary wavefront splitting interferometer known as Fresnel's biprism.

An amplitude splitting interferometer uses a partial reflector to divide the amplitude of the incoming beam into two separated beams that after travelling each path, recombine. Fizeau, Mach-Zehnder, Fabry-Pérot, Michelson and Twyman-Green interferometers are part of this category.

Interferometric devices apply the effect of the interferometry by different available techniques from which coherence scanning interferometry (CSI) is the most common and is most commonly known as vertical scanning interferometry (VSI) or white light interferometry. Other common techniques are available as the well-known phase shifting interferometry (PSI) and also there are interferometric microscopes objectives that are commonly used in the optical profiling interferometers.

The VSI technique, as shown in Figure 2.20 [62], is based on the use of white light source to achieve fringe localization. It refers to an optical surface measurement method wherein the localization of the interference pattern when scanning the optical path length allows the determination of the topography and optical properties of smooth to moderately rough surfaces with nanometer resolution [63].

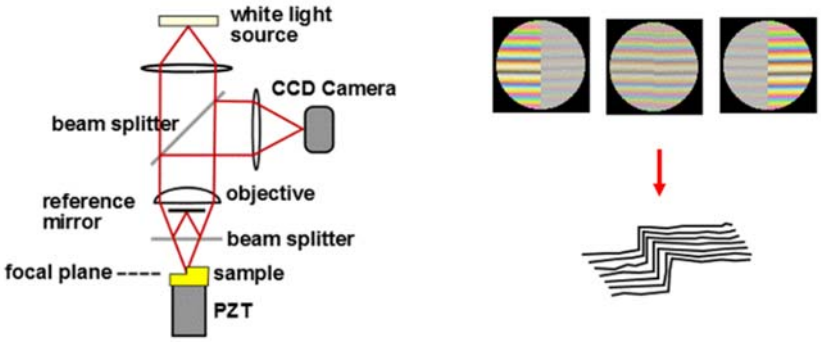

Figure 2.20 Representation of a vertical scanning interferometer with different recorded interferograms at different positions of the sample and the corresponding surface reconstruction.

White light interferometry is the basis of the VSI technique. Currently, most of the interferometric measurements are performed with the use of a laser light since the longer coherence length makes it easier to obtain the interference fringes. Also, compared with the use of the shorter coherence length of a white light source, the matching of the optical path of the interferometer is easier when using a laser. However, the use of a laser light to obtain interference fringes is not as good as it seems. The long coherence length of this light source can also be detrimental, resulting in interference with spurious reflections that will lead to incorrect measurements.

As explained, the use of a short coherence length white light source requires a more accurate match of the optical path of the interferometer to obtain interference fringes, but it results in an extremely high contrast interference pattern. For that reason, the use of this kind of light source can be considered as an advantage.

Phase shifting interferometry (PSI) [64]–[66], shown in Figure 2.21, is based on the introduction of a time-varying phase shift between the reference wavefront and the test or the sample wavefront in the intereferometer. This produces a time-varying signal at each measurement point in the interferogram and the relative phase between the two wavefronts at that location is encoded in the intensity pattern.

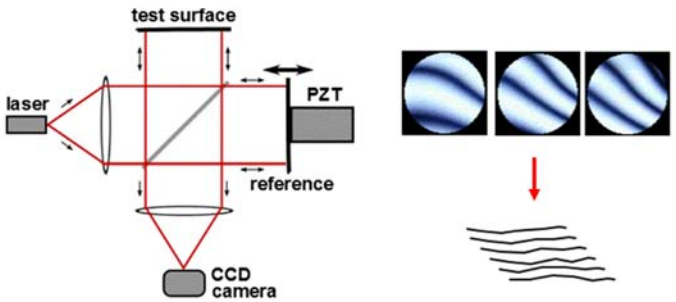

Figure 2.21 Representation of a phase shifting interferometer with different recorded interferograms and the corresponding surface reconstruction.

The PSI technique uses a monochromatic light source and provides surface height measurements of very smooth and continuous surfaces with sub-nanometer resolution. The application of this technique includes optical testing and real time wavefront sensing for active optics and microscopy.

Classically, the information from interference patterns is obtained by measuring the positions of the fringe centers and additional information is needed to correctly read the interferogram. For example, in a static interferogram which deviates from flatness, one cannot verify if it is due to a concave or a convex surface. PSI overcomes this issue since the movement direction of the fringes can be observed in real time while the reference surface is being measured. It does not rely on finding the fringe centers of the interferograms but rather recovering the phase data from collecting intensity data point-by-point.

The application of interferometric techniques has reached fields such as astronomy [67], [68] and biology with the development of the optical coherence tomography (OCT) [69], [70]. The main application of interest is the measurement of slight deviations of an optical surface that leads to the topography measurement with an accuracy better that an optical wavelength. This technique is also applicable to measuring the wavelength of a laser beam, monitoring slight changes in an optical wavelength of frequency by means of a Fabry-Pérot interferometer, measuring rotations by means of a Sagnac interferometer, measuring distances or changes of a distance or a position or the measurement of the chromatic dispersion of optical components as an optical filter.

After this theoretical introduction about the most relevant techniques currently used to perform 3D non-contact topographic measurements and since this Ph.D. thesis comes within the framework of an industrial Ph.D. the next section will present a benchmarking. We will give a broad overview about the current instruments that are available in the market in the field we are working on, regarding contact angle and surface energy measurements and devices to perform topographic measurement based on the techniques introduces before.

2.3. Benchmarking

The presented benchmarking consists in two main subsections. The first subsection is devoted to the main companies that supply complete equipment to perform contact angle measurement and the corresponding surface energy evaluations. The second subsection collects information about the main companies that supply equipment to perform contactless surface's profile measurements based on the previous introduced techniques currently used to perform these measurements.

2.3.1. Suppliers and devices to perform contact angle measurement and surface energy evaluation

Currently available devices in the market allowing the measurement of the surface energy perform the measurement indirectly. This means that the contact angle must be previously measured to be able to evaluate the surface energy. These devices are basically

contact angle meters whose function consists in measuring or evaluating the contact angle between a solid surface and a liquid which is placed on said surface. With the calculated contact angle, the evaluation of the surface energy of the surface can be carried out.

One of the best known contact angle meters suppliers is KRÜSS [71]. It has a wide range of products with different capabilities but they all share the same basic functionality: they allow the measurement of the contact angle and the surface energy of the surface under test with the same device.

The methodology of these devices for the measurement of the contact angle is based on drop shape analysis, generally from a lateral image of the drop. Sessile drop, pendant drop and extension/contraction method are among the most commonly used methods, and more complex methods such as Wilhelmy plate or top-view reflection method are also used.

The commercial portfolio includes a large variety of devices to perform the contact angle and surface energy measurement depending on the application requirements, as the ones shown in Figure 2.22. Fully and partially automated devices are presented, with a width angle measuring range and high accuracy and single and multiple dosing units are available in different devices to obtain a full energy surface evaluation. What is striking is the availability of portable devices whose accuracy is as high as the one from laboratory devices.

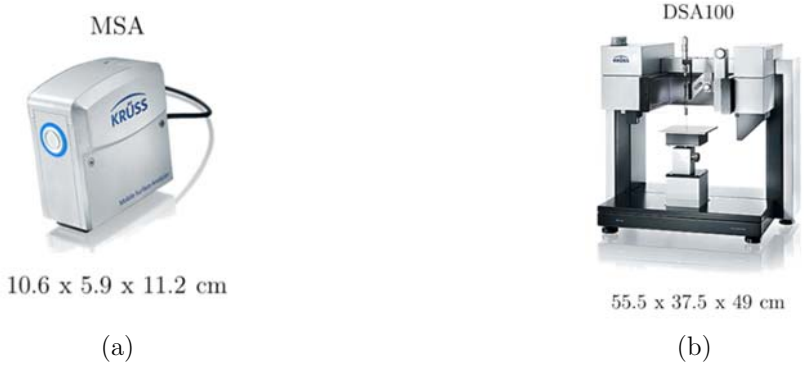

Figure 2.22 Representative devices from KRÜSS to measure the contact angle and the surface energy of a solid by means a (a) portable device and (b) Laboratory device.

KYOWA [72] is a Japanese company with the same purpose as the previous suppliers. In this case, in addition to accurate devices for contact angle measurements in regular sample size, KYOWA offers a wider range of devices which are aimed at measuring contact angles involving large surface area. Furthermore, they also offer a portable device to measure the contact angle and the surface energy as shown in Figure 2.23.

(a) (b)

Figure 2.23 Representative devices from KYOWA. (a) Portable device and (b) laboratory device both for measuring the contact angle, surface energy of a solid and the interfacial tension.

The methods present in most of the devices for calculating the contact angle are commonly the sessile drop, extension/contraction, sliding and three-state method and for the calculation of the surface or interfacial tension the main method is the pendant drop.

Dyne Testing [73] is the supplier with the narrower choice of products focused on the measurement of the contact angle and the surface energy, as the ones shown in Figure 2.24. On the other hand, their products have a wider range of applications for accurate and easy measurement of other properties of a surface such as the wettability, adsorption, spreading, and heterogeneity, including also the dynamic contact angle and the surface and interfacial tension. The offer also includes a portable device to measure only the contact angle, but the accuracy and the measured angle range is maintained with respect to the laboratory devices.

(a) (b)

Figure 2.24 Representative devices from Dyne Testing. (a) Portable device for measuring the contact angle. (b) Laboratory device for measuring the contact angle, surface energy of a solid and the interfacial tension.

At has been commented, this Ph.D. Thesis is located in a field under constant developement and it is of a great interest to the scientific community and to the market. During the development of this Ph.D. Thesis a new device appeared on the market that combines the measurement of the topography of a surface with the evaluation of the surface energy with a single device.

This device marketed under the name Attension Theta Topography, shown in Figure 2.25, by Biolin Scientific [74] and Dyne Testing [75] allows to correct the effect of the surface topography on the measurement of the contact angle according to Wenzel's model, which matches the goal of this Ph.D. Thesis.

Figure 2.25 Attension Theta Topography from Biolin Scientific and Dyne Testing. First device which allows the correction of the effect of the roughness of the surface in the contact angle measurement with a single device, but with a displacement of the sample between measurement modules.

By the modification of a previous available device, named Theta Optical Tensiometer, they introduced an external module able to perform topographic measurements from top-view by means of the fringe PHI technique. Once the topography is measured, the sample, which is placed in the sample holder of this module, is displaced from there to the place where the measurement of the contact angle will be performed with side view imaging. Although the displacement between these two positions is performed automatically by means of very accurate motors, we face the same current problem, which is the uncertainty of the sample positioning between the two modules of measurement.

2.3.2. Suppliers and devices to perform 3D non-contact profilometry measurements

In the field of 3D non-contact profilometers, a wide variety of companies offer products based on the measurement of the profile or the topography of a surface without any contact between the device and the sample under test.

Nanovea [76] designs and manufactures instruments providing solutions for profilometry based on chromatic confocal optical technology which gives the highest accuracy of all the optical techniques in this field in the nanometer range. Furthermore, if sub-nanometer accuracy is needed, Atomic Force Microscope integration is available for applications that also require nanometer range lateral resolution. Their commercial portfolio includes different setups mainly depending on the application and the size of the sample under test, including a portable optical profilometer, shown in Figure 2.26. On the other hand, the provided software allows to perform different measurements such as roughness, texture,

profile and thickness in addition to the topography of the surface and to control the setup via computer.

(a) (b)

Figure 2.26 Exemplary 3D non-contact profilometers from Nanovea. (a) Portable device, (b) Laboratory device to scanning samples up to 1x1 m

Sensofar [77] is a company specialized in developing, manufacturing and commercializing non-contact optical 3D profilometers. Its setups are based on confocal, interferometry and the focus variation technique to ensure the most accurate surface reconstruction. Different devices configuration are possible, as the ones shown in Figure **2.27**, to perform measurements of big size surfaces and with a vertical resolution in the sub-nanometer range allowed by one of the previous techniques.

(a) **(b)**

Figure 2.27 Exemplary 3D non-contact profilometers from Sensofar. (a) Different configurations allows from portable to XXL systems of this device, (b) device devoted to measuring aspheric and free-form optics.

The software, besides controlling the device, allows to extract different information from the surface under study such as the roughness and texture.

Another supplier in this field is ZYGO [78] whose devices are based on white light, coherence scanning or phase shifting interferometry, offering fast and reliable 3D metrology of surface features, as the ones shown in Figure 2.28. Depending on the requirements of the measurement, the offer includes speed, automation, configuration flexibility and vertical range in the measurement with sub-nanometer vertical and sub-micron lateral

resolution. Just as the previous suppliers, the software allows data analysis for several features of the surfaces and the system control.

Figure 2.28 Exemplary 3D non-contact profilometers from Zygo.

Other suppliers such as Novacam [79], Alicona [80], Olympus [81], KLA tencor [82] also offer high quality devices to ensure high accuracy measurement of surface topography with basically the same named technologies. Figure 2.29 shows exemplary devices from these companies.

Figure 2.29 Exemplary 3D non-contact profilometers from (a) Novacam and (b) Alicona.

To summarize, with 3D non-contact profilometers high accuracy topographic measurements can be achieved, with sub-nanometer vertical resolution, by means of the main techniques used in this field, which are the confocal technique and interferometry.

Next chapter will introduce the relation of the roughness of a surface and its contact angle, as well as the impact of not taking into account this roughness on the calculations and the further evaluation of the surface energy.

3. Roughness and surface energy

3.1. Introduction

When measuring experimentally the contact angle of a solid surface by any method introduced in Chapter 2, we must keep in mind that we will obtain a contact angle value that corresponds to a macroscopic measurement and does not reflect only the chemical properties of the material under study. It is important to note that the way of wetting of a liquid on a solid surface depends not only on the properties of the liquid and the chemical properties of the solid surface but also on its physical structure.

Regarding Young's equation, it is demonstrated that the surface energy of a solid can be obtained from the measured contact angle since the surface tension of the liquid is already known, provided that the surface under measurement is chemically homogenous and topographically smooth. The equation used for this, introduced in Chapter 2 and stated by equation (2.19), is the following.

$$\gamma_s = 0.25\gamma_L(1 + cos\,\theta_Y)^2 \tag{3.1}$$

where θ_Y corresponds to the intrinsic contact angle of this surface. Conversely, when we measure the contact angle on rough surfaces, this measured contact angle is affected by the roughness of the surface. If we want to evaluate the surface energy of a rough surface by directly using this measured contact angle value in Young's equation, it will lead to an erroneous value since this equation has been developed for surfaces which are perfectly smooth.

Hence, if we want to perform the evaluation of the surface energy with as much reliability as possible from the measured, apparent contact angle, which reflects both the effects of the chemical composition and the structural component of the surface, we must be able to correct the influence of the roughness of the surface on this apparent contact angle. We will then obtain the corresponding intrinsic contact angle, which can be used in Young's equation to obtain the surface energy.

As will be explained throughout this chapter, the structure of a surface is of key importance in the framework of wetting studies and we will see that the micro and nano structure of a surface is directly related with the modification of the wetting properties of the surface.

Two different models will be introduced to obtain the intrinsic contact angle from the measured apparent contact angle as a function of two characteristic surface parameters of the surface under study to finally evaluate accurately the corresponding surface energy.

Furthermore, we will evaluate the error performed when calculating the surface energy with the apparent contact angle instead of the intrinsic contact angle for a given material.

3.2. The Wenzel model

Earlier in the twentieth century, Wenzel [83] started to evaluate the impact of the roughness, as well as the micro- and nano- structure of a surface, in the measurement of the contact angle on rough and chemically homogeneous surfaces.

Let us suppose a rough surface with a given microstructure. A liquid drop is placed on it and wets completely the contact surface as Figure 3.1(a) shows. According to Wenzel, the total contact area between the solid and the liquid must be taken into account when calculating the surface energy so the surface is characterized by the roughness ratio factor (r). This factor is defined as the ratio of the real solid-liquid area (A_{rough}), which takes into account the roughness of the surface, to its projection on a smooth surface (A_{flat}) as Figure 3.1(b) shows, and is always greater than 1 since no surface is completely smooth at the molecular range.

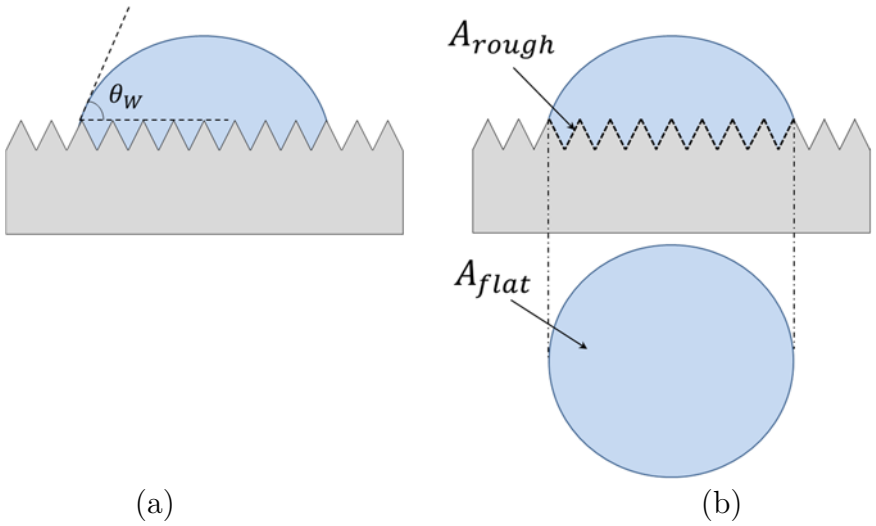

Figure 3.1 (a) Schematic diagram of Wenzel's apparent contact angle on a rough surface where the liquid droplet wets completely the surface of the solid; (b) schematic representation of the real area (A_{rough}) and the projected area (A_{flat}) of the droplet to calculate the roughness ratio factor r.

As the introduction of the roughness not only influences the surface energy of the solid surface but also its interfacial energy, adding the roughness ratio factor in Young's equation, where $\gamma_{SL} \rightarrow r \cdot \gamma_{SL}$ and $\gamma_S \rightarrow r \cdot \gamma_S$, we finally obtain Wenzel's equation.

$$\cos\theta_W = r \cdot \cos\theta_Y \tag{3.2}$$

where θ_W corresponds to the apparent contact angle measured on the surface. θ_Y remains as the Young's contact angle which corresponds to the intrinsic contact angle of this surface (the one we would measure if it were topographically smooth) and the effect of the roughness of the surface is corrected by the introduction of the roughness ratio factor.

If we depict the behaviour of this equation, plotted in Figure 3.2, we can easily differentiate between a hydrophilic and a hydrophobic region. In the first one, i.e. $\theta_Y < 90°$, for any θ_W measured the corresponding θ_Y will be always larger, $\theta_W < \theta_Y$, so this means that the introduction of roughness in the surface increases the hydrophilicity of the surface and the liquid will tend to wet further. For the hydrophobic region, i.e. $\theta_Y > 90°$, we get the opposite situation. For any θ_W measured, it will have associated a smaller value of θ_Y which means that the liquid will tend to wet less, so the surface becomes more hydrophobic.

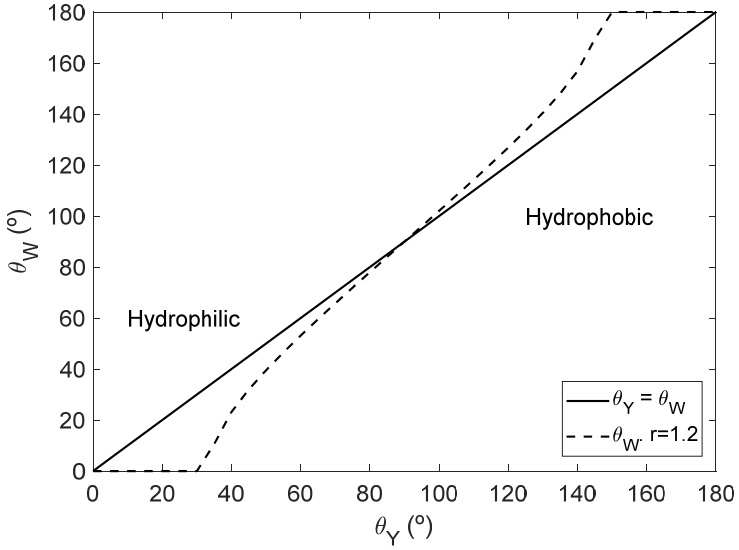

Figure 3.2 Representation of the measured Wenzel's apparent contact angle Θ_W as a function of the Young's contact angle Θ_Y for r=1.2 as an exemplary value.

Therefore, Wenzel's equation predicts that the introduction of roughness on a surface enhances its wetting properties since it makes a hydrophilic surface even more hydrophilic and a hydrophobic surface even more hydrophobic.

As our aim is to give an overview of how the roughness of a surface affects the measurement of its surface energy, we must go further in the study of how the modification of the roughness affects the contact angle.

Figure 3.3 gives an idea of the error introduced in the surface energy calculation when the roughness is not taken into account. It plots the θ_Y that corresponds to different measured contact angles (θ_W) as the roughness increases. It is clear the θ_Y only corresponds to θ_W for r=1, i.e. smooth surface. From then on, it is increasingly erroneous to associate θ_Y to θ_W.

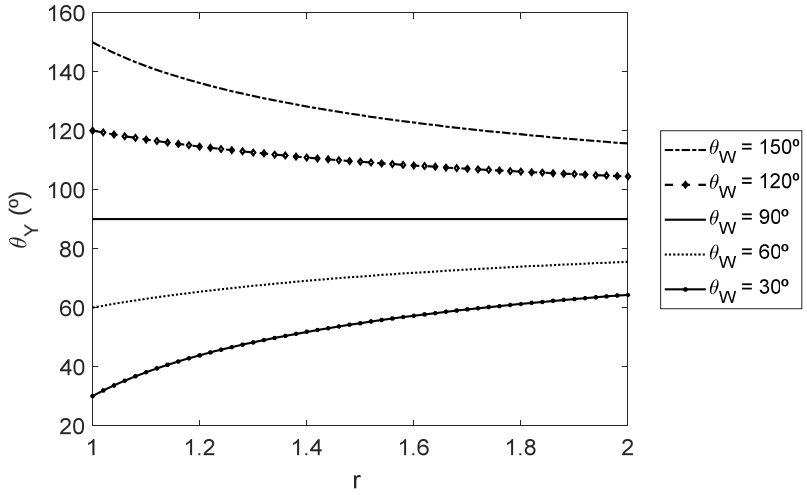

Figure 3.3 Representation of the intrinsic contact angle as a function of the roughness factor r for different apparent angles θ_W=30°, 60°, 90°, 120° and 150° in Wenzel's scenario.

As pointed out previously, Wenzel state tends to magnify the wetting properties of the surface under study. For $\theta_W > 90°$, $\theta_Y \leq \theta_W$ and as r becomes larger the difference between them also increases. On the other hand, for $\theta_W < 90°$, $\theta_Y \geq \theta_W$ so θ_Y becomes larger as r does.

This behaviour means that the introduction of roughness on surfaces enhances its wetting properties so for a surface that is not initially as hydrophobic or as hydrophilic as needed, one can compensate this lack of hydrophilicity or hydrophobicity making the surface rougher.

Once the effect of the roughness on the contact angle has been evaluated, it is time to consider how this effect impacts the evaluation of the surface energy and the error it introduces when the roughness is not taken into account.

From the bibliography, we can obtain standard values for the surface energy for some materials with different wetting properties in specific measurement conditions [84] as well as the surface tension values for common test liquids for surface energy analysis [85]. For this case of study, we selected two surfaces with different surface energy values in the hydrophilic and hydrophobic regime respectively, and water and Diiodomethane as measurement liquids since they are the most common test liquids in wettability studies. With these parameters we can obtain the theoretical intrinsic contact angle through Young's equation for water (WCA) and for the Diiododmethane (DCA) for each surface. All of these parameters as well as the respective contact angles are contained in Table 3.1.

Table 3.1 Values of the surface tension (γ_L) of water and Diiodomethane, surface energy (γ_S) of the hydrophilic and hydrophobic surface and the calculated values of the water contact angle (WCA) and Diiodomethane contact angle (DCA) at 20°C.

	$\gamma_L\ (mN/m)$		Hydrophilic surface	Hydrophobic surface
Water	72.8	$\gamma_S\ (mN/m)$	41.1	12.0
Diiodomethane	50.8	$WCA\ (°)$	59.8	100.8
		$DCA\ (°)$	37.0	91.6

In Figure 3.4 we can compare the evaluation of the surface energy by taking or not into account the roughness of the surface for a hydrophilic and a hydrophobic surface. For a hydrophilic surface, it is easily seen that when we calculate the surface energy without correcting for the roughness of the surface, the obtained value (γ_S Water or γ_S Diiodomethane) is always larger than the intrinsic surface energy (γ_S). This means not considering the roughness of a surface when evaluating its surface energy induces to overestimate its value. The error becomes larger as the roughness increases.

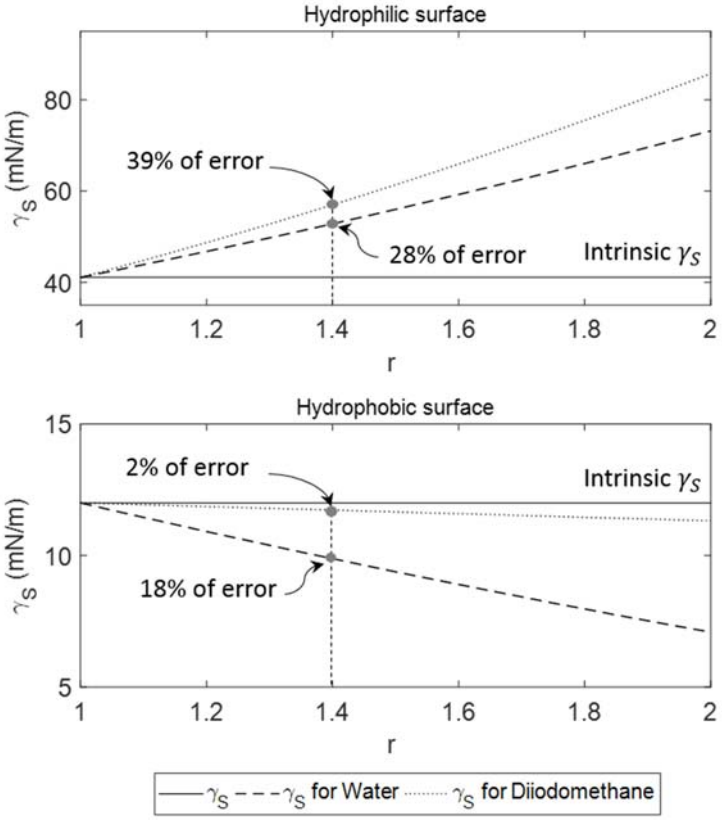

Figure 3.4 Evaluation of the surface energy for a hydrophilic and a hydrophobic surface for water (γ_S water) and Diiodomethane (γ_S Diiodomethane) as measurement liquids, not taking into account the roughness of the surface, compared to the intrinsic surface energy value (γ_S).

For a moderately rough surface (r=1.4), we can see that the error introduced for not considering the roughness of the surface is 28% when measuring with water and the error when measuring with Diiodomethane is 39%. The surface energy is overestimated so the surface would appear more hydrophilic than it really is and the error obviously gets worse for larger values of r.

On the other hand, the value of the surface energy for a hydrophobic surface when not taking into account the effect of the roughness is underestimated. The introduction of the roughness makes the surface to behave more in a more hydrophobic manner, so the value estimated for the surface energy directly with Young's formula would be lower than it really is. For r=1.4, the introduced error is lower than in a hydrophilic surface but for water it is 18% and for the Diiodomethane, 2%, getting worse for larger values of r.

It is important to keep in mind that the surface energy should be evaluated with at least two contributions, the dispersive and the polar one. The behaviour previously plotted can be associated to each of these contributions separately, i.e. the dispersive and the polar component of the surface energy. The evaluation of the total surface energy will strongly depend on the weight of each of these components.

If both the dispersive and polar components are in the hydrophobic or in the hydrophilic regime, since Wenzel model predicts an enhancement of the wetting of both hydrophobic and hydrophilic properties, this behaviour would be more remarkable. Otherwise, for example, if the contact angle of the polar part is larger than 90° and the contact angle of the dispersive part is smaller than 90°, one effect will compensate the other and the calculated surface energy will not deviate so much from the real one.

This simple example verifies the influence of the roughness of a surface in the measurement of its wetting properties, and highlights the importance to know the roughness of the surface to be measured when measuring its surface energy.

3.3. The Cassie Baxter model

After Wenzel developed the calculation of the intrinsic contact angles on rough and homogeneous surfaces, Cassie and Baxter [86] came with a new approach for solids which are chemically heterogeneous, so their chemical composition is of at least two different chemical substances which will also influence the wetting properties of the surface.

What Cassie and Baxter proposed is a way to calculate the intrinsic contact angle from the apparent measured one on surfaces that consists of n different type of materials. They considered that any of these materials are randomly distributed on the surface and have associated a fraction of the material (f_i) on the surface as well as their own surface energies $\gamma_{i_{SL}}$ and γ_{i_S}.

In this scenario, if we consider the fraction associated to each material and we introduced it in Young's equation where $\gamma_S \rightarrow \sum_i^n f_i \cdot \gamma_{i_S}$ and $\gamma_{SL} \rightarrow \sum_i^n f_i \cdot \gamma_{i_{SL}}$, we finally obtain the Cassie-Baxter's equation.

$$\cos\theta_{CB} = \sum_{i}^{n} f_i \cdot \cos\theta_{i_Y} \tag{3.3}$$

This equation relates the apparent measured contact angle with the intrinsic contact angles taking into account the fraction of each material that composes the surface of the solid and is in contact with the liquid.

Cassie and Baxter also introduced the way to determinate the fractions f_i of the material [86] by first determining the geometry of the structure of the surface.

In an easier scenario where the solid surface consists of two different component materials, 1 and 2 as shown in Figure 3.5(a), whose fractions are f_1 and f_2, where $f_1 + f_2 = 1$, and their intrinsic contact angles are θ_{1_Y} and θ_{2_Y}, the Cassie Baxter equation can be simplified as equation (3.4) shows.

$$\cos\theta_{CB} = f_1 \cdot \cos\theta_{1_Y} + f_2 \cdot \cos\theta_{2_Y} \tag{3.4}$$

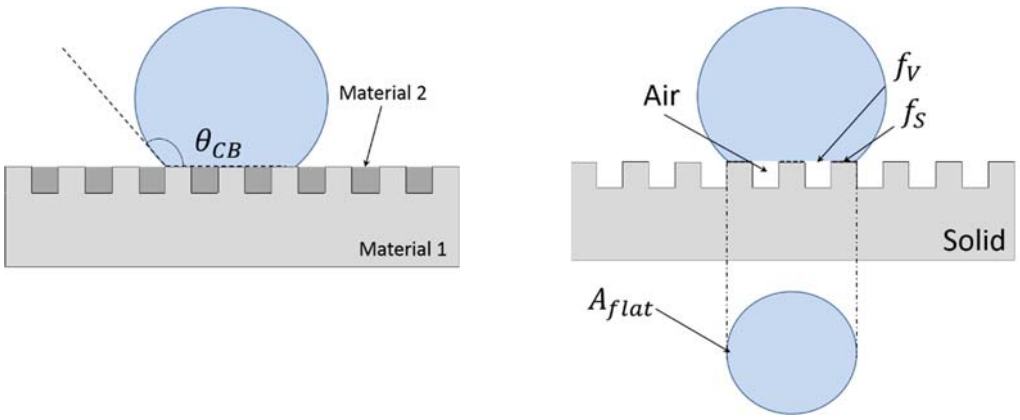

(a) (b)

Figure 3.5 (a) Schematic diagram of Cassie Baxter's apparent contact angle on two component materials; (b) schematic representation of a droplet sitting on trapped air bubbles f_V between the fractions of the material f_S which represents the lotus effect and its projected area (A_{flat}) on a smooth surface.

Following the previous state, for a given surface with a specific structure of one material, it can be possible that air bubbles become trapped between the fractions of the material as Figure 3.5(b) shows. In this situation, the wetting state can also be described by Cassie-Baxter's model with the solid material as material 1 and the trapped air bubbles as material 2.

In this case, one of the fractions is given by the liquid-air interface characterized by $f_1 = f_V$ and $\theta_{1_Y} = 180°$, since the fraction is fully dry so there is no contact between the liquid and solid. The other one is given by a solid-liquid interface characterized by $f_2 = f_S$, which represents the fraction of liquid in contact with the solid with its corresponding contact angle $\theta_{2_Y} = \theta_Y$. In this state, Cassie-Baxter's equation is expressed as in

equation (3.5) and its apparent contact angle depends on the percentage of solid which is in contact with the droplet.

$$cos\,\theta_{CB} = -f_V + f_S \cdot cos\,\theta_Y \tag{3.5}$$

As $f_V + f_S = 1$, then $f_V = 1 - f_S$ the Cassie-Baxter equation can be described as equation (3.6) shows.

$$cos\,\theta_{CB} = f_S \cdot (r \cdot cos\,\theta_Y + 1) - 1 \tag{3.6}$$

If we represent the evolution of Young's angle with respect to the Cassie-Baxter apparent angle for given values of r and f_S, shown in Figure 3.6(a), we can see that the apparent angle will always be larger than θ_Y. Also, as f_S increases, the difference between θ_{CB} and θ_Y decreases for a constant value of r. This is quite intuitive sine when f_S increases, the volume fraction corresponding to trapped air decreases. When f_S is small however, CB model predicts very large apparent contact angles even for materials with very low intrinsic hydrophobicity.

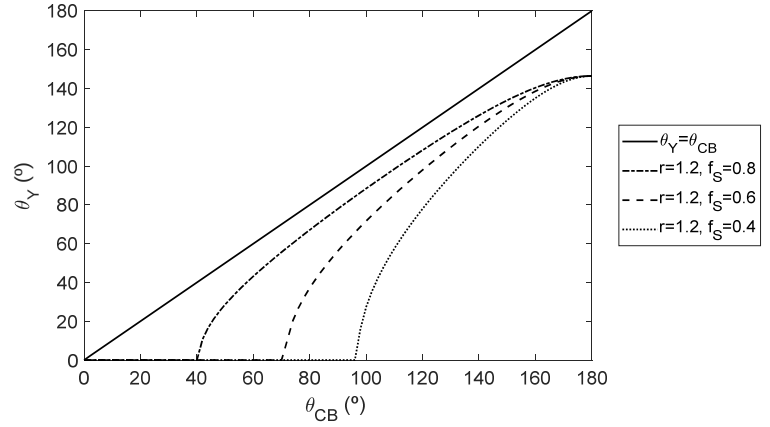

(a)

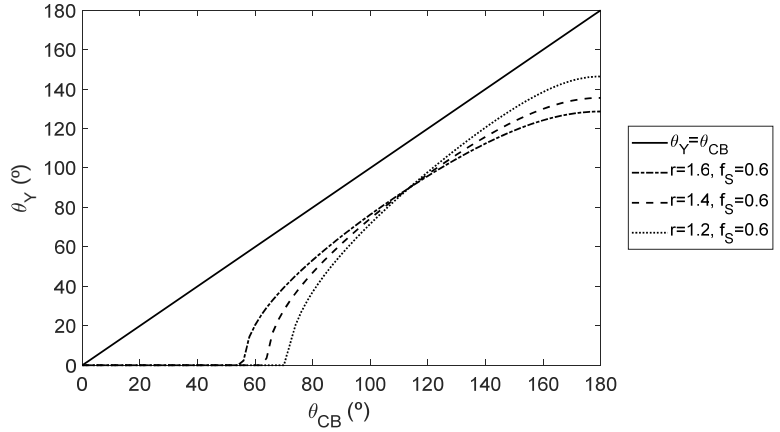

(b)

Figure 3.6 Representation of the Cassie Baxter's apparent contact angle Θ_{CB} as a function of the Young's contact angle Θ_Y for (a) $r = 1.2$ and $f_S = 0.4$, 0.6 and 0.8 as exemplary values, (b) $f_S = 0.6$ and $r = 1.2$, 1.4 and 1.6 as exemplary values.

The second section of Figure 3.6 shows the relation between θ_Y and the apparent contact angle for different roughness values at a given f_S value of 0.6. It allows us to glimpse the influence of microstructure geometry upon the hydrophobicity of the surfaces. For intrinsically hydrophilic materials, the less rough the microstructure for a given fraction of trapped air, the less hydrophilic they become. Conversely, for intrinsically hydrophobic materials, the rougher the surface for a given fraction of trapped air, the more hydrophobic they become.

As Figure 3.7 shows, for low values of f_S which means there is lot of air trapped, the behaviour of the surfaces are not hydrophilic anymore even for low values of θ_Y for low roughness. Therefore, according to Cassie Baxter, low contact angles cannot be possible for low values of f_S and r.

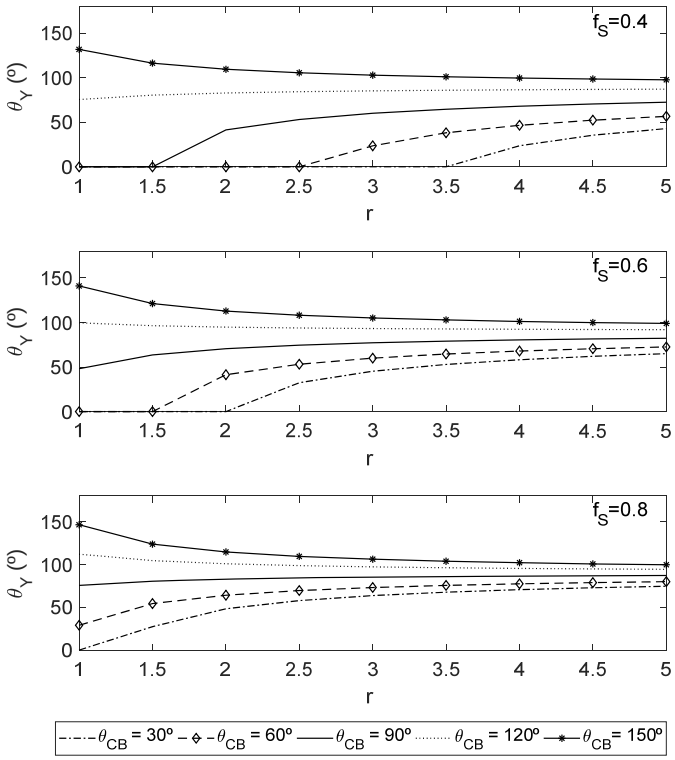

Figure 3.7 Representation of the intrinsic contact angle θ_Y corresponding to a set of given Cassie Baxter's apparent contact angles as a function of the roughness factor r for of θ_{CB}= 30°, 60°, 90°, 120° and 150° and f_S = 0.4, 0.6 and 0.8.

According to all of the above, for samples with complex microstructure best described by the Cassie Baxter model, if we do not take into account the specific geometry of the surface when performing an evaluation of the surface energy, we will underestimate grossly its value.

In terms of the surface energy, we can notice the exposed behaviours taking into account if the surface is hydrophilic or hydrophobic as we performed with Wenzel model.

For the before considered hydrophilic surface (Figure 3.8), for low values of both f_S and r, the value of the intrinsic surface energy (γ_S) is larger than the value of the surface energy measured with both liquids when not correcting for roughness. This fact is due to the trapped air under the drop that makes the surface to behave less hydrophilically. As f_S becomes larger, the trapped air under the drop decreases and the surface behaves more similar to Wenzel's model, since there is a bigger fraction of material which is in contact with the drop. Furthermore, if r becomes also larger, the surface becomes more hydrophilic since at a certain point, the value of the measured surface energy is larger than the surface energy for the smooth surface as a result of the increased roughness.

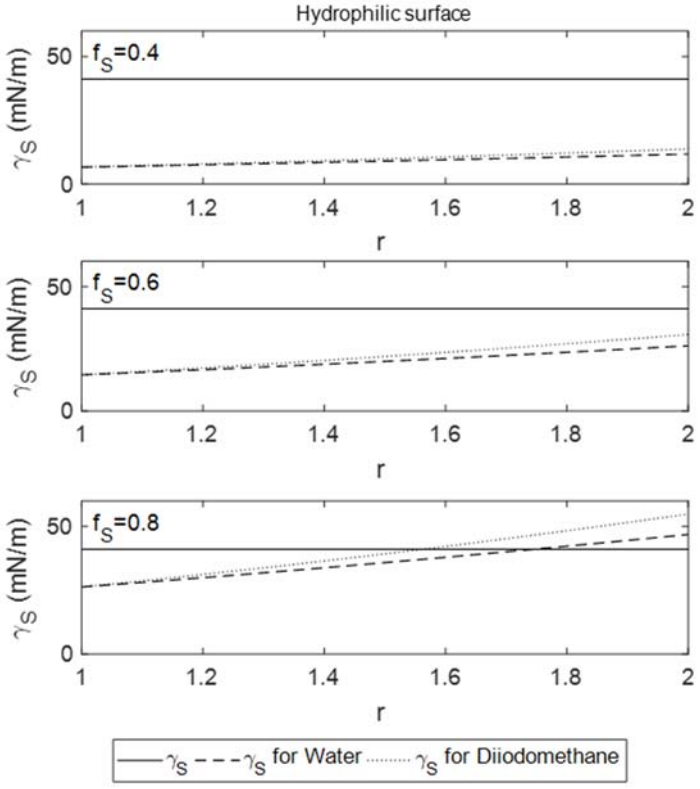

Figure 3.8 Evaluation of the surface energy for a hydrophilic surface, where the roughness varies from 1 to 2 for $f_S = 0.4$, 0.6 and 0.8 comparing to the intrinsic surface energy value.

Conversely, if the surface is hydrophobic, its behaviour is slightly different as can be seen in Figure 3.9. In this case, the value of the intrinsic surface energy is larger than the one estimated when not correcting for the roughness and the fraction of material in contact with the drop. Even then, as f_S and r become larger, the surface becomes less hydrophobic. Furthermore, for small values of r, the error made in the evaluation of the SE not considering the real contact area between the liquid and the solid decreases as f_S increases.

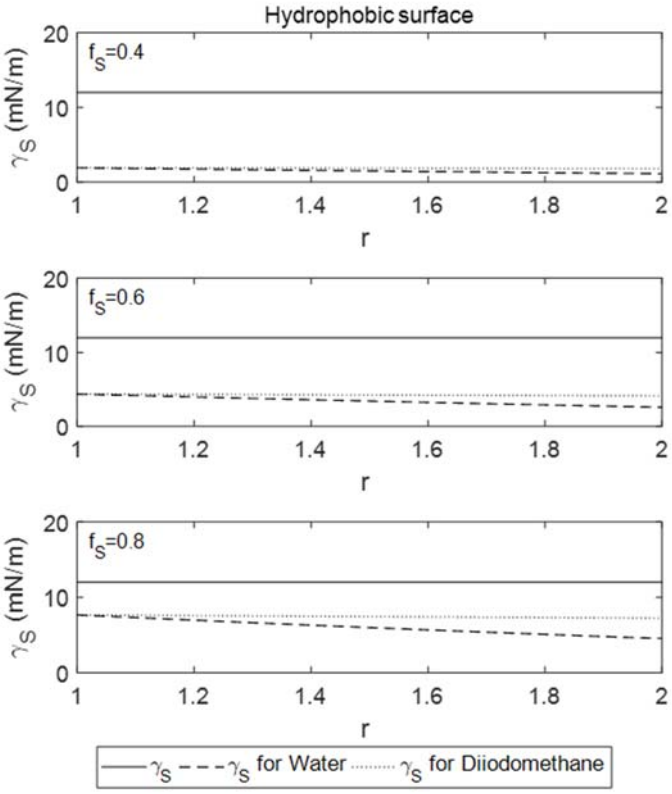

Figure 3.9 Evaluation of the surface energy for a hydrophobic surface, where the roughness varies from 1 to 2 for $f_S = 0.4$, 0.6 and 0.8 comparing to the intrinsic surface energy value.

The question arises whether one can distinguish easily between Wenzel and Cassie-Baxter scenario and the answer is yes. When placing a drop of liquid on a solid surface and it easily slides, we are in Cassie Baxter's regime. On the other hand, if the droplet remains stuck on the surface even though it is a hydrophobic surface, we are in Wenzel regime.

There is a particularly striking example in nature were both models can be observed. For example, a Wenzel scenario can be observed in a rose which petals are hydrophobic but the water drops reaching the surface do not slip off and remain on the petal, as shown in Figure 3.10(a). Due to the micro structure of the surface and the wetting conditions, the liquid drop sticks to the surface and does not slip.

(a) (b)

Figure 3.10 (a) Image of a flower petal with a water drop stuck on its surface that represents a Wenzel scenario; (b) image of sliding water on a lotus leaf that represents a Cassie-Baxter's scenario. Sources: [87], [88]

On the other hand, a Cassie-Baxter's scenario is easily recognized on a lotus leaf as Figure 3.10(b) shows. These kind of leafs are of particular interest in superhydrophobic studies and self-cleaning surfaces development due to its microstructure and its capability to drag the dirt particles as the water slips off on the surface.

3.4. Summary

This chapter has presented the effect of the roughness of a surface in the evaluation of its surface energy as well as how the modification of the structure of the surface can enhance the wettability properties of the solid.

Two different models have been presented to correct the effect of the roughness on the contact angle calculations. On the one hand, Wenzel model pointed out that the introduction of roughness on a surface improves its wetting properties. The introduction of roughness makes a hydrophilic surface even more hydrophilic and a hydrophobic surface even more hydrophobic.

On the other hand, Cassie-Baxter's model highlighted that this introduction of roughness on a hydrophobic sample can enhance its hydrophobicity to become superhydrophobic, but never hydrophilic. On the contrary, in a hydrophilic surface, depending on the values of r and f_S, the surface can cross over from hydrophilic to hydrophobic or else become more hydrophilic.

The effect of the roughness of the solid on the surface energy has also been evaluated giving as a result that the error introduced by not taking into account this roughness is greater the greater the value of r. This result gives strength to this Ph.D. thesis that is focused on evaluating the surface energy on rough samples by correcting the effect of the roughness, which has been demonstrated to be an important cause of error.

The next step in this Ph.D. Thesis consists in introducing how we are going to carry out the evaluation of the surface energy by first presenting the mathematical method developed and the minimum error that it introduces to the calculations of the contact angle.

4. Proposed mathematical method for measuring the contact angle

4.1. Introduction

As seen in Chapter 3, current techniques can only be applied to assess the global hydrophobicity or hydrophilicity of the surface, but cannot be used to determine the intrinsic surface energy if the surface under study is not smooth. As has been demonstrated with Wenzel model, the greater the roughness of the surface, the more erroneous it is to associate the measured apparent contact angle only with the evaluation of the surface energy. On the other hand, as Cassie Baxter shows, the greater the roughness, the greater the contact area between the liquid and the solid, and the greater the effect of the trapped air bubbles, so these factors can only be suitably accounted for when the local microstructure of the surface under study is known.

From these presented models in Chapter 3, it can be verified that there is a direct correlation between the topography of a surface and the contact angle of a drop placed on it. For this reason, the surface energy of a rough material should not be calculated directly from the measured contact angle [89] and it is necessary to obtain the intrinsic contact angle thanks to the Wenzel or Cassie Baxter models [83], [86].

In order to be able to use these calculation methods correctly in real samples (as opposed to samples specifically prepared with a determined topography via etching or other such processes), one must know with the utmost accuracy both the contact angle and the topography of the sample in the exact area of the sample where the drop has been placed.

Unfortunately, no commercial device is currently available to perform both topography and contact angle measurements. The use of two different devices leads to a sample positioning uncertainty, implying that besides the time and resource consumption inherent to making two different measurements with two different devices, no assurance can be given that both measurements are performed on the same area on the sample and that the resulting calculated surface energy is correct.

In order to solve this problem, a measurement method has been developed in this Ph.D. Thesis to measure the contact angle with a commercial device designed for non-contact topography measurements. This technique allows the measurement of both the topography of a solid surface and the contact angle of a drop placed on it, with a single device based on confocal technology. Thus, shifting in the sample positioning between the two

measurements is avoided and the proper location of both measurements in the same area of the sample is ensured.

The developed measurement method has two main parts: the mathematical models, to calculate the contact angles, and the measurement strategy, to perform the measurements of the required parameters by means the confocal device, for the calculation of the contact angles.

The confocal device will provide the measurement of several parameters of a liquid drop placed on the surface under measurement, as its height (h) and its apparent diameter (L), by means of the measurement strategy that will be introduced in next chapter. These parameters, in combination with the volume of the drop (V), that will be known for each drop thanks to the use of a high accuracy liquid dispenser, will allow to calculate the apparent contact angle of the drop by three different mathematical models presented here below.

This chapter will also include an evaluation of the error introduced in the calculation of the contact angles by means the three different mathematical method to verify their validity to perform contact angle calculations.

4.2. Developed mathematical models to calculate the contact angle

The three different mathematical models to calculate contact angles arise from the combination of the measured parameters of the drop by the confocal device, i.e. h and L, together with the volume of the dispensed drop, V. We have proposed to calculate the contact angle by taking into account only the following pairs of parameters: (h, L), (V, L) and (h, V).

As Figure 4.1 shows, two possible situations when placing a liquid drop on a surface can be found, depending on the wetting properties of the surface that will be considered in the developed mathematical models, assuming that the drop is perfectly spherical.

Figure 4.1(a) shows a drop placed on a high wettability surface, which means that the liquid drop maximizes its contact area with the solid surface and the contact angle is smaller than 90°. In the second scenario, as Figure 4.1 (b) shows, the drop minimizes the contact area with the surface, which means the surface has low wettability and it is therefore hydrophobic. In this case, the contact angles will be always greater than 90°.

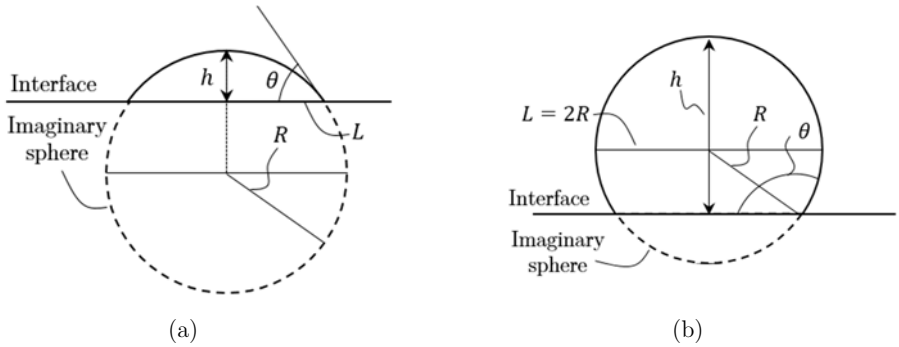

(a) (b)

Figure 4.1 Schematic representation of a drop placed on a (a) high wettability surface; (b) low wettability surface assuming that it is perfectly spherical.

Next, the mathematical expressions developed for each pair of parameters will be presented to calculate the contact angle exclusively with the corresponding parameters, but further details on the mathematical development can be found in Appendix B. Although the mathematical models described below could seem very easy and straightforward compared to the available fitting methods in a commercial contact angle meter, we will demonstrate that taking into account the roughness of the surface compensates the small error introduced by the developed measurement method to calculate the contact angle.

4.2.1. Contact angle calculation with h and L

The first mathematical model presented is based on a purely geometric calculation of the contact angle by means of the height h and the apparent diameter L of the drop, both measured with the confocal device. The mathematical expressions to calculate the contact angle of the drop in the hydrophilic and the hydrophobic surfaces are stated in equations (2.7) and (4.2) respectively.

$$\theta = acos\left(\frac{\frac{L^2}{4} - h^2}{h^2 + \frac{L^2}{4}}\right) \tag{4.1}$$

$$\theta = acos\left(\frac{L - 2h}{L}\right) \tag{4.2}$$

4.2.2. Contact angle calculation with h and V

The second mathematical model presented is based on the calculation of the contact angle by means of the height of the drop h and its volume V as stated in equation (4.3), regardless of the wetting properties of the surface.

$$\theta = acos\left(\frac{3V - 2\pi h^3}{3V + \pi h^3}\right) \tag{4.3}$$

4.2.3. Contact angle calculation with L and V

The third mathematical model relates the contact angle θ together with the apparent diameter of the drop L measured by the confocal device and the volume of the drop V and their expressions were developed by Mazzola et al. in [89].

The mathematical expressions to calculate the contact angle of the drop on the hydrophilic and the hydrophobic surfaces are stated in equations (4.4) and (4.5) respectively.

$$L = \frac{2\sqrt[3]{V}\,sin\,\theta}{\sqrt[3]{\frac{\pi}{3}\,[2 - 3\,cos\,\theta + cos^3\,\theta]}} \tag{4.4}$$

$$L = \frac{2\sqrt[3]{V}}{\sqrt[3]{\frac{\pi}{3}\,[2 - 3\,cos\,\theta + cos^3\,\theta]}} \tag{4.5}$$

The main difference presented by this mathematical model is that the contact angle does not have a direct mathematical expression as a function of the selected parameters. Since the analytical solution is a complex and lengthy process, the value of the contact angle would be obtained by numerical analysis in each scenario.

As commented previously, one can think at first glance that these mathematical developments are very easy ways to calculate the contact angle with less accuracy than that provided by a fitting method. Even so, as we will see later in this Ph.D. Thesis, the potential of these simple analytical equations combined with a high accuracy device in the field of metrology will be proved. The reliability and accuracy of the performed measurements with the confocal device and the application of these easy expressions will result in a powerful, easy-to-use method, well suited for the measurement of hydrophobic samples, which arises as a solution to the previous exposed problems in this Ph.D. Thesis. We now proceed to evaluate the error that the measurement of those parameters could introduce in the calculation of the contact angle with each of these mathematical models.

4.3. Evaluation of the error introduced in the calculation of the contact angle

The previous presented mathematical expressions have two main sources of errors that could affect the calculations of the contact angle. On the one hand, measuring the height and the apparent diameter of the drop by means of the confocal device, introduces a positioning error depending on the axis of measurement. On the other hand, when the volume of the drop is involved in the calculations, the error will be determined by the accuracy of the used liquid dispenser. In our case of study, using a 10X microscope objective, and in the case where at least half of the drop is visible within the FOV, the values of these errors are tabulated in Table 4.1.

Table 4.1 Values of the errors introduced by the measurement of h (δh) and L (δL) by means the confocal device and the error introduced in the volume (δV) of the drop by means of the liquid dispenser.

Errors		
δh (μm)	δL (μm)	δV
1	10	1% of the nominal volume

We therefore proceed to evaluate the minimum error introduced by the measurement of these parameters assuming the drop to be perfectly spherical in the calculation of the contact angle by the mathematical models developed in this Ph.D. Thesis.

For each mathematical method this section presents the final expressions that evaluate the error introduced in the contact angle ($\delta\theta$) by the different parameters taking into account the sources of error. The mathematical expressions are obtained by standard error propagation procedures and assuming independent sources of errors, so the final contribution results from the square root of the sum of both squared contributions.

4.3.1. Evaluation of the error introduced in the calculation of θ by the measurement of h and L

The errors introduced in the first mathematical model come exclusively from the measurement of h and L by the confocal device and are therefore related to the measurement error of the device, assuming the volume constant.

The mathematical expressions that take into account the error introduced by h and L in a hydrophilic and in a hydrophobic sample when calculating the contact angle are stated by equations (4.6) and (4.7) respectively.

$$\delta\theta = \frac{4}{L^2 + 4h^2}\sqrt{(L \cdot \delta h)^2 + (h \cdot \delta L)^2} \tag{4.6}$$

$$\delta\theta = \frac{1}{\sqrt{h(L-h)}} \cdot \sqrt{\delta h^2 + \left(\frac{h}{L} \cdot \delta L\right)^2} \tag{4.7}$$

where δh and δL are the errors introduced by the measurement of h and L respectively by the confocal device.

Figure 4.2 plots the values of the minimum error in the calculation of the contact angle in both the hydrophilic and hydrophobic regime due to the error introduced by the measurement of h and L by means of the confocal device for given values of the volume of 2, 5 and 10μL, as long as the spherical approximation holds.

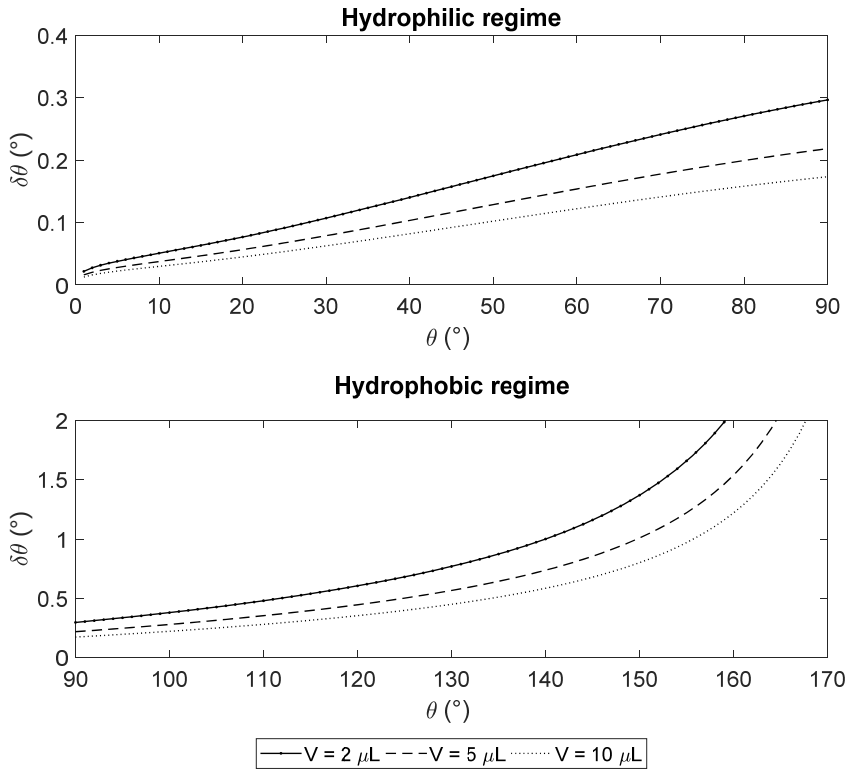

Figure 4.2 Evaluation of the error introduced in the calculation of the contact angle, in both the hydrophilic and hydrophobic regime, by the parameters h and L, measured by the confocal device, for 2, 5 and 10μL as exemplary values of V.

Although the error increases as the contact angle does and as the volume becomes smaller the error increases, we can assume that the contact angle calculations will not be overly affected by these errors neither in the hydrophilic nor in the hydrophobic regime.

This method will be the one used in Chapter 6 to calculate the contact angle by the measurement of h and L, exclusively by means of the confocal device. Calculating the contact angle with this method enables us to do a direct comparison with the values of the contact angles measured by height-width fitting methods available in the contact angle meter due to their similarity.

4.3.2. Evaluation of the error introduced in the calculation of θ by the measurement of h and V

The errors introduced in the calculation of the contact angle by means of the second mathematical model come from the measurement of h by the confocal device and the error in the volume of the drop introduced by the liquid dispenser, assuming L constant.

The mathematical expression that gives the error introduced by h and V in both hydrophilic and a hydrophobic samples when calculating the contact angle is stated by equation (4.8).

$$\delta\theta = \frac{\sqrt{3\pi}\sqrt{h^3(6V-\pi h^3)}}{3V+\pi h^3}\sqrt{\left(\frac{3}{\pi h^3-6V}\cdot\delta V\right)^2+\left(\frac{9V}{6Vh-\pi h^4}\cdot\delta h\right)^2} \tag{4.8}$$

where δV is the error introduced by the liquid dispenser in the volume of the measured drop.

Evaluating the introduced error in the contact angle calculation for the second mathematical model as we performed in the previous model, as Figure 4.3 shows, we can also validate this second method for the calculation of the contact angle using h, measured by the confocal device and knowing V by using the accurate liquid dispenser.

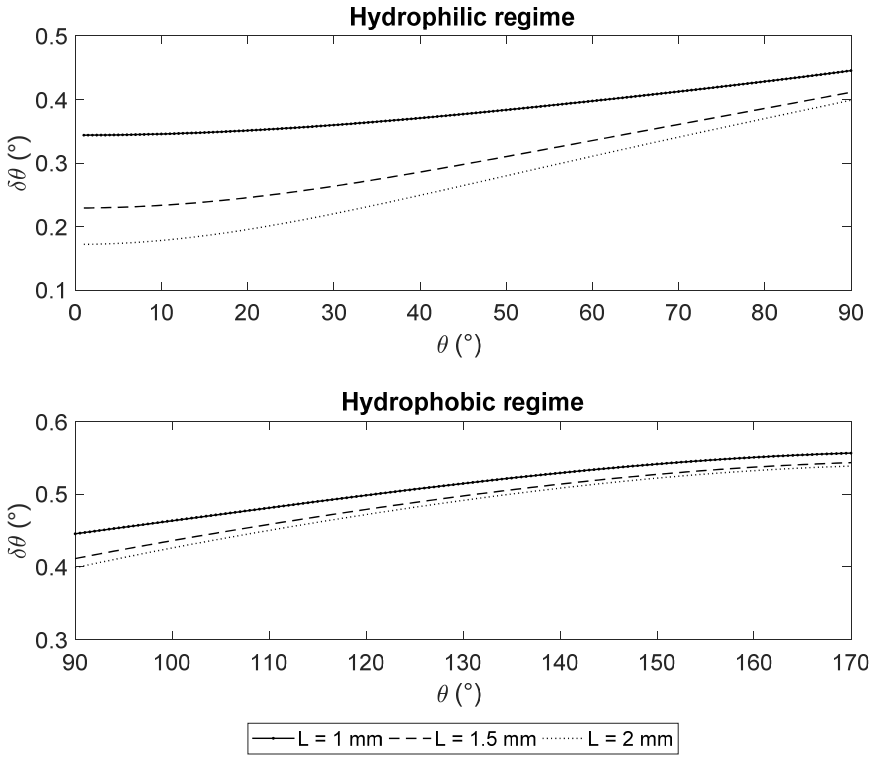

Figure 4.3 Evaluation of the error introduced in the calculation of the contact angle, in both the hydrophilic and hydrophobic regime, by the parameters h and V, for 1, 1.5 and 2mm as exemplary values of L.

The error introduced by calculating the contact angle using the parameters h and L is similar to the introduced by the previous method, therefore, theoretically, both methods are equally valid.

4.3.3. Evaluation of the error introduced in the calculation of θ by the measurement of L and V

In the last of the three mathematical models the errors in the contact angle calculation is introduced in the measurement of L by the confocal device and the error in V introduced by the liquid dispenser, assuming h constant.

The main difference of the actual mathematical model is that the evaluation of the error introduced in the contact angle calculation must be performed numerically, so there is no mathematical expression.

Figure 4.4 shows the numerical evaluation of the error performed for the calculation of the contact angle with L and V in a hydrophilic and a hydrophobic sample for 0.3, 0.5 and 1 mm as exemplary constant values of h.

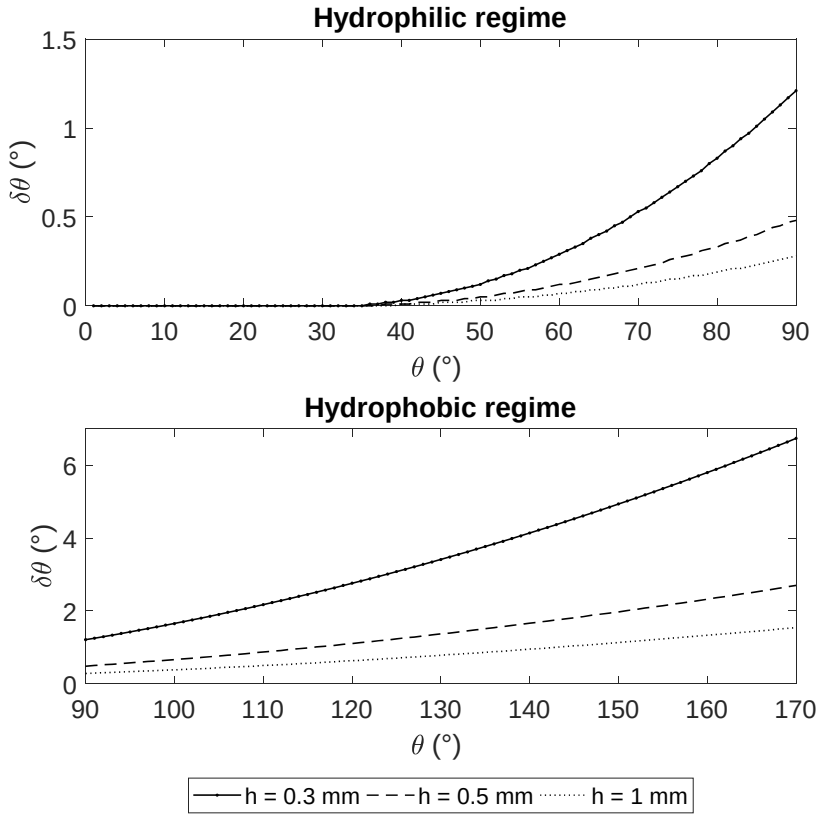

Figure 4.4 Evaluation of the error introduced in the calculation of the contact angle, in both the hydrophilic and hydrophobic regime, by the parameters L and V, for 1, 0.5 and 0.3 mm as exemplary values of h.

This last method introduces a much larger error values than the previous methods. The numerical evaluation could have an impact in the estimation of these larger error but, overall, we think it is just less accurate than the other two.

4.4. Summary

We have been able to develop three different mathematical models to calculate the contact angle based on these sets of easily measured parameters (h, L), (V, L) and (h, V), two of which can be measured with the confocal microscope, while the second is given by the liquid dispenser accuracy. We have estimated by error propagation the error introduced in the calculation of the contact angle for all three mathematical models due to the measurement errors in the measured parameters. The results indicated that the first two models are better suited to estimate the contact angle because the propagated error is smaller. Even so, from now on we will focus on the first mathematical model, which uses h and L , both of which can be obtained exclusively by means of the confocal device, since from the point of view of further experimental implementation, we will have more confidence in performing the contact angle calculations in a straight and feasible way.

Next chapter will present the second part of the developed measurement method consisting in the measurement strategies. We therefore proceed to explain the measurement strategies to perform the contact angle measurements by means of a commercial contact angle meter and the confocal device.

5. Measurement strategies

5.1. Introduction

After the introduction of the developed mathematical models to calculate the contact angle from different sets of parameters of the drop, it is time to introduce the second part of the developed measurement method, which are the measurement strategies.

As discussed earlier, the structure of a surface is of key importance for its wetting properties. For this reason, in this Ph.D. we want to evaluate the surface energy of hydrophobic samples taking into account its surface structure, specifically its roughness. To be able to perform this evaluation as accurately as possible, we need to use a device whose capabilities in topography measurements are at the top of the sector, i.e. the confocal device.

On the other hand, in order to give reliability to those results obtained by the confocal device, the contact angle values as well as the calculated surface energy need to be compared with reliable values obtained by another accurate device in the field of the contact angle measurements. In this case, we selected a commercial contact angle meter that measures the contact angle and calculates the corresponding surface energy in a reliable and accurate way in the case of smooth samples.

This section contains two main parts, corresponding the two different devices that were used in this study. First we will present the commercial contact angle meter that was used to measure the contact angle on hydrophobic samples from the side and the developed measurement strategy to perform the contact angle measurements. Then, we will present the confocal device used to measure the set of parameters of the drop that are used to calculate the contact angle with the first mathematical model presented in Chapter 4, and the measurement strategy developed to measure the required parameters.

To finish with the measurement strategies, we will introduce how the surface energy is calculated by the commercial contact angle meter. This same strategy will also be applied with the contact angle values obtained with the confocal device.

5.2. Contact angle meter

Since the aim of this study is to validate a developed measurement method in hydrophobic samples, accuracy and precise contact angle values are needed to compare them with the ones we want to validate. In this section we are going to present the results obtained from the contact angle and surface energy measurements performed thanks to the stay in a The Welding Institute (TWI) in Cambridge, equipped with an accurate and really

reliable contact angle meter, with extensive functionality for the calculation of the surface energy of the solid surface under measurement.

TWI has expertise in the areas of joining and coating technology for engineering materials and it is at the forefront of the development of novel coatings of many types and their characterization.

The contact angle meter with which the TWI is equipped has been manufactured by KRUSS, which produces first-class measuring instruments for surface and interfacial chemistry. The DSA-100, see Figure 5.1(a), is specialized in coatings characterization and its technology allows the user to measure the contact angle of a liquid drop and the evaluation of the surface energy of the solid surface under measurement.

A software that allows the user a wide range of measurement options for the contact angle and the proper evaluation of the surface energy controls the device. This study focuses on the contact angles obtained from a sessile drop and the corresponding evaluation of the surface energy of the solid surfaces.

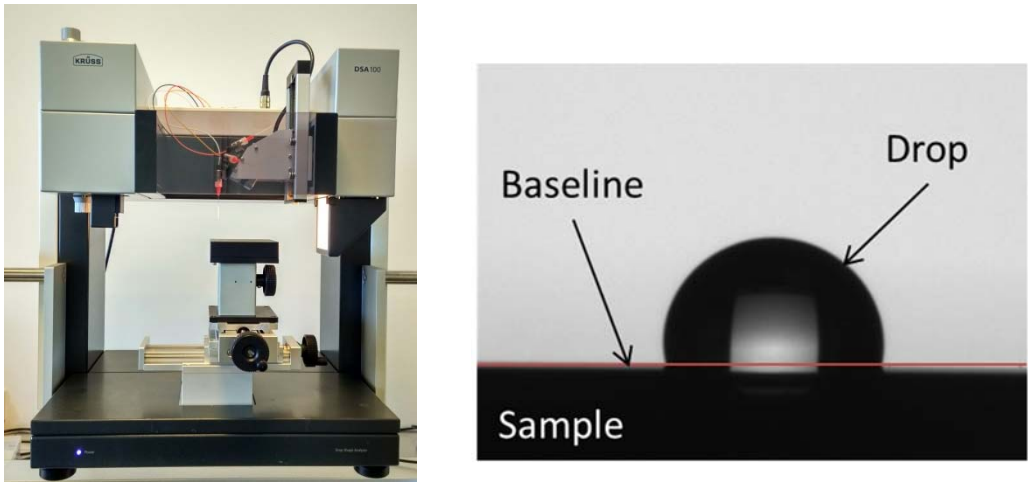

(a) (b)

Figure 5.1 (a) Picture of the DSA-100 from KRUSS used to perform the contact angle measurements; (b) Image of a sessile drop acquired by the DSA-100.

The methodology of the DSA-100 for the measurement of the contact angle is based on the shape analysis of the lateral view of the drop for every measurement method as shown in Figure 5.1(b). It includes the sessile drop, pendant drop and the dynamic contact angle methods among others. It is equipped with a high-resolution camera and three-axis mechanical stage used as a sample holder. The liquid dispenser consists of a set of syringes located on a revolving holder allowing the measurement of the contact angle with up to 8 liquids, which is translated in maximum accuracy for determining the surface free energy. Each syringe links to a liquid reservoir containing the liquids of interest and the software controls the dispensation of each drop. It also allows the user to control the volume of the dispensed drop and the liquid used in each measurement. All of these qualities make the DSA-100 a reliable and high accuracy contact angle meter.

In order to compare the measurements obtained with this device with those obtained with our measurement method, the use of a sessile drop is mandatory since, with our method, the drop will be measured in a top view configuration. For this reason, the principal measurement method chosen to measure the contact angle with the DSA-100 was the sessile drop.

The sessile drop measurement method performed by the DSA-100 has a wide range of options to perform the fitting to the sessile drop in order to obtain the contact angle. The circle, ellipse, height/width, tangent and Young-Laplace are the methods available in the software and are shown in Figure 5.2.

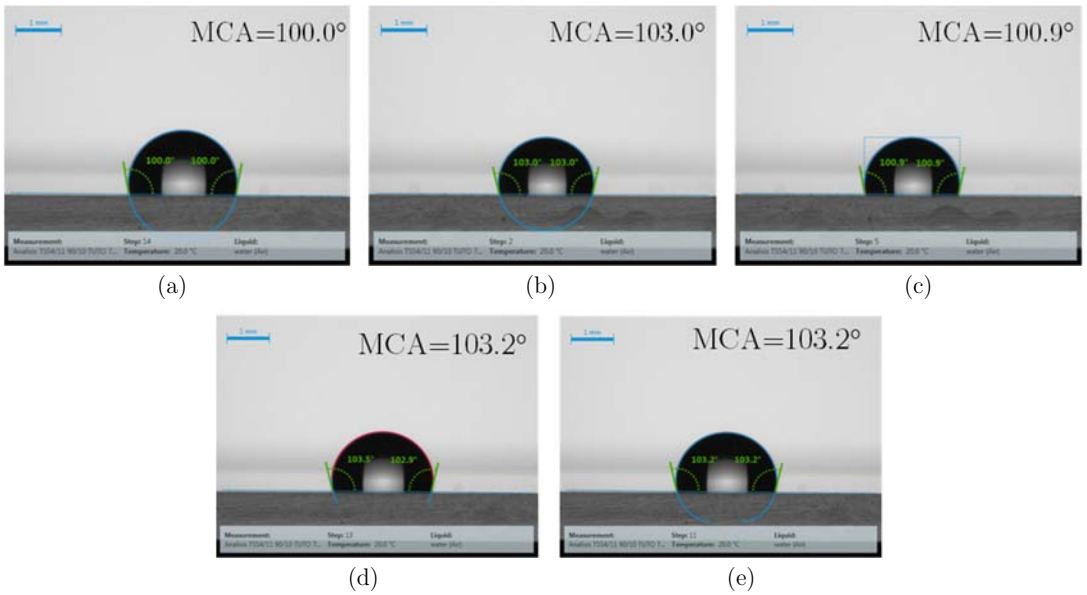

Figure 5.2 Images of the same water drop placed on a hydrophobic solid surface, showing the different applied fitting models of the contact angle by the DSA-100 software and the mean values (MCA) obtained. (a) Circle, MCA=100.0°; (b) Ellipse, MCA=103.0°; (c) Height/width, MCA=100.9°; (d) Tangent, MCA=103.2° and (e) Young-Laplace, MCA=103.2°, fitting methods. The figures include the simulation lines of the shape of the water droplets and the horizontal baselines.

From the pictures, it is easy to see that the extracted values of the contact angle depend strongly upon the fitting method applied. The reason why they are different relies on the fitting equation and the number of points that each method uses. This does not mean that one fitting method is better than the others but rather that each is more appropriate in particular measurement conditions, regarding the wettability of the surface and the measurement liquid.

In order to obtain valuable and reliable data in our study, the sample was measured several times with different liquid drops, as Figure 5.3(a) shows. The edge of the sample must be placed as close as possible to the edge of the sample holder and the drops must be placed near to the edge of the sample. In this way, the user can avoid misinterpretations and inaccuracies due to the loss of the sharpness in the contact area between the drop and the sample when the drop is placed far from the edge, as Figure 5.3(b) shows.

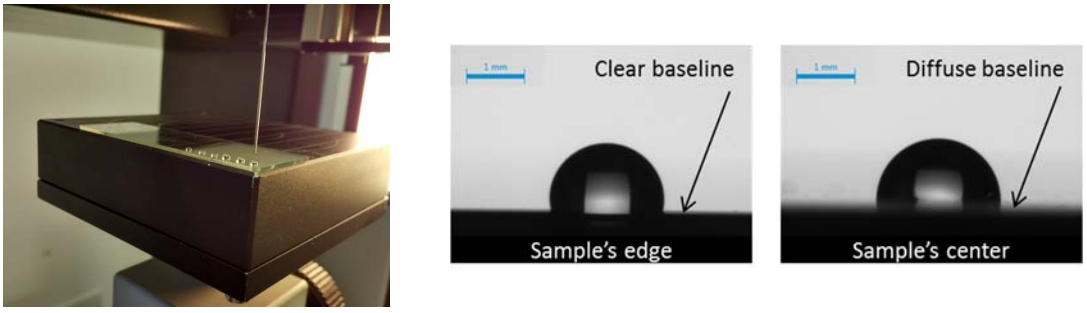

(a) (b)

Figure 5.3 (a) Placement of the sample in the sample holder of the DSA and location of the water drops, (b) Comparison of the sharpness of the interface when a drop is placed on the edge and far from the edge of a hydrophobic sample.

In order to place correctly the drop on the surface of the sample it is mandatory to let it fall from the smallest possible height so kinetic energy does not spread it. To do that, the tip of the syringe should be as close as possible to the sample so that, when the drop is growing, it will touch the surface and the adhesion to the surface will pull it off the tip when it recedes.

Different measurement strategies were carried out in order to achieve a database as complete as possible. With all the available samples, all the different fitting methods were applied to measure the value of the contact angle with at least three liquid drops in each sample, for each liquid, and measured its contact angle. All the different available fittings were applied to each drop to verify their functionality for each case. Since our developed method has as parameters the height and the width of the drop, the contact angle values obtained with the DSA from the height/width fitting method will be compared with the ones obtained by the presented method as they use the same set of parameters.

Another key point of the method used by the DSA-100 is the way in which it evaluates the surface energy once the contact angle is measured. In order to measure the surface energy as reliably as possible, two different liquids are used, one dispersive and the other

one polar. In this way, the DSA-100 used the OWRK method, introduced in Chapter 2, which takes into account these two components when calculating the surface energy.

As a first step, the DSA-100 software calculates the dispersive part of the surface energy since the Diiodomethane only has the dispersive component. Therefore, the dispersive part of the surface energy (γ_S^d) of the solid surface is directly calculated as stated by equation (2.4) in Chapter 2, and expressed by equation (5.1).

$$\gamma_S^d = \frac{\gamma_L}{4}(1 + cos\,\theta_D) \tag{5.1}$$

Where γ_L is the dispersive part of the Diiodomethane surface energy and θ_D is the contact angle measured with the Diiodomethane.

Once the dispersive part is calculated, the polar part can be calculated using water as the measurement liquid. Equation (5.2) shows how the different components of the surface energy of the water and the measured water contact angle can be used to calculate the polar component of the solid surface energy.

$$\gamma_S^p = \frac{1}{\gamma_L^p}\left(\frac{\gamma_L^T}{2}(1 + cos\,\theta_P) - \sqrt{\gamma_S^d \gamma_L^d}\right)^2 \tag{5.2}$$

Where γ_L^p is the polar part of the surface energy of the water, γ_L^d is the dispersive part of the surface energy of the water, γ_L^T is the total surface energy of the water and θ_P is the polar contact angle measured with water.

Finally, the total surface energy of the solid is the sum of both components.

5.3. Confocal device

First, it is important to highlight the reason why the chosen device is a confocal microscope. As has been mentioned in previous chapters, there is a proven relationship between the roughness of a surface and its contact angle but, nowadays, no device is available that can perform both measurements. There are devices specialized in contact angle and surface energy measurements, as the one presented above and devices specialized in topography measurement as the one selected in this study.

The device used is the S-Neox, shown in Figure 5.4(a), from Sensofar Metrology Company who develops, manufactures and commercializes high-end 3D surface metrology tools. The S-Neox is a very accurate and reliable non-contact 3D surface profiler that combines confocal, interferometry and focus variation techniques.

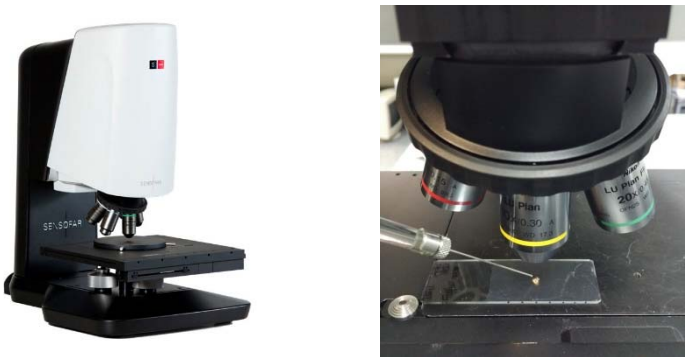

(a) (b)

Figure 5.4 (a) Picture of the S-Neox from Sensofar, (b) close-up of the sample placed on the sample holder of the S-Neox and the high accuracy syringe placing the measuring water drop on the sample.

The device is equipped with a set of microscopic objectives with magnifications from 2.5X to 150X and numerical apertures up to 0.95, located in a manually controlled revolver objective holder. The three-axis mechanical stage used as a sample holder is controlled by software and its resolution is up to 2 nm with linear stage and 0.75 nm with piezo stage. All of this gives the confocal device great capability and high accuracy performing topographic measurements.

As has been mentioned, the device offers three different measurement methods and each one has the proper set of microscope objectives to get the right performance depending on the characteristics of the sample under measurement. Due to the requirements of the presented study, the measurement method which fits better is the confocal method.

There are different reasons to justify this choice but one of the most important is the high vertical resolution that this technique provides. As has been explained in Chapter 4, the developed calculation methods have as main parameters the height (h) and the width (L) of the liquid drop to be measured. Since the vertical resolution of the confocal technique is down to 1 nm, this means that the height of the drop can be obtained with high accuracy in the nanometer range, thus significantly reducing the error in the calculation.

One of the main advantages that the S-Neox presents over the traditional side-view devices is that there is no constraint on the placement of the sample to measure the contact angle since it performs a top view measurement. There is therefore no inconvenient from reflections produced by the edges of the sample.

The first step in the developed measurement method consists on measuring the topography of the sample at the exact location where the drop will be later placed. We use a 20X microscope objective to perform the measurement with high accuracy, according to the characteristics of the samples to be measured.

As the field of view of the 20X microscope objective is about 660 µm x 480 µm, the topography of the sample is obtained by performing a 6x6 extended topography, in order to cover the entire surface where the drop will be later placed, as shown in Figure 5.5(a).

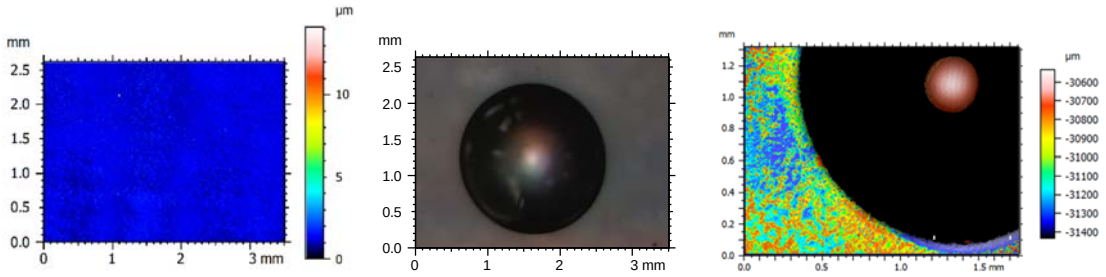

(a) (b) (c)

Figure 5.5 (a) Extended surface topography of one of the measured samples with a 20X microscope objective, (b) top-view image of the liquid drop deposited on the sample, obtained with a 5X microscope objective and (c) dual topography of both the apex of the drop and the surface of the sample performed with a 10X microscope objective.

The second step after the measurement of the topography, consists on placing the liquid drop within the limits of the measured area by changing first the microscope objective by a 5X in order to see the entire drop in the field of view. An image of the drop is taken from above, as Figure 5.5(b) shows, from which the width of the drop will be later obtained by software processing.

This time, the drop dispensation is performed manually with a high accuracy syringe with which the volume is always under control. Placing manually the drop has its advantages so the user can locate exactly the drop under the light path of the device ensuring the right positioning of the drop on the measured area of the sample.

Immediately after taking the image, a dual topography is performed in order to measure the height of the drop. As we need to enlarge the field of view to be able to see simultaneously the apex of the drop and the surface of the sample, we change to a 10X microscope objective. First, the apex of the drop must be located and fitted within the field of view of the microscope objective. Then we search approximately the distance from the apex to the sample surface. We can then perform two topography scans, one on the apex of the drop and the other on the sample surface, both with the appropriate scanning ranges. The measurement of the height of the drop by this procedure reduces the measuring time while the drop and avoids the evaporation of the liquid drop.

Figure 5.5(c) shows the dual topography where the topography of both the apex and the surface of the sample are measured. The color scale shows the difference in height between the sample surface and the apex of the drop. From this dual topography we will obtain the height of the drop by the processing software, which is the last parameter needed to calculate the contact angle with the developed measurement method.

The next step consists in measuring the roughness of the surface, the height and the width of the drop processing the three previous measurements with the software. The roughness of the surface is obtained from the topography of the surface of the sample, the width of the drop from the top-view image of the drop and the height of the drop from the dual topography.

The first step of this processing procedure consists in obtaining L (width of the drop). With the software named Sensomap, from Sensofar Company, the contour of the drop can be extracted from the image and a circle fitting can be performed to obtain the value of L as shown in Figure 5.6(a).

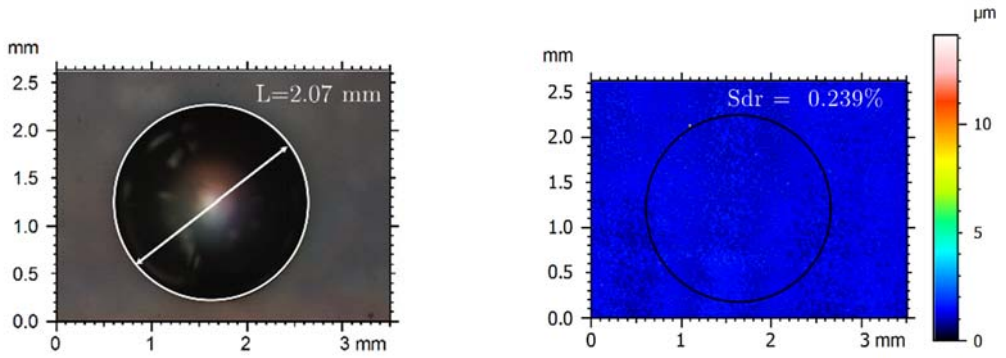

(a) (b)

Figure 5.6 (a) Measurement of L of the drop by fitting a circle to the contour of the liquid drop in the image taken by the S-Neox. (b) Calculation of the *Sdr* parameter in the area filled by the liquid drop.

The next step consists in measuring the roughness of the surface from the previous performed topography. By processing this data set with the Sensomap software, we can obtain the Developed Interfacial Area Ratio (Sdr) [90] which is defined as the additional surface area contributed by the texture as compared to a flat plane on the same measurement region size and is expressed in percentage.

The value of the Sdr is obtained processing the entire area where the topography was performed, and therefore where the drop was deposited, as shown in Figure 5.6(b).

With this parameter, we can calculate the roughness ratio factor r by applying equation (5.3). This parameter is the one needed to correct the effect of the roughness in the contact angle calculation according to Wenzel's model.

$$r = 1 + \frac{Sdr}{100} \tag{5.3}$$

The last step consists on measuring the height of the drop of liquid placed on the surface of the sample from the dual topography. With Sensomap, we can obtain the profile of this topography by tracing a line which connects the two topographies, from surface to apex, to finally measure the value of the height of the drop, as shown in Figure 5.7(a) and Figure 5.7(b).

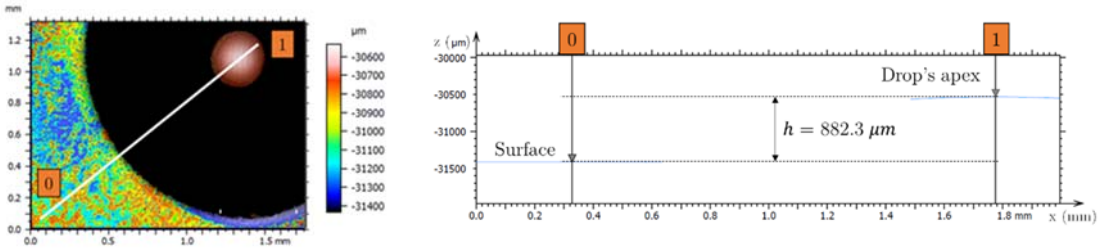

(a) (b)

Figure 5.7 (a) 2D view of the dual topography of both the apex of the drop and the surface of the sample to measure the height of the drop from the profile obtained from the drawn line, (b) measured height of the drop.

At this point, with L and h measured, the contact angle of the sample can be calculated by method presented in Chapter 4, in which h and L are the only required parameters. As was said before, we selected this calculation method because one of the aims of this Ph.D. Thesis consists in demonstrating that a confocal device can provide singlehandedly all the required parameters needed for the calculation of the contact angle. Hence, the selected mathematical model calculates the contact angle by parameters only measured with the S-Neox, and is therefore not influenced by other error sources such as the error in the volume due to the liquid dispenser.

Furthermore, with the roughness ratio factor obtained from the topography of the surface, we can correct the contact angle according to Wenzel's model, introduced in Chapter 3. Thus, we take into account the real roughness of the surface under study with the certainty that the topography and the contact angle measurements were performed in the same exact area of the sample.

As commented before, this procedure is performed several times for the same samples measured with the DSA-100 as well as with water and Diiodomethane as measurement liquids. The measurement of the contact angle is performed for three different drops of each liquid in order to obtain a mean contact angle value as reliable as possible and which turns out to be comparable with the ones obtained with the measurements performed with the DSA-100.

The use of these two liquids allows the evaluation of the surface energy of each sample with the mathematical expressions introduced before, taking into account the contributions of the dispersive and the polar parts in the surface energy.

With these measurements, our aim is to demonstrate the validity and accuracy of the presented measurement method for measuring contact angles in hydrophobic samples with a confocal device. Furthermore, we are able to correct those contact angles values with the influence of the surface roughness according to Wenzel's model, verifying the validity of the developed method to finally calculate the intrinsic surface energy of the surface under study.

6. Experimental measures

6.1. Introduction

In this chapter, we will present the experimental results obtained with the measurements performed with both the DSA-100 and the S-Neox. First, we will introduce the different samples used in this work, as well as their main characteristics and the kind of measurements performed with each one. We will then present the contact angle values obtained for each sample and its corresponding value of the surface energy provided by the DSA-100. Furthermore, a repeatability study performed in some samples will be presented in order to give reliability to the measurement procedure used with both devices.

Finally, we will introduce the values obtained by means the measurements performed by the S-Neox for each sample, which include the height and the width of the liquid drop as well as the *Sdr* parameter related to the structure of the surface. We will then calculate the corresponding value of the contact angle by means of the developed measurement method to compare them with the ones obtained with the DSA-100. Initial conclusions obtained from this comparison will be the verification of the validity of the developed measurement method to measure contact angles.

6.2. Samples and measurements

The goal of this Ph.D. Thesis consists validating the previously presented developed measurement method on hydrophobic samples. However, we wanted to extend the scope of this validation to hydrophilic and superhydrophobic samples in order to perform a full validation. For this reason, we present the samples used in this Ph.D. divided according to their wetting properties, i.e. hydrophobic, hydrophilic or superhydropobic, also specifying the kind of substrate and the measurements performed with each device. Figure 6.1 shows some of the samples used in the study.

Figure 6.1 Pictures of samples S1 through S6 used in this Ph.D. Thesis to validate the developed measurement method.

Most of the samples consist on a glass substrate with coatings provided with different wetting properties from the hydrophobic to the hydrophilic range.

Some of these samples, in particular those that have been coated, were provided by the TWI and L'Urederra (LUR) research centres. For this reason, no information about the composition of the coating is given in this thesis since the formula of these coatings are of TWI and LUR property.

Different measurements were performed on these samples such as the contact angle and the surface energy (CA, SE) performed by the DSA-100, the measurement of the height and the width of the liquid drops to further calculate the contact angle as well as the *Sdr* parameter (L, h, Sdr), all three performed by the S-Neox. Furthermore, a repeatability study were also performed in two of the samples as well as a study of how the volume change over time (V vs T).

The set of samples are tabulated in next three tables where it is indicated the substrate of the sample, the wetting properties of the coating and the measurement performed with each device as well the supplier of the sample.

Table 6.1 Summary of the hydrophobic measured samples indicating the supplier, the substrate material and the measurements performed with both the DSA-100 and the S-Neox.

Hydrophobic samples					
Supplier	**Sample**	**Substrate**	**Coating**	**DSA-100 measurements**	**S-Neox measurements**
TWI	S1	Glass	Hydrophobic	CA, SE	L, h, Sdr
	S2	Glass	Hydrophobic	CA, SE Repeatability	L, h, Sdr Repeatability
	S3	Glass	Hydrophobic	CA, SE V vs T	L, h, Sdr
	S4	Glass	Hydrophobic	CA, SE	L, h, Sdr
	S5	Glass	Hydrophobic	CA, SE Repeatability	L, h, Sdr Repeatability
	S6	Glass	Hydrophobic	CA, SE	L, h, Sdr
LUR	S7	Glass	Hydrophobic	CA, SE	L, h, Sdr
	S8	Aluminium	Hydrophobic	CA, SE	L, h, Sdr

Table 6.2 Summary of the hydrophilic measured samples indicating the supplier, the substrate material and the measurements performed with both the DSA-100 and the S-Neox.

Hydrophilic samples					
Supplier	**Sample**	**Substrate**	**Coating**	**DSA-100 measurements**	**S-Neox measurements**
LUR	S9	Glass	None (Hydrophilic)	CA, SE	L, h, Sdr
	S10	Glass	Hydrophilic	CA, SE V vs T	L, h, Sdr
	S11	Aluminium	None (Hydrophilic)	CA, SE	L, h, Sdr

Table 6.3 Superhydrophobic sample, indicating the supplier, the substrate material and the measurements performed with both the DSA-100 and the S-Neox.

Superhydrophobic samples				
Supplier	**Sample**	**Substrate**	**DSA-100 measurements**	**S-Neox measurements**
TWI	S12	Glass	CA, SE	L, h, Sdr

Below, we will introduce the measurements performed with both the DSA-100 and the S-Neox, focusing on the parameters measured with each one. These parameters include the contact angle and the surface energy directly calculated by the DSA-100 and the height, the width of the liquid drop and the real area of sample that is used in the calculation of the surface structure (*Sdr*) by the S-Neox. All these measurements were performed at a temperature of 20°C with a relative humidity between 30-35% and both liquids at room temperature.

6.3. DSA-100 experimental measurements

6.3.1. Contact angle and surface energy measurements

To measure the contact angle with the DSA-100, we used water as well as Diiodomethane as measurement liquids. For each liquid, we deposited a 2 µL drop on the sample and we measured by means of the software its corresponding contact angle applying the height-width fitting method.

The reason why we selected the height-width fitting method in the DSA-100 to calculate the contact angles is due to the similarity with the method used to obtain the contact angle with the S-Neox by means of the developed measurement method. The calculations of the contact angle assumes a spherical shape for the drop and only involves h and . As was said before, both parameters are measured entirely by means the S-Neox. In this way, we do not take into account external sources of error such as the error in the volume of the drop introduced by the liquid dispenser.

The measurement procedure is repeated three times, so three different liquid drops of the same volume are measured for each liquid. The software gives us a mean contact angle value for each measurement liquid (θ Mean) and its standard deviation ($\delta\theta$).

Furthermore, the software calculates the surface energy (SE) according to Fowkes' method with the previous obtained values of the mean contact angles, and also provides the dispersive and the polar components.

Table 6.4 summarizes the mean contact angle calculated by the DSA-100 and its standard deviation obtained for each hydrophobic sample, measured with water and Diiodomethane as well as the total surface energy and its dispersive and polar components.

Table 6.4 Summary of the mean contact angle value and its standard deviation obtained by the DSA-100 in hydrophobic samples. The software also calculates the surface energy and gives the total surface energy as well as its dispersive and polar components.

	Water		Diiodomethane		Surface energy (mN/m)		
Sample	θ Mean (°)	$\delta\theta$ (°)	θ Mean (°)	$\delta\theta$ (°)	Total SE	Dispersive component	Polar component
S1	108.49	0.55	82.82	1.16	16.81	16.08	0.74
S2	119.27	1.46	88.84	0.10	13.27	13.22	0.05
S3	126.24	0.30	99.04	0.36	9.04	9.02	0.01
S4	100.70	0.93	75.09	0.52	21.57	20.07	1.49
S5	111.29	0.52	80.51	1.38	17.52	17.24	0.28
S6	120.55	0.25	93.04	0.54	11.48	11.39	0.09
S7	108.25	0.97	86.77	1.87	15.25	14.17	1.08
S8	110.05	0.84	90.82	1.12	13.45	12.34	1.11

The measurement of the contact angle of the hydrophilic samples was more complex than the measurement of the contact angle of the hydrophobic samples. One of the difficulties we met was the placement of the liquid drop on the surface. The drops tended to spread on hydrophilic surfaces in an irregular way and we generally needed more than three attempts to be able to place one that useful for measurement. This was traduced in about 10 deposited drops whereof only three of them were adequate to calculate the mean contact angle.

The other main problem was the fitting performed by the DSA-100, which was not as accurate as when performed for drops placed on hydrophobic samples. The fitting was completely unstable and it took a long time for it to stabilize. Sometimes too, the fitting did not recognize the contour of the drop.

The results obtained from these measurements performed on hydrophilic samples are shown in Table 6.5.

Table 6.5 Summary of the mean contact angle value and its standard deviation obtained by the DSA-100 in hydrophilic samples. The surface energy is also calculated by the software and gives the total surface energy as well as its dispersive and polar components.

	Water		Diiodomethane		Surface energy (mN/m)		
Sample	θ Mean (°)	$\delta\theta$ (°)	θ Mean (°)	$\delta\theta$ (°)	Total SE	Dispersive component	Polar component
S9	30.17	1.76	55.29	0.74	65.47	31.28	34.19
S10	25.56	0.85	41.49	1.13	70.44	38.85	31.59
S11	87.40	2.00	52.59	1.69	35.32	32.82	2.51

In the case of the superhydrophobic sample (S12), we performed the measurements with approximately 7 µL water drops since we need more volume to be able to place the drop on the surface. These measurements were only performed with water since the Diiodomethane spread completely on the surface, which did not allow performing the measurement.

Figure 6.2 shows the same water drop placed on the superhydrophobic surface, fitted by different fitting methods available in the DSA-100. The height-width fitting method does not seem to be the most appropriate.

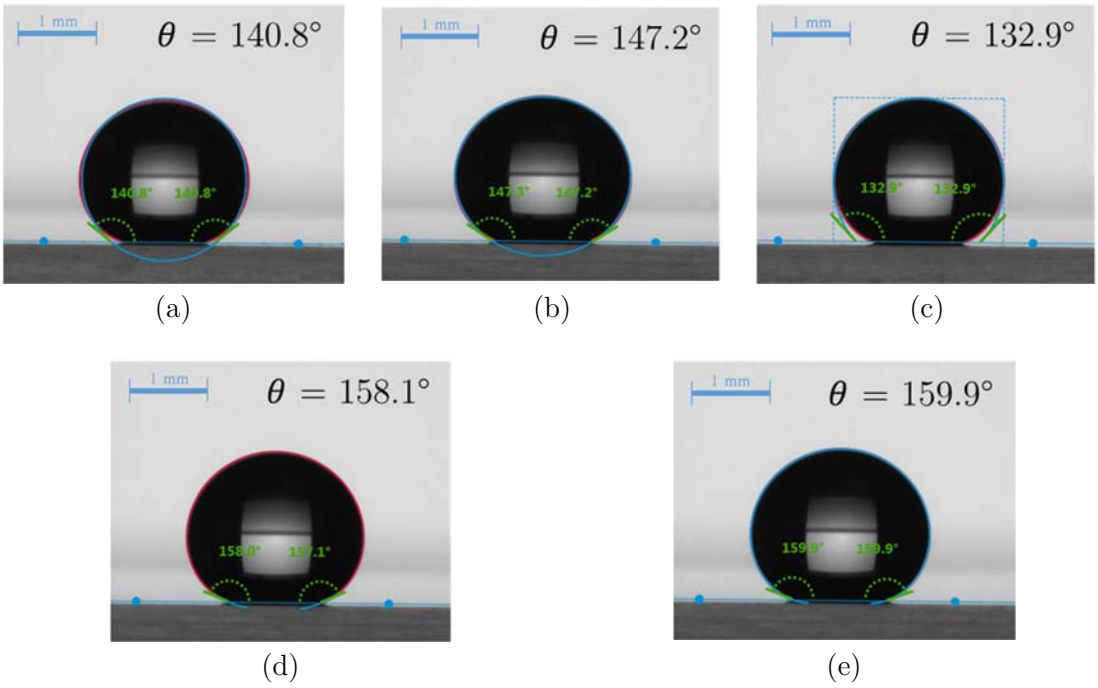

Figure 6.2 Pictures of the same 7 µL water drop placed on sample S12 with different fittings applied by the DSA-100 to calculate the contact angle: (a) circle, (b) Ellipse, (c) Height-width, (d) Tangent and (e) Young-Laplace fittings.

The measured value of the contact angle by the DSA-100 for the same water drop is completely different depending on the applied fitting method. Following the same procedure, each fitting was applied to each of the three water drops so we finally obtain a mean contact angle value and its standard deviation for each fitting, whose values are tabulated in Table 6.6.

Table 6.6 Summary of the mean contact angle value for water as a measurement liquid and its standard deviation measured by the DSA-100 for the superhydrophobic sample (S12) obtained different fittings.

S12 measured with water		
Fitting	**θ Mean (°)**	**$\delta\theta$ (°)**
Circle	139.13	2.22
Ellipse	147.23	2.51
Height-width	133.89	1.71
Tangent	158.08	3.84
Young-Laplace	159.68	4.85

The value of the standard deviation obtained for each fitting seems to suggest that the most appropriate is the height-width fitting, but looking at the image, we can easily see that the fitting is not well performed. According to the explained in previous chapters, when working with superhydrophobic samples, the best fitting method is the Young-Laplace since it takes into account the effect of the gravity on the liquid drop. This makes it the best choice in this case because the drops are bigger than the ones needed in hydrophobic samples and the gravity effects are more pronounced.

The high value obtained for the standard deviation could be due to the volume of the dispensed drop by means of the DSA-100. As superhydrophobic samples are water-repellent, we need drops with higher volumes to be able to place a drop on the surface. With higher volumes, the DSA-100 is less accurate than when dispensing smaller volumes. Furthermore, as the drop is not stuck on the surface it can be affected by any airflow, however small, and any movement of the drop at the time of fit its contour, could affect the measurement of the contact angle value.

6.3.2. Repetabilty of the measurements

In order to give reliability to the performed measurements, we wanted to test their repeatability.

To do that, we chose some samples that had already been measured by the procedure explained previously. For this study, we measured the contact angle in four different areas of the sample, with three different 2µL drops for each liquid, to obtain a mean value of the contact angle along the entire sample.

From these measurements, the DSA-100 performs an average to obtain a mean contact angle value for the entire sample that can be compared with the value obtained by the previous procedure.

In Table 6.7 are tabulated both the mean contact angles values obtained from the 3-drops method and the ones obtained by the 12-drops method. The standard deviation ($\delta\theta$) for each mean contact angle value is also shown for each measurement liquid.

Table 6.7 Comparison of the mean contact angle values obtained by the 3-drops method and the ones obtained by the 12-drops method for samples S2 and S5.

		Water			Diiodomethane		
Sample	**Method**	**θ Mean (°)**	**$\delta\theta$ (°)**	**St. Dev (°)**	**θ Mean (°)**	**$\delta\theta$ (°)**	**St. Dev (°)**
S2	3-drops	119.27	1.46	1.34	88.84	0.13	0.63
	12-drops	120.9	1.19		89.96	1.85	
S5	3-drops	111.29	1.03	0.05	80.51	1.65	0.42
	12-drops	111.6	0.78		81.42	0.97	

This study demonstrates the high repeatability of the measurement procedure used. The existing difference between the contact angle values obtained by both methods and each liquid will be due to the measurement error itself.

We will now introduce the measurements performed by the S-Neox which includes the measurement of the height and the width of the liquid drops and also the *Sdr* parameter.

We will also present the corresponding mean contact angle values calculated by applying the developed measurement method presented in Chapter 4 depending on the wetting properties of the sample, and the roughness factor r as explained in Chapter 5.

6.4. S-Neox experimental measures

6.4.1. Height, width and *Sdr* measurements

With the S-Neox, we first measured the Sdr parameter for the samples presented in Table 6.8, Table 6.9 and Table 6.10 at each position were the three different drops would be placed. The values shown in these tables correspond to an average of the three measured Sdr values along the sample. We verified that most of the samples have their coating homogeneously deposited so the values of the Sdr for the same sample have a dispersion lower than 0.01%.

Furthermore, we have also measured the height (h) and the width (L) of three different 2 µL drops, with both water and Diiodomethane as measurement liquids. The mean values of L and h of each sample are also presented in the following tables as well as the corresponding standard deviation for each mean value.

Table 6.8 Summary of the mean values of h and L measured for three different 2µL drops of both water and Diiodomethane measured by the S-Neox on hydrophobic samples as well as the mean value of the *Sdr* of each sample.

	Water				Diiodomethane				
Sample	L Mean (mm)	δL (mm)	h Mean (mm)	δh (mm)	L Mean (mm)	δL (mm)	h Mean (mm)	δh (mm)	Sdr (%)
S1	1.805	0.016	1.180	0.013	2.361	0.021	1.021	0.026	0.79
S2	1.745	0.011	1.312	0.022	2.783	0.023	1.021	0.013	1.01
S3	1.764	0.013	1.410	0.011	1.724	0.012	0.987	0.019	0.49
S4	1.980	0.010	1.142	0.021	2.520	0.014	0.830	0.022	0.04
S5	1.840	0.019	1.240	0.020	2.168	0.017	0.883	0.025	0.42
S6	1.756	0.015	1.325	0.009	2.470	0.015	0.940	0.018	0.16
S7	1.916	0.023	1.254	0.014	2.278	0.027	1.047	0.022	0.32
S8	1.895	0.017	1.278	0.022	2.030	0.011	1.056	0.027	0.70

As with the DSA-100, we also met several problems to measure h and L in hydrophilic samples. For such samples, the width of the drop is larger than for drops placed on hydrophobic surfaces and they do not fit in the field of view of the 5X microscope objective. We then tried to perform an extended image of the drop but the movement of the sample holder was transferred to the drop resulting in a blurred and fragmented image of the drop. As the software of the S-Neox has no the option to leave some seconds holder movement ad image acquisition when performing an extended image, the drop cannot be stabilizedand the problem cannot be overcome. We therefore had to change to a 2.5X microscope objective to be able to perform the image of the drop.

In order to measure h, we also had to change the microscope objective from the 10X to a 5X because otherwise we could not see the apex of the drop and the surface of the sample at the same time in the field of the microscope objective. The measured h and L in the hydrophilic samples are shown in Table 6.9 together with the measured value of the *Sdr.*

Table 6.9 Summary of the mean values of h and L measured with the S-Neox for three different 2µL drops of both water and Diiodomethane on hydrophilic samples, together with the mean value of the *Sdr* of each sample.

	Water				Diiodomethane				
Sample	L Mean (mm)	δL (mm)	h Mean (mm)	δh (mm)	L Mean (mm)	δL (mm)	h Mean (mm)	δh (mm)	*Sdr* (%)
S9	2.498	0.011	0.349	0.010	3.311	0.013	0.724	0.025	0.02
S10	2.325	0.035	0.406	0.009	3.128	0.022	0.706	0.017	0.01
S11	2.159	0.029	1.078	0.018	2.974	0.018	0.780	0.022	0.33

For the superhydrophobic sample, we also measured the drop parameters with 7µL drops. Otherwise, we were not able to place the drop on the surface. The mean values of h and L are reported in Table 6.10 as well as the value of the *Sdr*.

Table 6.10 Summary of the mean values of h and L measured f by the S-Neox for three different 7µL water drops on superhydrophobic samples, together with the mean value of the Sdr.

Water					
Sample	L Mean (mm)	δL (mm)	h Mean (mm)	δh (mm)	Sdr (%)
S9	2.275	0.039	2.702	0.053	0.02

From these measured parameters, we are able to calculate the corresponding contact angles values with the h, L model presented in Chapter 4. We also calculated the value of the roughness factor r as explained in Chapter 5. All these parameters are shown in Table 6.11, Table 6.12 and Table 6.13.

Table 6.11 Calculated contact angle values and their standard deviation, for both water and Diiodomethane and the r factor for the set of hydrophobic samples.

	Water		Diiodomethane		
Sample	Calculated θ Mean (°)	$\delta\theta$ (°)	Calculated θ Mean (°)	$\delta\theta$ (°)	r
S1	107.91	0.33	82.23	0.05	1.0079
S2	120.25	0.16	74.56	0.09	1.0101
S3	126.77	0.10	98.34	0.10	1.0049
S4	98.83	0.07	70.05	0.09	1.0004
S5	110.35	0.14	79.31	0.06	1.0042
S6	120.60	0.30	76.18	0.07	1.0016
S7	108.00	0.28	85.37	0.17	1.0032
S8	110.41	0.14	92.32	0.06	1.0070

Table 6.12 Calculated contact angle values and their standard deviation, for both water and Diiodomethane and the r factor for the set of hydrophilic samples.

	Water		Diiodomethane		
Sample	Calculated θ Mean (°)	$\delta\theta$ (°)	Calculated θ Mean (°)	$\delta\theta$ (°)	r
S9	31.22	0.24	47.23	0.22	1.0002
S10	38.50	0.65	48.59	0.15	1.0001
S11	89.92	0.32	55.35	0.16	1.0033

Table 6.13 Calculated contact angle value and its standard deviation, for both water and Diiodomethane and the r factor for the superhydrophobic sample.

Water			
Sample	Calculated θ Mean (°)	$\delta\theta$ (°)	r
S12	133.12	0.35	1.0002

Before we proceed with the validation of these mean contact angles calculated by means the application of the developed measurement method, we must verify that these measurements are also as reliable as the ones performed with the DSA-100. We therefore, present the repeatability study performed with the S-Neox.

6.4.2. Repetabilty of the measurements

As was also done with the DSA-100, we selected samples S3 and S5 to perform the repeatability study. The procedure was the same; we measured the height and the width of 12 different drops, all with a volume of 2µL, with both water and Diiodomethane as measurement liquids, and we compared the values with the ones obtained in section 6.4.1 for these samples.

In Table 6.14 are tabulated both the mean L and h values obtained from the 3-drops method and the ones obtained by the 12-drops method with their corresponding standard deviation for each measurement liquid.

With these values, we can conclude that the measurement procedure performed by the S-Neox is as reliable as the one performed by the DSA-100.

Once the reliability of the measurement procedures performed by both devices has been proved, we must deal with a possible situation that we could face when working with liquids, regardless of the device being used. As we are aware, liquids evaporate depending on the environment conditions. This evaporation could obviously affect our type of measurements. For this reason, we decided to study how the volume of a drop placed on a surface under measurement changes with time. The results will be presented in the following section.

Table 6.14 Comparison of the mean h and L values obtained by the 3-drops method and the ones obtained by the 12-drops method for samples S2 and S5.

		Water				Diiodomethane			
Sample	**Method**	L Mean (mm)	St. Dev. (mm)	h Mean (mm)	St. Dev. (mm)	L Mean (mm)	St. Dev. (mm)	h Mean (mm)	**St. Dev. (µm)**
S2	3-drops	1.745	0.012	1.312	0.019	2.783	0.21	1.021	0.014
	12-drops	1.759		1.320		2.763		1.035	
S5	3-drops	1.840	0.017	1.240	0.020	2.168	0.019	0.883	0.022
	12-drops	1.832		1.244		2.189		0.901	

6.5. Evolution of the volume of the drop with time

Under a controlled atmosphere at a temperature of 20°C and a relative humidity between 30-35%, we monitored the evolution of the volume of a drop taking advantage of the DSA-100 software.

The measurement consisted of recording a two-minute video of a deposited drop on two different samples, one hydrophilic and the other one hydrophobic, with the two measurement liquids, water and Diiodomethane. From this video, every 15 seconds we took a snapshot from the side view of the drop and applying a fitting method we obtained the value of the volume calculated by the DSA-100 software at each moment.

The recorded evolution of the volume with time plotted in Figure 6.3 shows that, even though both liquids show some evaporation, water drops have a notable loss of volume compared to the Diiodomethane ones, in the same range of time of 2 minutes, regardless of the wetting properties of the samples.

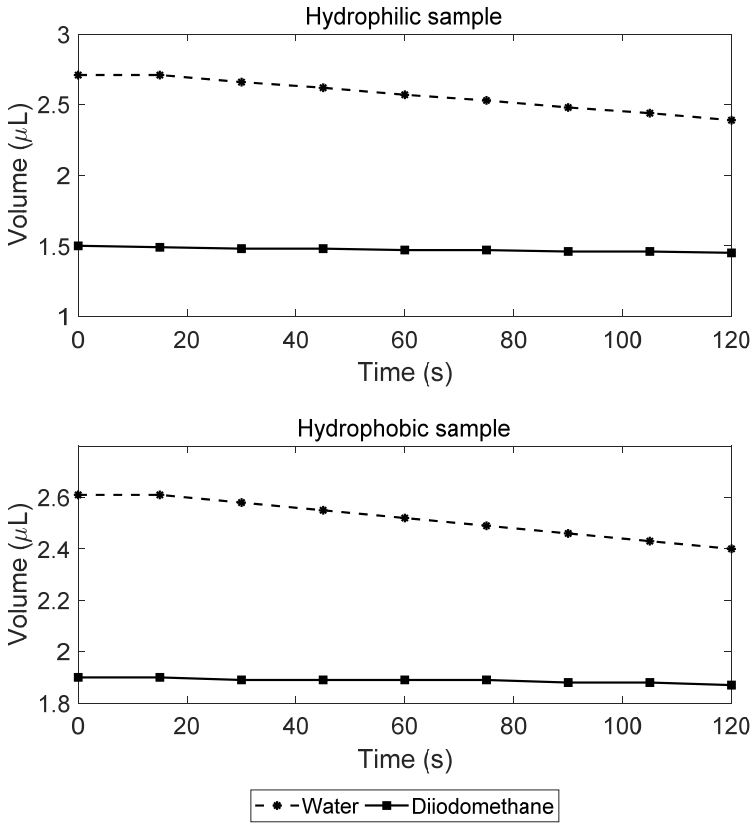

Figure 6.3 Plot of the evolution of the volume of a drop with time of both water and Diiodomethane as measurement liquids placed on a hydrophilic and a hydrophobic sample.

Time is an important parameter to take into account when working with liquids so the measurements must be performed in a range of time where these losses are minimum. On the one hand, the time taken to perform a contact angle measurement by the DSA-100 can be as short as 30 seconds, whereas the measurement of the height and the width of the

drop by means the S-Neox can take 45 seconds. According to these times, a summary of the volume losses are presented in Table 6.15, depending on the wetting properties of the sample and the device used to perform the measurement.

Table 6.15 Summary of the volume losses according to the wetting properties of the sample under study and the device with which the measurements are performed.

Loss of volume over time			
		Hydrophilic sample	Hydrophobic sample
DSA-100	Water	2.0%	1.0%
	Diiodo	1.0%	0.5%
S-Neox	Water	3.0%	1.0%
	Diiodo	2.0%	0.5%

In both cases, the loss of volume of a water drop is higher than the loss of volume suffered in the case of a Diiodomethane drop, which can be explained due to their heat capacities.

Heat capacity is defined as the quantity of heat transferred to a body that increases its temperature 1 unit of temperature. Water has a heat capacity of 75.4 $J/K \cdot mol$ [91] compared to the heat capacity of the Diiodomethane which is 133 $J/K \cdot mol$ [92] both at a temperature of 25°C. This difference makes water to be more volatile in an air atmosphere and at temperature and humidity conditions presents in our measurements, than the Diiodomethane in agreement with the observed behaviour. Furthermore, when the sample under study is hydrophilic, the surface-to-volume ratio of the drop increases, and the resulting evaporation rate is higher than for hydrophobic samples.

Even so, these losses of volume in the range of time taken to perform the measurement with both devices is actually quite small and considered to be within the experimental measurement error since the losses are less than 2%. Therefore, we can consider that, under our ambient conditions, the results are not affected by the evaporation suffered by the liquids drops during the time in which the measurements are being performed.

Another important factor to take into account is how the drop is illuminated since the way of illuminate the drop can increase the evaporation rate.

In the case of the DSA-100, the drop is illuminated with backlight coming from a light source placed behind a diffuser plate. The quantity of light received by the liquid drop is therefore quite small and does significantly contribute to its heating.

The S-Neox [93] has an illumination system completely different to the one from the DSA-100. This device needs the light reflected by the sample to be able to perform the measurement so, when measuring h and L, it illuminates directly the liquid drop and some of the light passes through it. In this case, different factors such as the absorption spectrum of water and Diiodomethane and the spectral distributions of the LEDs and their

corresponding dichroic filters, used in the S-Neox, must be taken into account since they can encourage the loss of volume of the drops through heat contribution.

From the absorption spectrum of both liquids, shown in Figure 6.4, we can observe that, on the one hand, water is relatively transparent to visible light and absorbs most ultraviolet and infrared light. On the other hand, Diiodomethane has its maximum absorption centered on the ultraviolet range (shown in the following figure), and is mostly transparent to the visible light.

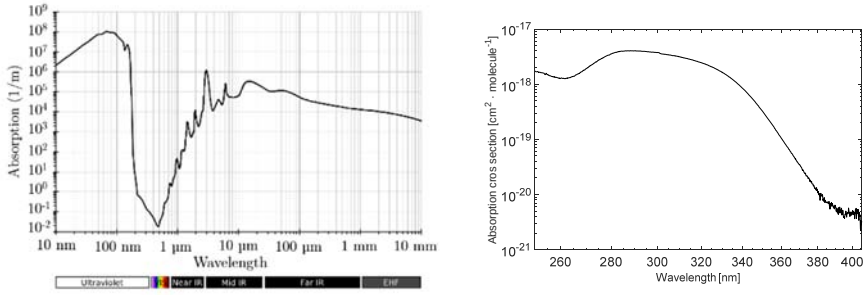

(a) (b)

Figure 6.4 (a) Absorbance spectrum of water and (b) absorption cross-section of Diiodomethane. Sources: [94], [95].

The measurement of h and L of a drop with the S-Neox was performed illuminating with the green LED with which the device is equipped. The spectral distribution, shown in Figure 6.5, has its peak at a wavelength of 530 nm.

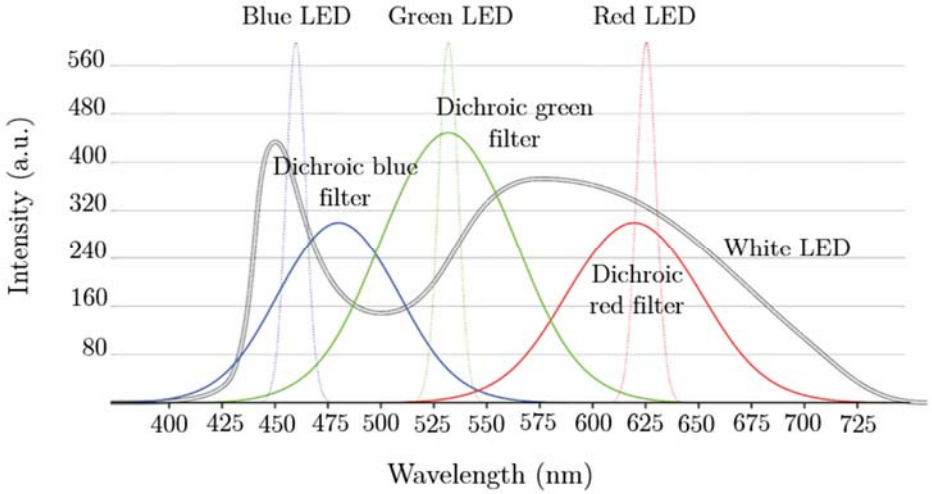

Figure 6.5 Spectral distribution of the three LED blue (460 nm), green (530 nm) and red (630 nm) and their corresponding dichroic filters as well for the white LED with which the S-Neox is equipped. Source: [93].

From this data, we can surmise that neither water nor Diiodomethane will absorb heat provided from the light source since they are very transparent in the range were the set green LED – dichroic green filter has its peak of spectral distribution. Even so, we decided to evaluate the temperature increase of the water drop due to the illumination of the light source over the time taken to perform the measurement. In order to do this, we measured the power that reaches the drop from the green LED by means an optical power meter.

The spotlight of the LED that reaches the liquid drop covers all the area filled by the drop. As we were usually working with 2µL drops, from the measurements performed in the set of hydrophobic samples, the mean height of these drops is 1.8 mm.

The heat capacity (C) of a material is defined as the absorbed heat (Q) divided by the temperature increase (ΔT) as stated in equation (2.23).

$$C = \frac{Q}{\Delta T} \tag{6.1}$$

The heat capacity can be also expressed as the specific volumetric heat capacity (C_{esp}) multiplied by the volume (V) of the liquid drop and the energy absorbed by the liquid drop is the absorbed power (P_{abs}) over the time taken to perform the measurement (t). Replacing these parameters in equation (2.23), we finally obtain the temperature increase expressed as equation (6.2) shows.

$$\Delta T = \frac{P_{abs} \cdot t}{C_{esp} \cdot V} \tag{6.2}$$

The absorbed power is the difference between the power that reaches the liquid drop (P_{in}), which is by the power meter, and the power that goes through the drop and comes out again (P_{out}). P_{out} is calculated according to equation (6.3) taking into account the absorbance coefficient (α) of water at the wavelength of the light source, obtained from Figure 6.4(a), and the distance travelled by the light through the liquid drop (L), which is (to take a maximum value) two times the height of the drop.

$$P_{out} = P_{in} \cdot e^{-\alpha L} \tag{6.3}$$

The values of the different parameters involved in the calculations are shown in Table 6.16 as well as the resulting temperature increase of the drop.

Table 6.16 Value of the different parameters involved in the calculation of the temperature increase of a drop of water illuminated by the green LED of the S-Neox during the time taken to perform the measurement.

C_{esp} $\left(\frac{J}{m^3\,°C}\right)$	t (s)	V (m^3)	α (m^{-1})	L (m)	P_{in} (J/s)	P_{out} (J/s)	P_{abs} (J/s)	ΔT $(°C)$
4185	45	$2 \cdot 10^{-9}$	10^{-2}	$3.60 \cdot 10^{-6}$	$2.40 \cdot 10^{-5}$	$2.39 \cdot 10^{-5}$	$8.64 \cdot 10^{-9}$	0.05

The maximum temperature increase of the water drop during the measurement with the S-Neox is around 0.05°C. Therefore, we can conclude that the light source is adequate for these measurements and does not contribute significantly to the evaporation.

After these verifications, we can recommend the best measurement conditions that would consists on:

- working in a controlled environment where the relative humidity does not exceed (or go much lower than 35%) and a maximum temperature of 22°C
- to not illuminate the liquid drops with high light powers that would in any case not suit the measurement procedure because the detector of the device would saturate,
- keep the measurement time of h and L under 1 minute and,
- whenever possible, keeping the liquid drops under 5 microliters in order for the spherical approximation of the drop to work.

At this point, the final step in this chapter consists on comparing the values obtained from the direct measurement of the contact angle by means of the DSA-100 and the ones calculated with our mathematical method.

6.6. Validation of the calculated contact angles

To validate the values of the contact angles in hydrophobic samples obtained from the S-Neox measurements, we will directly compare those values with the ones obtained with the measurements performed with the DSA-100.

Table 6.17 Comparison between the contact angles measured with the DSA-100 and the ones calculated by the developed measurement method using the S-Neox in hydrophobic samples.

	Water			Diiodomethane		
	DSA-100	S-Neox		DSA-100	S-Neox	
Sample	θ Mean (°)	θ Mean (°)	Difference	θ Mean (°)	θ Mean (°)	Difference
S1	108.49	107.91	0.54%	82.82	82.23	0.71%
S2	119.27	120.25	0.82%	88.84	74.56	16.08%
S3	126.24	126.77	0.42%	99.04	98.34	0.71%
S4	100.70	98.83	1.86%	75.09	70.05	6.72%
S5	111.29	110.35	0.84%	80.51	79.31	1.49%
S6	120.55	120.60	0.05%	93.04	76.18	18.12%
S7	108.25	108.00	0.23%	86.77	85.37	1.62%
S8	110.05	110.41	0.33%	90.82	92.32	1.65%

At first glance, one can appreciate that the contact angle values obtained by applying the measurement method in the S-Neox are essentially the same than the ones obtained by the DSA-100 when measuring with water. Conversely, the values of the contact angles

obtained with Diiodomethane by applying the measurement method with the S-Neox have a strong difference with the ones obtained by the DSA-100 in most cases, with several epic fails.

On the other hand, as we already commented, the wetting properties of the samples depend on their chemical compositions and their surface microstructure but also depend on the liquid used to perform the measurements. As we can see, a sample that presents a contact angle of 108.49° (S1) with water, has a contact angle of 82.82° for Diiodomethane, an angle below 90º. This fact can be related with the behaviour presented by Wenzel model introduced in Chapter 3. At the time to evaluate the surface energy of these samples, the behaviour of each component must be taken into account when evaluating the total surface energy.

Although the main aim of this Ph.D. Thesis is to validate the developed measurement method on hydrophobic samples, we will also compare the contact angle values obtained for the measured set of hydrophilic samples with both devices to understand if the developed measurement method is also valid for contact angles in the hydrophilic regime.

Table 6.18 compares the values of the contact angles obtained by means of both devices for the set of hydrophilic samples. As we can see, in general, the smaller the contact angle value the more the difference between the contact angles obtained by the DSA-100 and the S-Neox, regardless of the measurement liquid.

Table 6.18 Comparison between the measured contact angles by the DSA-100 and the ones calculated by the developed measurement method using the S-Neox in hydrophilic samples.

	Water			Diiodomethane		
	DSA-100	S-Neox		DSA-100	S-Neox	
Sample	θ Mean (°)	θ Mean (°)	Difference	θ Mean (°)	θ Mean (°)	Difference
S9	30.17	31.2	3.49%	55.29	47.23	14.58%
S10	25.56	38.50	50.64%	41.49	48.59	17.11%
S11	87.40	89.92	2.88%	52.59	55.35	5.26%

The very large difference can be due to different facts, however, it is likely that the calculation of the contact angle from h, and L is not the most appropriate for drops that spread widely, especially due to the Field-of-view considerations already explained in Chapter 5, which translate in a loss of accuracy in the measurement of both parameters. Therefore, the developed measurement method in its current form is not valid for very hydrophilic samples. As we developed three different mathematical methods to calculate the contact angle by the parameters measured with the S-Neox, further steps would consist in trying out the other two mathematical methods in order to check whether the error is reduced by substituting one of the parameters by V. However, as was said, since our aim was to validate the measurement method on hydrophobic samples, these further steps are out of the scope of this present thesis.

Even so, as was pointed out in Chapter 5, even with the DSA-100 or other commercial devices, the measurement of the contact angle for hydrophilic samples is an arduous process that needs to be improved or be performed in different measurement conditions than the ones used to measure the contact angle in hydrophobic samples. With the DSA-100, the fitting was not as accurate and reliable when measuring the contact angle in hydrophilic samples as when measuring it in hydrophobic samples.

Finally, another explanation for the large difference between contact angles could be found in the loss of volume of drops when measuring on hydrophilic samples. As was shown, the greatest loss of volume take place when measuring with water in hydrophilic samples. As the losses are around 3%, it could be considered that this loss of volume during the measurement further lowers the measurement accuracy of the parameters.

The comparison between the contact angles obtained by both devices for the superhydrophobic sample must take into account that we need to compare the values obtained by the height-width fitting although the Young-Laplace method performs the best measurement fitting. This comparison can only be made for water as a measurement liquid, as shown in Table 6.20, since we could not measure with Diiodomethane because the drops spread completely on the surface.

Table 6.19 Comparison between the contact angle measured with the DSA-100 and the one calculated by the developed measurement method using the S-Neox in the superhydrophobic sample for water.

Water			
	DSA-100	S-Neox	
Sample	θ Mean (°)	θ Mean (°)	Difference
S9	132.89	133.12	0.178%

The value of the contact angle obtained with the measurement method developed for the S-Neox is practically equal to the one calculated by the DSA-100. Therefore, we confirm that the developed measurement method is also valid to obtain contact angles in superhydrophobic samples as DSA-100 does by the height-width fitting method. However, we must keep in mind that, as shown in Chapter 5, the spherical assumption is not perfectly valid when measuring on superhydrophobic samples, which need larger volumes for the drop to set. Therefore, the value obtained for the superhydrophobic samples is not perfectly accurate.

From these comparisons, we have obtained encouraging results that allow us to confirm the validity of the developed measurement method to calculate the contact angle in hydrophobic samples by means of a confocal device. We have therefore developed a valid measurement method and its corresponding mathematics that allows us to measure both the topography and the contact angle of a hydrophobic sample with a single device. This guarantees the reliability required to further evaluate the surface energy of hydrophobic

samples with the correction of the effect of the roughness of the surface in the contact angle according to Wenzel's model.

6.7. Correction of the effect of the roughness in the calculated contact angles

Since the validity of the developed measurement method to calculate the contact angle on hydrophobic surfaces by means of the parameters provided by the S-Neox has been proved, the next step consists in correcting the effect of the roughness of the surface on the contact angles according to Wenzel's model introduced in Chapter 3. The correction of the contact angle will be made according to equation (6.4) which comes from equation (3.2).

$$cos\,\theta_Y = \frac{1}{r} \cdot cos\,\theta_W \tag{6.4}$$

where θ_W corresponds to the observed contact angle, calculated by means of the parameters provided by the S-Neox and θ_Y is Young's contact angle, corrected of the effect of the roughness of the surface, also measured by means of the confocal device.

The correction of the effect of the roughness will be made only for those samples whose difference between the measured contact angle by the DSA-100 and the calculated by the parameters provided by the S-Neox is less than 2% with both measurement liquids.

Table 6.20 summarizes the r factor calculated for each hydrophobic sample as well as the corrected contact angle according to Wenzel's model for samples S1, S3, S5, S7 and S8.

Table 6.20 Values of the contact angles corrected (θ_Y) of the effect of the roughness of the surface according to Wenzel's model in hydrophobic samples for both water and Diiodomethane.

S-Neox					
		Water		Diiodomethane	
Sample	r factor	Calculated θ Mean (°)	θ Mean corrected (°)	Calculated θ Mean (°)	θ Mean corrected (°)
S1	1.0079	107.91	107.76	82.23	82.29
S3	1.0049	126.77	126.56	98.34	98.30
S5	1.0042	110.35	110.26	79.31	79.36
S7	1.0032	108.00	107.94	85.37	85.38
S8	1.0070	110.41	110.26	92.32	92.30

These values of the contact angles corrected by the effect of the roughness follow the behaviour predicted by Wenzel's model as the roughness of the surface enhances the wetting properties of the surfaces. This means that the corrected contact angle is smaller than the observed one in the hydrophobic regime. Conversely, in the hydrophilic regime, the corrected contact angle is larger than the observed one.

We will therefore be able in the following chapter to evaluate the surface energy of the hydrophobic measured samples with more reliability than the ones provided by the DSA-100 since this device does not take into account the effect of the roughness and our developed measurement method does.

Something that should be pointed out is that the set of samples used, do not have large values of roughness. As the validity of the measurement method to calculate the contact angle on hydrophobic samples has been demonstrated, and as one of the goals of this Ph.D. Thesis consists on correcting the effect of the roughness of a surface in its contact angle, we wanted to go further with real samples in which the roughness has an important role.

6.8. Contact angle calculation in naturally-structured samples

Once the validity of the calculation of the contact angle by means of the developed measurement method have been demonstrated, we wanted to apply the same procedure but in samples that can be found in nature. Specifically, the following introduced samples are plants that have a particular surface structure, with larger roughness than the previous samples, which gives them larger hydrophobicity.

Figure 6.6 shows the samples used in these last measurements were the surface structure plays an important role. Concretely, we used a Photus leaf, a petal of a Gerbera and a petal of a rose.

For the topography measurement of more complex surfaces than the ones already measured, we needed to change to a microscope objective with larger magnification than the used until now. Concretely, we used a 50X microscope objective since the structure of the surfaces have sizes of 10 µm and larger slopes that cannot be measured with smaller magnifications.

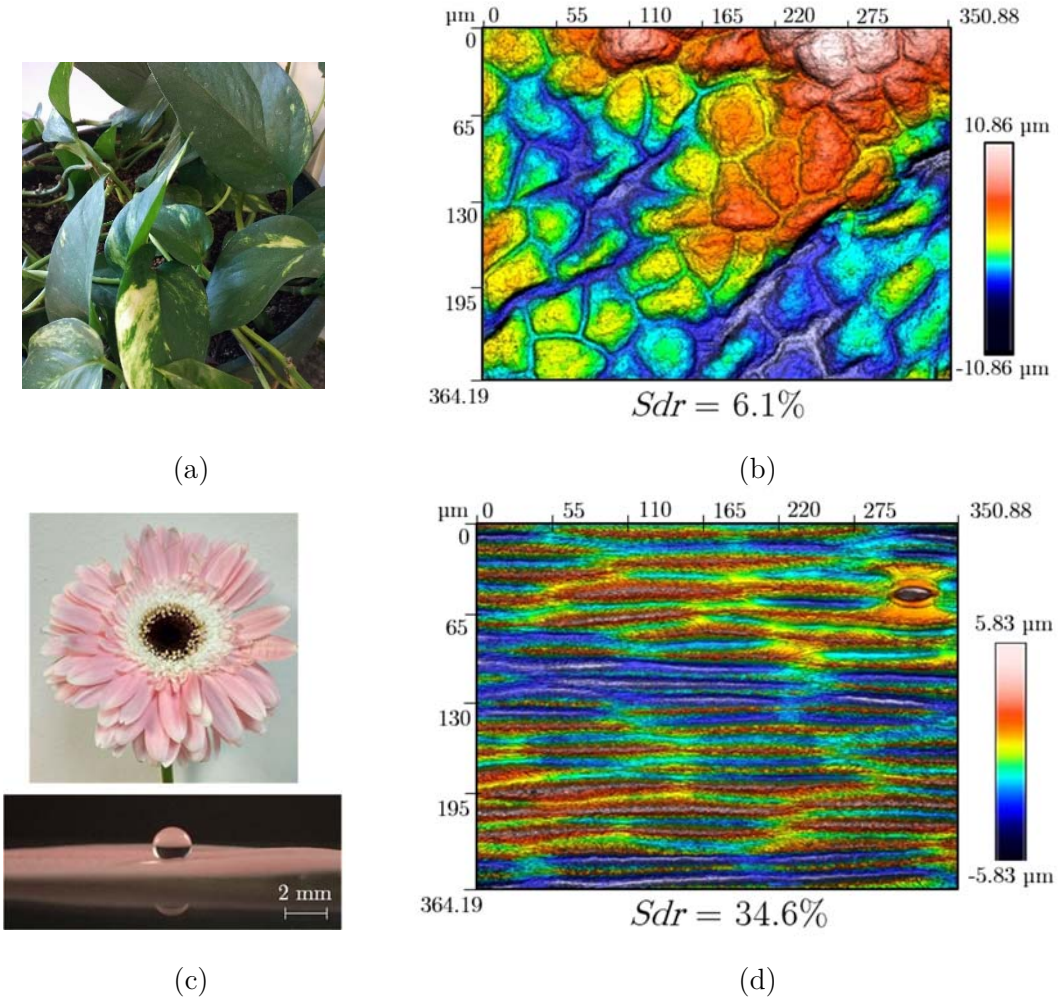

Figure 6.6 (a) Optical image of a Photus plant, (b) surface topography of the Photus leaf measured by the S-Neox with a 50X microscope objective to obtain the *Sdr* factor; (c) optical image of Gerbera and a drop placed on the surface of a Gerbera's petal and (d) surface topography of the Gerberas's petal measured by the S-Neox with a 50X microscope objective to obtain the *Sdr* factor.

As can be seen, the values of the *Sdr* factor are much larger than the ones obtained with the samples that have been used to validate the developed measurement method. With these samples, we also performed the same previous procedure to obtain a mean value of h and L and calculate the corresponding contact angle for each one with 4µL drops in order to no introduce the effect of the gravity in the drop, shown in Table 6.21. The measurements were performed with water since the samples are superhydrophobic and the Diiodomethane spreads on their surfaces.

Table 6.21 Mean values of h and L measured with 4µL liquid drops and the value of the Sdr obtained by the S-Neox of the selected real samples.

S-Neox			
Sample	L Mean (mm)	h Mean (mm)	θ Mean (°)
Photus leaf	2.313	1.535	109.15
Gerbera petal	2.021	1.769	138.61

The next step consists in correcting the contact angle with the roughness of the sample. The correction of the roughness of the sample is performed according to Wenzel's model and the resulting values are shown in Table 6.22.

Table 6.22 Correction of the contact angle value with the r factor according to Wenzel's model.

S-Neox			
Sample	Sdr (%)	r	θ Mean corrected (°)
Photus leaf	6.10%	1.061	107.94
Gerbera petal	34.6%	1.346	123.87

In these samples, whose structures provides the surface with larger roughness, we can observe the impact of correcting with Wenzel's method more notably than in the first set of samples. The corrected values (θ_Y) according to Wenzel's model are much smaller than the observed ones, since they take into account the roughness of the surface.

The rose petal was another sample in which we have great interest since it is key in most of the superhydrophobic studies found in the bibliography. What we met when measuring the topography of the rose petal was the limits of the S-Neox with this kind of surface structures.

As Figure 6.7 shows, the surface of a rose petal presents a structure that contains a pillar pattern. The shape of these pillars have slopes that the S-Neox is not able to measure so the surface topography has a black background. Since the S-Neox is not able to obtain the topography of the entire structure of those pillars by means of any available magnification, the *Sdr* cannot be measured in this case.

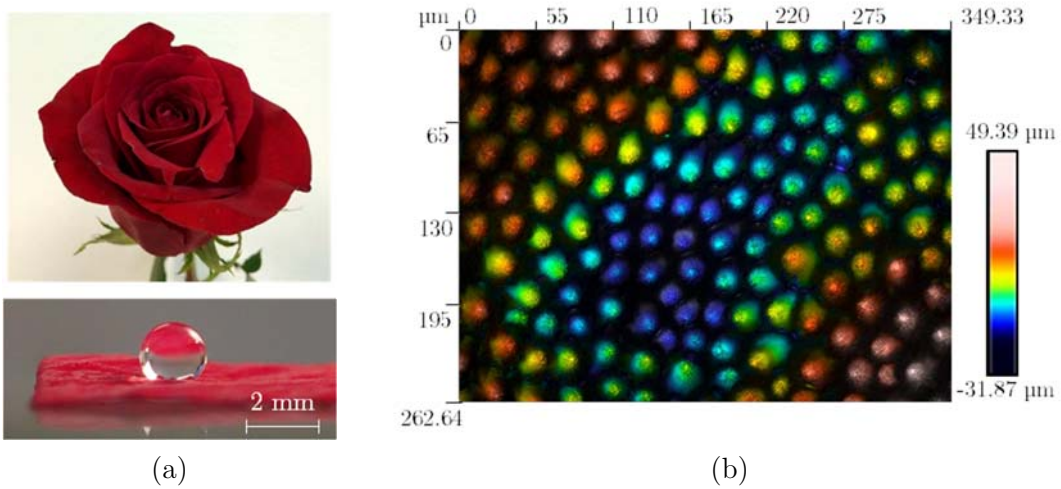

(a) (b)

Figure 6.7 (a) Optical image of a rose and a petal with a drop placed on the surface. (b) surface topography measured by the S-Neox with a 50X microscope objective to obtain the *Sdr* factor.

In most cases found in the bibliography, the surfaces images of this kind of samples are obtained by means of a Scanning Electron Microscopy (SEM) [96], [97], as the one shown in Figure 6.8. The pillars which are scattered over the surface of the petal rose have great slopes that the S-Neox is not able to measure.

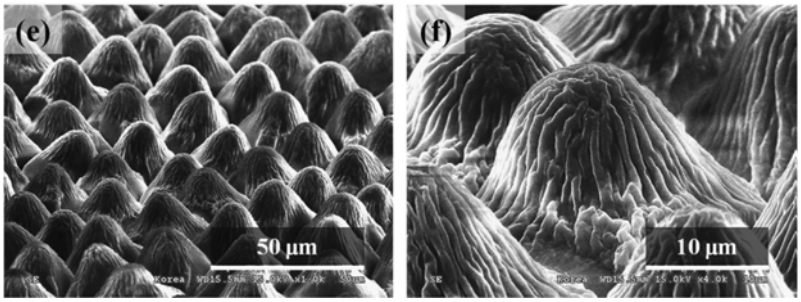

Figure 6.8 SEM image of the surface of a petal rose where the entire pillar-structure can be seen. Source: [97]

In any case, we were able to measure the contact angle in the rose petal with water as the measurement liquid and the results are shown in Table 6.23.

Table 6.23 Correction of the contact angle value with the r factor according to Wenzel's model.

S-Neox			
Sample	***L*** Mean (mm)	***h*** Mean (mm)	***θ*** Mean (°)
Rose petal	2.104	1.850	139.91

Comparing this value with the one obtained for the Gerbera's petal, we can expect that, if we wanted to calculate the surface energy from this measured contact angle, the

error that we would make by not taking into account the roughness of the rose petal would be relevant.

Next chapter will introduce the evaluation of the surface energy of those samples in which the validation of the calculation of the contact angle by means of the developed measurement method have been successfully validated. The evaluation will be performed with the corrected contact angles by the effect of the roughness of the surface presented in section 6.7. Unfortunately, the evaluation of the surface energy in samples such as superhydrophobic or the plant samples presented in this last section, will not be performed due to the impossibility to measure the contact angle with Diiodomethane as a measurement liquid.

7. Surface energy evaluation

7.1. Introduction

After the validation of the calculation of the contact angle by means of the developed measurement method on hydrophobic surfaces, we are going to evaluate the surface energy according to the OWRK method, introduced in Chapter 5, only for those samples where the contact angle are valid (that is, hydrophobic samples with valid measurements with the diiodomethane drop) . The evaluation will be made with the values of the contact angles that have been already corrected by the effect of the roughness of the surface according to Wenzel's model.

Furthermore, we will compare the values of the surface energy that takes into account the roughness of the surface with the ones obtained by the DSA-100. With this, we will demonstrate that the developed measurement method is a powerful tool to evaluate the surface energy of a hydrophobic sample taking into account the effect of the roughness. All the required measurements are performed by means of a confocal device, and even then, the result is provided with less error than when performing the measurement with a commercial contact angle meter that does not take into account the roughness of the surface.

7.2. Evaluation of the surface energy from the measurements performed with the S-Neox.

The evaluation of the surface energy according to OWRK's method performed by means of the DSA-100 from the measurement of the contact angle was introduced in Chapter 5. As a reminder, the OWRK method considers that the total surface energy (γ_S) of a solid has two main contributions, the dispersive (γ_S^d) and the polar (γ_S^p) ones and are expressed as equations (2.4) and (5.2) respectively shows.

$$\gamma_S^d = \frac{\gamma_L^d}{4}(1 + cos\,\theta_D) \tag{7.1}$$

Where γ_L^d is the dispersive component of the Diiodomethane and θ_D is the contact angle measured with Diiodomethane, and

$$\gamma_S^p = \frac{1}{\gamma_L^p}\left(\frac{\gamma_L^T}{2}(1 + cos\,\theta_P) - \sqrt{\gamma_S^d \gamma_L^d}\right)^2 \tag{7.2}$$

where γ_L^T is the total surface energy of the water, γ_L^p and γ_L^d are the polar and the dispersive component of the surface energy of water respectively, and θ_P is the contact angle measured with water.

At this point, we will use the previous mathematical expressions to evaluate the surface energy with the corrected calculated values of the contact angles obtained by means of the developed measurement method using the S-Neox only for those samples whose contact angles are valid for both liquids in Chapter 6.

As we worked with two different liquids, the dispersive component of the surface energy will be evaluated with Diiodomethane, as it is a pure dispersive liquid. On the other hand, the polar component of the surface energy will be evaluated with water. Table 7.1 shows the values of the polar and dispersive components of both liquids.

Table 7.1 Surface energy values for water and Diiodomethane.

	Surface energy (mN/m)		
	Total	Dispersive	Polar
Water	72.8	22.6	50.2
Diiodomethane	50.8	50.8	0.0

The evaluation of the surface energy is performed in hydrophobic samples where the correction of the effect of the roughness in the contact angle has already been performed. Table 7.2 shows the values of the surface energy for hydrophobic samples S1, S3, S5, S7 and S8, calculated with the corrected contact angle values obtained by the developed measurement method.

Table 7.2 Values of the total surface energy (Total SE) and its dispersive and polar components calculated from the corrected contact angles measured in the hydrophobic samples by means of the developed measurement method.

Surface energy evaluation (mN/m)			
Sample	Total SE	Dispersive component	Polar component
S1	15.45	14.40	1.05
S3	10.89	10.87	0.02
S5	15.62	15.05	0.57
S7	14.87	13.72	1.14
S8	13.22	12.19	1.03

Although the developed measurement method is also valid for superhydrophobic and real samples, for those samples we have only been able to calculate and correct the contact angle with water. Therefore, we are not able to evaluate the surface energy of these samples without the dispersive component, related to the measurement of the contact angle with the Diiodomethane.

The next step consists in comparing the surface energy values obtained from the developed measurement method by using the S-Neox with the ones directly calculated by the DSA-100.

7.3. Validation of the surface energy calculation

Table 7.3 compares the values of the surface energy evaluated with the measurement method developed in this Ph.D. Thesis and the ones directly calculated by the DSA-100 for the selected hydrophobic samples.

Table 7.3 Comparison between surface energy values corrected by the effect of roughness obtained by the developed measurement method and the ones calculated by the DSA-100.

	Total Surface energy (mN/m)		Dispersive component (mN/m)		Polar component (mN/m)	
Sample	Corrected	DSA-100	Corrected	DSA-100	Corrected	DSA-100
S1	15.45	16.81	14.40	16.08	1.05	0.74
S3	10.89	9.04	10.87	9.02	0.02	0.01
S5	15.62	17.52	15.05	17.24	0.57	0.28
S7	14.87	15.25	13.72	14.17	1.14	1.08
S8	13.22	13.45	12.19	12.34	1.03	1.11

From the comparison of these values of the evaluated surface energy, we can obtain encouraging results although the validation of the evaluation of the surface energy must be made by components as we aware when Wenzel's model was introduced.

Initially, before performing any measurement, we knew that these samples were hydrophobic, in the sense that the water contact angle was larger than 90º. However, being hydrophobic doesn't necessarily mean that the contact angle for dispersive liquids is larger than 90º.

When measuring with water, the contact angles obtained were always larger than 100° in all these samples. The evaluation of the polar component of the surface energy gives as a result a low contribution in the total surface energy. Therefore, if we compare the values of the polar components taking into account the roughness of the surface with the ones directly obtained with the DSA-100, we recognize the behaviour exposed by Wenzel's model; in the hydrophobic regime, not taking into account the roughness of the surface in the calculation of the surface energy means that we are underestimating its value.

On the other hand, when measuring with Diiodomethane, the values of the contact angle were generally smaller than 90°, with the exception of S3. The dispersive component in this case is therefore much larger than the polar component. If we compare the values of the dispersive component of the surface energy taking into account the roughness of the surface with the ones directly calculated by the DSA-100, we can also recognize the

behaviour predicted in Wenzel's model. Since the contact angle is smaller than 90º, not taking into account the roughness would make us overestimate the surface energy values.

Lastly, as Wenzel also predicted, the evaluation of the total surface energy strongly depends on the weight of each component of the surface energy. Since these hydrophobic samples have their two components (polar and dispersive) in a different wetting regime, the general behaviour of the total surface energy cannot be easily predicted, since the effect of one of the components compensates the other.

Therefore, we can validate our developed measurement method in this last step because the evaluation of the components of the surface energy of hydrophobic samples, taking into account the roughness of the surface have been successfully performed since the obtained results fulfil the behaviour predicted by Wenzel.

7.4. Summary

In this last chapter, we have successfully been able to evaluate separately the polar and dispersive components of the surface energy of the previously selected hydrophobic samples with the effect of the roughness of the surface. We performed the evaluation with the contact angles measured with our developed measurement method, with both water and Diiodometahne as measurement liquids, and calculated Young's angle by taking into account the effect of the roughness according to Wenzel's model.

Since we were dealing with hydrophobic samples, the polar component of the surface energy calculated with our method was larger than the value provided by standard commercial calculations that assume smooth surfaces. The dispersive component of the surface energy, on the contrary, was smaller than when calculating it with standard methods, because the contact angles were smaller than 90º and therefore, in a different regime. The global result was that, for these samples of limited roughness, one thing almost compensated the other and the overall effect on the total surface energy was small.

It is worth noting that all the required measurements to get here have been performed with the developed measurement method in this Ph.D. Thesis, using a confocal device to measure both the roughness of the surface and the required parameters to calculate the contact angle and without displacement of the sample between devices since we used a single device.

8. Summary, conclusions and future work

8.1. Summary

There is a big dynamism of the scientific community as well as of the market in the field of surface characterization to overcome the problem that, until recently, there was no available device able to perform topographic and surface energy measurements with a single device.

On the one hand, the scientific community dynamism is captured by the implementation of the European project NATURAL "Standardized metrology of Nano-sTrUctuRed coAtings with Low surface energy" (FP7-NMP-2012-SME-6, 310397) with the goal of develop real world, practical characterization methods for nano-structured coatings with a low surface energy for anti-fouling applications and/or for low friction applications. The characterization methods developed during the project are directly related with the measurement of the surface energy of the coating through the measurement of the contact angle.

On the other hand, the market interest is demonstrated by the development of a new device while this Ph.D. thesis was being carried out, which focuses on the characterization of solid samples through the measurement of both the topography and the surface energy of the surface with the same device. Even so, the solution developed in this Ph.D. Thesis presents some advantages over this competing device; one is that the technique used to perform the topographic measurements is more accurate and the other is that in our solution, there is no displacement of the sample at any time.

This Ph.D. Thesis has presented interesting contributions in the characterization of solid surfaces. The innovation of the Ph.D. Thesis is mainly the development and validation of a new measurement method able to evaluate, with a single device, the surface energy of solid samples through the measurement of the contact angle and the structure of a surface in the same area of the sample. Taking into account that the structure of the surface at the same place where the contact angle is measured is known, the effect of the roughness in the contact angle is corrected according to Wenzel's model.

Although we started to work with interferometry in this Ph.D. Thesis, finally the confocal technique has been presented as a new tool able to correct the effect of the roughness of a hydrophobic surface in the evaluation of the surface energy with water and Diiodomethane as measurement liquids.

8.2. Conclusions

In this Ph.D. Thesis, we developed a new measurement method to measure the surface energy in hydrophobic samples with a single device, based on confocal technology, which incorporates the correction of the effect of the roughness of the surface in the contact angle measurement. We have further validated this technique by comparing the results obtained by measuring different samples with our developed method and with a commercial contact angle meter.

Initially, this Ph.D. Thesis started to develop the measurement method based on the interferometric technique but the initial results stated that interferometry has strong limitations to achieve the goals of this Ph.D. Thesis. For this reason, we changed to the confocal technique, which allowed us to achieve successfully the proposed goals. Therefore, we conclude that:

- *Confocal profilometry is the best option to take into account the roughness of a surface in the measurement of the surface energy.*

A bibliographic and a commercial analysis in the field of contact angles and surface topography measurements has been performed, in which we detected a single, very recent device based on interferometry, to solve the problematic for which this Ph.D. is also addressed. From this study, we conclude that:

- *No commercial device has a fully satisfactory capability to evaluate the surface energy taking into account the roughness of a surface.*
- The theoretical basis for the new measurement methodology has been explained. It allows correcting the effect of the roughness of the surface in the contact angle according to Wenzel's model.

We have developed three different mathematical models to obtain the contact angle from a combination of the width (L) and the height (h) of the drop measured by the confocal device, and the volume of the dispensed drop (V) indicated by the liquid dispenser. Each different model uses a different pair of parameters: (h, L), (h, V) or (L, V).

We have verified the three different mathematical models by evaluating the error introduced in the measurement. This has allowed us to obtain the validity of each method to perform the calculation of the contact angle.

We have developed a measurement strategy to perform contact angle measurements and surface energy evaluations with a commercial contact angle meter.

We have explained the calculation of the surface energy from the previous measurement of the contact angle according to the OWRK method, which is the method used by current commercial contact angle meters to perform the calculation.

We have developed a measurement strategy to perform the measurement of the Developed Interfacial Area Ratio (Sdr) in the same area where the drop will be placed, as well as the measurement of h and L of a liquid drop with the confocal device. L is obtained by measuring the contour of the drop from an image of the entire drop and h is measured

by a dual topography performed at both the apex of the drop and at the surface of the sample.

We have measured using the commercial contact angle meter different sets of hydrophobic, hydrophilic and superhydrophobic samples. The measurement of the contact angles have been performed with the height-width fitting method with water and Diiodomethane as measurement liquids.

The total surface energy values of these three set of samples were also obtained from the automatic calculation performed by the commercial contact angle meter according to the OWRK method, as well as their dispersive and polar components.

We have found some difficulties while measuring with the commercial contact angle meter that can be summarized as follows:

- The measurement of hydrophilic samples is complicated with any technique and fitting method because the low value of the contact angle generates repeatability issues.
- For the set of superhydrophobic samples, the contact angle must be measured using the Young Laplace fitting method because larger volumes are required, implying that the effect of the gravity in the drop must be taken into account.
- For the set of superhydrophobic samples we have only been able to measure the contact angle with water as a measurement liquid because the Diiodomethane spreads completely on the surface. Hence, the evaluation of the surface energy could not be performed for this set if samples.
- The commercial contact angle meter has a restriction on the area of the sample were the drop can be placed, limited to the area adjacent to the edges of the sample. Otherwise, the intersection between the drop and the sample is out of focus and blurred which introduces error to the measurement of the contact angle.

We have measured using our new methodology the same set of hydrophobic, hydrophilic and superhydrophobic samples with both water and Diiodomethane as measurement liquids. The measurements have been performed with a confocal device to obtain Sdr, h and L. The corresponding contact angle values have been calculated with the mathematical model in which only h and L are involved since both parameters can be measured with the confocal device alone.

We have found some difficulties while measuring with the confocal device that can be summarized as follows:

- In the measurement of h and L of drops placed on hydrophilic samples, we must reduce the magnification of the microscope objective up to 2.5X to be able to obtain the entire image of the drop, and up to 5X to measure h by means of the dual topography. Hence, the accuracy of the measurement of h and L is significantly reduced.

- The use of larger drops in order to measure superhydrophobic samples means that the spherical assumption which underlies our developed mathematical methods is not really valid any more, introducing a larger error in the evaluation of the contact angle.

Both measurement strategies were validated by means a repeatability study of the measurements for both devices in samples S3 and S5 (hydrophobic). Therefore, we conclude that:

- *Both measurement strategies have great and equivalent repeatability in the measurement of contact angles for hydrophobic samples.*

With a study of the evolution of the volume of the drop over time performed in a hydrophobic and a hydrophilic sample, with both water and Diiodomethane, we verify that the loss of volume of the drop does not affect the measurements performed by both devices. The maximum volume losses are around 2% of the initial volume when measuring with water in hydrophilic samples with the commercial contact angle meter and of 3% also measuring with water in hydrophilic samples with the confocal device. Therefore, we conclude that:

- *The drop's volume losses in the measurement of the contact angle is equivalent in both measurement strategies and does not affect the measurements.*

The ways of illuminating the liquid drops by both devices have been also demonstrated to not enhance the loss of volume of the liquid drops. The commercial contact angle meter illuminates the drop with backlight and therefore does not contribute to heating the drop. Conversely, the confocal device illuminates directly the liquid drop but there is very little absorption on the part of both water and Diiodomethane of any wavelength of the light source, implying that very little heating takes place. Therefore, we conclude that:

- *The light source does not contribute to the evaporation of the drops when measuring with the confocal device.*

We have compared the contact angles calculated with the parameters provided by the confocal device, comparing them with the ones obtained with the commercial contact angle meter for the three set of samples measured.

We have successfully validated our developed measurement method for the confocal device for the contact angles measured with water in the entire set of hydrophobic samples and partially for the contact angles measured with Diiodomethane.

We have not validated the developed measurement method in the set of hydrophilic samples due to the absence of similarity between the values of the contact angles obtained by both devices.

We have calculated the roughness factor r from the Sdr parameter obtained using the confocal device. This r factor is required to correct the effect of the roughness in the contact angle according to Wenzel's model.

We have corrected the effect of the roughness in the contact angles of a subset of hydrophobic samples (S1, S3, S5, S7 and S8) according to Wenzel's model. . The effect of the roughness of the sample in the contact angle have also been corrected in real samples such as a Photus leaf, a Gerbera's petal and a rose petal.

We have evaluated the dispersive and polar component of the surface energy for samples S1, S3, S5, S7 and S8 according to OWRK's method, taking into account the roughness of the surface and this evaluation have been successfully validated since we have demonstrated the behaviour predicted by Wenzel. Therefore, we conclude that:

- ***The work developed in this Ph.D. Thesis has been able to demonstrate and correct the effect of the roughness in the evaluation of the surface energy of hydrophobic samples by using a single device based on confocal technology.***

8.3. Future work

The future research lines opened by the work presented in this Ph.D. Thesis are:

- Regarding the measurement performed by means the confocal device, different measurement conditions could be studied in order to decrease the loss of volume particularly in hydrophilic samples when measuring with water. Lower the environment temperature or cold down the samples before the measurement could decrease the loss of volume in the time taken to perform the measurements by means the confocal device.
- Regarding the measurement of the contact angle in hydrophilic samples by means the developed measurement method in this Ph.D. Thesis it could be interesting to test the validity of the remaining mathematical models to calculate the contact angle as a function of (h, V) or (L, V) since the mathematical model applied in the validation performed is not the proper one for hydrophilic samples.
- In order not to lose accuracy in the measurement of L of drops placed on hydrophilic samples due to the decrease of the objectives magnification up to 2.5X, the idea to perform an extended image of the drop keeping the 5X magnification was directly eliminated. Since the movement of the sample holder of the confocal device is transferred to the drop between consecutive images, the final image results in a blurred image. It could be useful to provide to the movement of the sample holder of the confocal device with some seconds to allow the drop to be static again at the moment to take the different images.

A. Preliminary results with interferometric technic

During the first year of this Ph.D. Thesis we started to focus our work to develop a device in the field of interferometric technic so we built a first experimental setup and checked some limits of the standard interferometric technique.

This preliminary testing had two principal aims. On the one hand, we wanted to check the adequacy of the proposed system for the measurement of liquid drops profiles with the developed experimental setup. And, on the other hand we tested the adaptations applied in the interferometric device consisting on the use of an afocal system in front of the detector and the use of incoherent light to achieve an interference pattern from which the information to obtain the profile of the drop would be extracted.

The first developed prototype was based on an amplitude division interferometer, in a Twyman-Green configuration [61], [98]. Figure 4.1 shows the system which works by generating an interference pattern coming from the light reflected on two surfaces (measured and reference), which are placed at the output ports of each measurement arm of the device. The light coming from the light source is reflected back by both surfaces and recombined in the detector plane by means of an internal beam splitter. In the case that a liquid drop is placed on one of the surfaces, the resulting interference pattern will be the resulting from light reflected by one of the surfaces and the light reflected by the surface of the liquid drop.

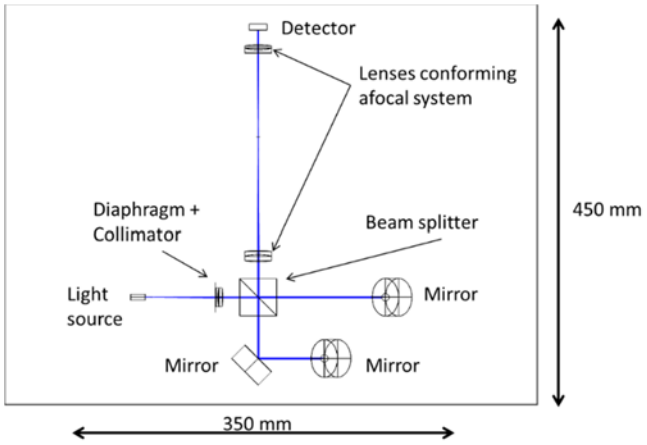

Figure A.1 Schematic representation of the developed system based on a Twyman-Green interferometer in which an afocal system is placed in front of the detector.

The first adaption of the original interferometric system is the addition of an afocal system in the detector arm. This afocal system, placed between the beam splitter and the detector, consists of two doublet achromatic lenses, for which the image focal point of the first doublet is located on the object focal point of the second doublet.

With the addition of this afocal system, we achieve a constant lateral magnification in the detector arm of the system which avoids the work distance dependence if we want to maintain a scale relation between the pixels size of the detector and the real size of the sample. It also allows us to obtain, on the detector plane, the image of the sample surface, combined with the interferogram pattern. The detector used consists of a CMOS Monochrome camera [99], with 2592x1944 (HxV) pixels with sizes of 2.2x2.2 µm and a sensing area of 5.7x4.28 mm.

Figure A.2(a) shows the first prototype of the developed system. To test the assembled device and to perform the first measurements, two flat mirrors placed on a solid plate are used, as Figure A.2(b) shows. One of these mirrors will be use as reference and the other one as sample. One of the reasons for choosing two flat mirrors lies, in first instance, in testing the capability of the prototype to perform interferometric measurements. By using an easy shape as a flat mirror is, a well-controlled interference pattern is obtained.

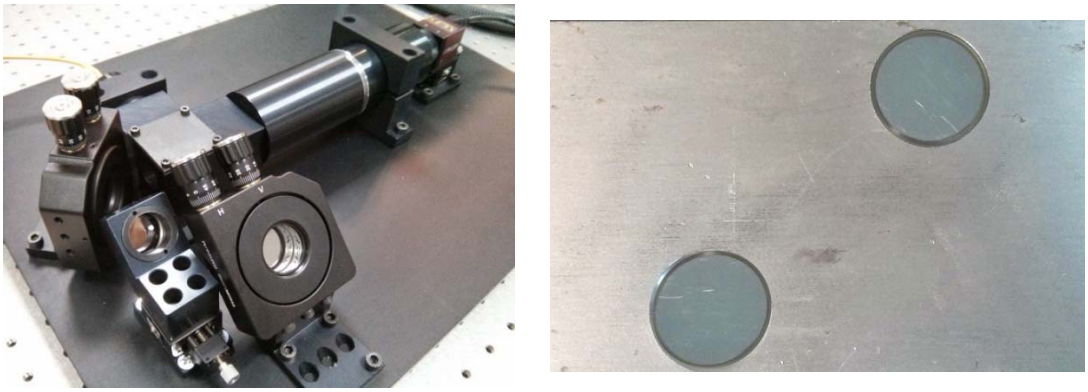

(a) (b)

Figure A.2 (a) Image of the developed experimental setup placed in a platform of 450x350 mm. (b) Flat mirrors, of 25 mm of diameter, used in the measurement a liquid drop profile, both placed in a plate of 75x120 mm.

On the other hand, by placing these mirrors into a solid plate we try to simulate the experimental conditions that the NATURAL project wants to face up to. The measurement process consists on measuring two different areas of the same sample, thereby minimizing the impact of vibrations on the measurement. In this way, we achieve this minimization due to the use of this solid plate to hold the mirrors.

Initially, a coherent light was selected as the light source. More specifically, a fiber-coupled Single Mode Laser Diode [100], with wavelength 635 nm and a bandwidth less than 3 nm, working in continuous wave (CW) mode, in order to achieve a flat enough wave front. To perform the first measurements, both flat mirrors were placed on the exits of the

corresponding arms of the setup and the first interference pattern was obtained, as Figure A.3(a) shows.

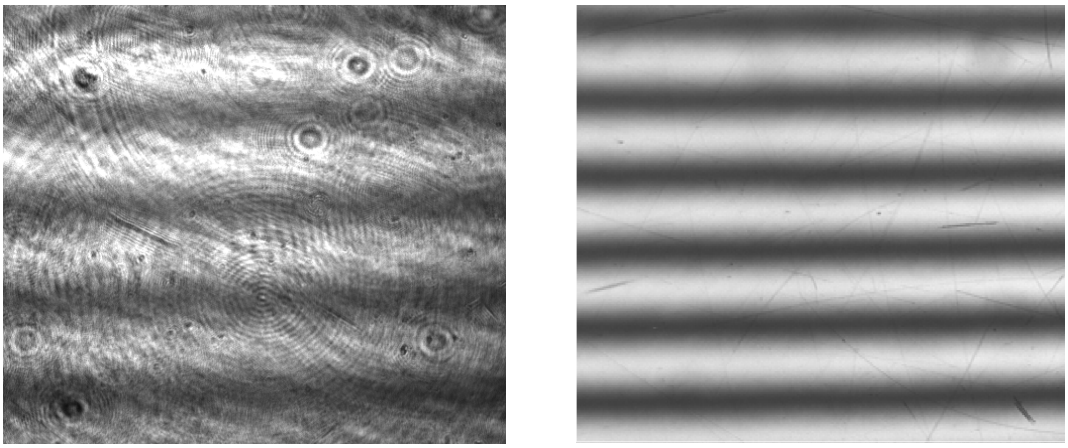

(a) (b)

Figure A.3 5.7x4.28 mm acquired images of the interference pattern created by (a) the superposition of the reflected laser light on the surface of both mirrors; (b) the superposition of the reflected LED light on the surface of both mirrors.

It is clearly seen that the obtained interference pattern, which is composed of horizontal fringes, includes diffractive effects translated into small concentric circular patterns because of the presence of dust particles and also multiple reflections of the light through all the optical parts of the system, which turn into a low contrast circular pattern which covers the entire image.

Due to the fact that these effects do not allow the correct evaluation of the information given by the interference pattern; a second light source was tested. The laser light was replaced by an encapsulated LED source [101], with 626 nm wavelength and a bandwidth of 50 nm. A light diffusor was placed in front of LED in order to achieve uniform illumination on the sample.

Following the same procedure as before, a new interference pattern is obtained and is shown in Figure A.3(b). The differences between both interference patterns are very clear. In this case, a high contrast, uniform fringe pattern is obtained and the explanation comes from the fact that the low coherence of this kind of light sources allows to deal with non-desired diffractive effects.

Indeed, if we compare the coherent length of both light sources obtained from equation (2.17), where λ_0 is the wavelength and $\Delta\lambda$ is the bandwidth, the result is around 3 µm for the LED and around 0.1 mm for the diode laser.

$$\Delta z = l_c \approx 0.44 \cdot \left[\frac{\lambda_0^2}{\Delta\lambda}\right] \tag{A.1}$$

The coherence length gives us an idea of the allowed optical path difference (OPD) between both arms of the setup to achieve interferences. If the OPD is larger than the

coherence length, there will not be any interference pattern from the sample. Therefore, because our light source corresponds to the lowest coherence length, the configuration of the setup requires perfect symmetry in both arms to ensure that the detected optical path differences will be due to the sample under test instead of the interferometer itself.

Regarding the final objective of the NATURAL project, which has the aim of measure the surface energy of a solid surface, it is important to highlight that liquid drops are always involved in the process. The next step was therefore to measure the radius of a liquid drop which is deposited in the field of view of the system. In these conditions, a new interference pattern will be obtained and subsequently analyzed to obtain the value of the radius.

The process starts by placing a liquid drop on one of the mirrors by means of a retractable liquid dispenser. Once the drop is placed in the field of view of the system, the light will illuminate both, the drop and the reference mirror, as Figure A.4(a) shows. It is important to take into account that the light reflected by the surface of the drop will have a specular behaviour as Figure A.4(b) shows.

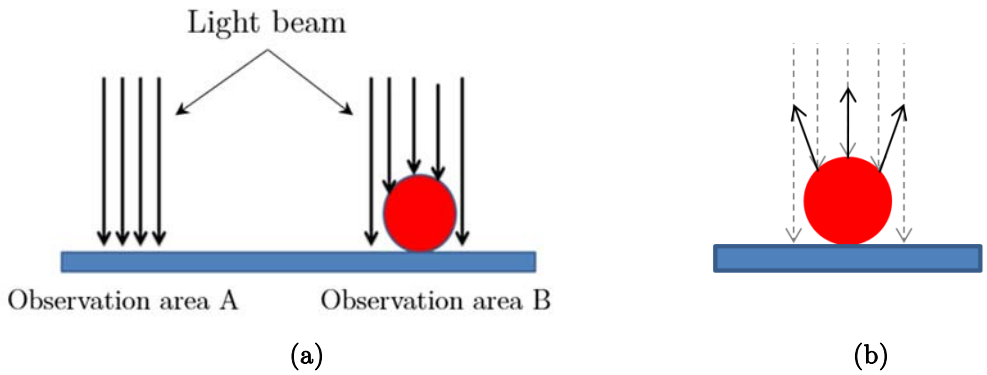

Figure A.4 (a) scheme of how the light illuminates the mirror and the dispensed liquid drop, (a) schematic representation of the reflection of the light by the surface of a liquid drop

This will mean that only a small part of the light will be reflected back into the system and will recombine with the light reflected by the surface of the mirror.

Figure A.5(a) shows the obtained image at this point, in which the interference pattern can be seen together with the disposed drop and only a small part of the drop is illuminated, leaving the rest of the drop as a shadow. The interference pattern corresponds to the recombination of the light coming from both mirrors, as in the previous step, which means that the optical path must be changed to match the same length both for the mirror and for the surface of the drop. Once the length of one of the arms is adjusted, the interference pattern is obtained in the vertex of the drop, at its highest, central point, as Figure A.5(b) shows.

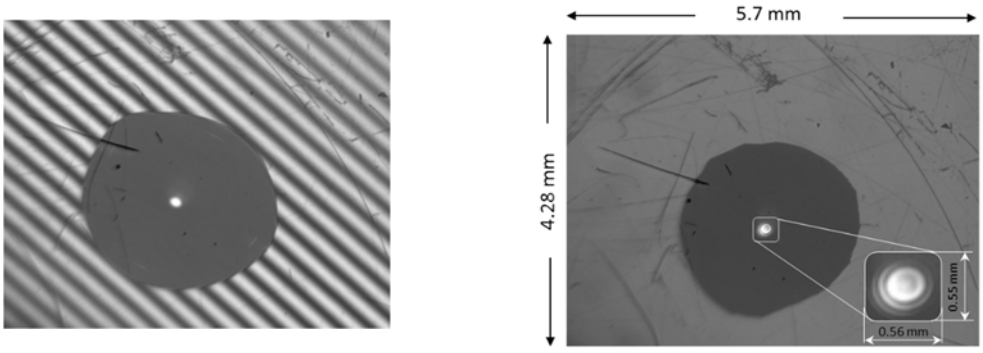

(a) (b)

Figure A.5 (a) 5.7x4.28mm image of the interference pattern created by the light reflected by both mirrors with the liquid drop placed on the field of view; (b) interference pattern created by the light reflected by the upper part of the liquid drop recombined with the light reflected by the reference mirror highlighting the dimensions of the interference pattern.

As can be seen, the area covered by the interference pattern of the drop is about 0.56x0.55 mm which is very small compared to the total image size, 5.7x4.28 mm, and also compared to the dimensions of the drop.

Given that we are performing these first experiments with liquids drops whose volumes are in the microliter scale, we can take advantage of the fact that the influence of gravity is negligible compared to the influence of surface tension and the liquid drop can be approximated as a part of a sphere [102]. With this approximation, the height and the width of the cap of the liquid drop where the interferences take place can be obtained from the interference pattern.

Figure A.6(b) shows the intensity profile along the dotted line of the interference pattern of Figure A.6(a). This intensity profile represents the grey levels of the image between 0 and 255 at each corresponding pixel of the detector.

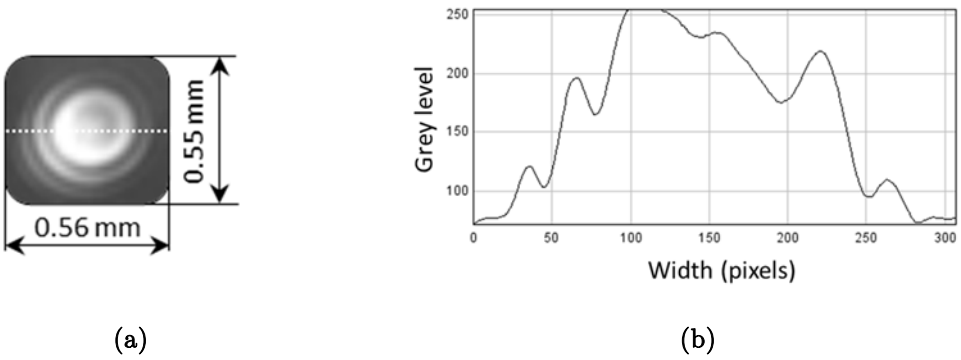

Figure A.6 (a) Magnified image of the interference pattern of the drop; (b) intensity profile obtained along the dotted line in (a).

By analyzing this intensity profile, we can obtain the number of fringes, since the maximums correspond to white fringes and minimums to the black ones. We know that the distance between a black and a white fringe corresponds to $\lambda/2$, therefore, the height of the cap can be easily known by multiplying this value with the obtained number of fringes.

On the other hand, the width of this cap of the liquid drop covered by the interferences can be extracted from the intensity profile by means of the length covered by the interference pattern, since we know the pixel size of the detector.

It is important to highlight that the contrast of this interference pattern is much poorer than the obtained when only the mirrors were used. This will be an important point to work on in the following steps of the thesis.

Once the height and the width of the cap of the liquid drop covered by the interferences are obtained, the spherical cap equation can be applied to the interference pattern to finally obtain the value of the radius of the sphere.

For the present example, which was presented in the OPTOEL 2015 [103] congress, the value of the calculated radius of the sphere is about 0.6 mm. This means that the interference pattern produced by the reflected light on the drop only covers a 0.36% of the total area of the drop, what means that only 30 μm of the drop are used to perform the measurement. This is another point to be improved in the further work of this PhD thesis.

As a summary, from this early testing of the prototype it is easy to conclude that the use of non-coherent light is a key point to achieve clear interference patterns and, on the other hand, the addition of an afocal system in the measurement arm of the device prevent us of incorrect scale interpretation in the image analysis. However, we also have identified that the area covered by the interference pattern in the measurement of the profile of the liquid drop is about 0.36% of the projected drop and the contrast of its interference pattern is not as nice as the previous performed experiments. We therefore conclude that standard interferometric devices are not enough to successfully reach the improvements of the essential components that this Ph.D. Thesis wants to obtain.

B. Detailed mathematical models

In this appendix, we are going to introduce the detailed mathematics to obtain the finals equations to calculate the contact angle from the different sets of parameters introduced in Chapter 4: (h, L), (V, L) and (h, V).

The parameters involved in these equations are depicted in Figure 4.1 where a liquid drop is drawn both in a hydrophilic and in a hydrophobic surface and assumed to be perfectly spherical.

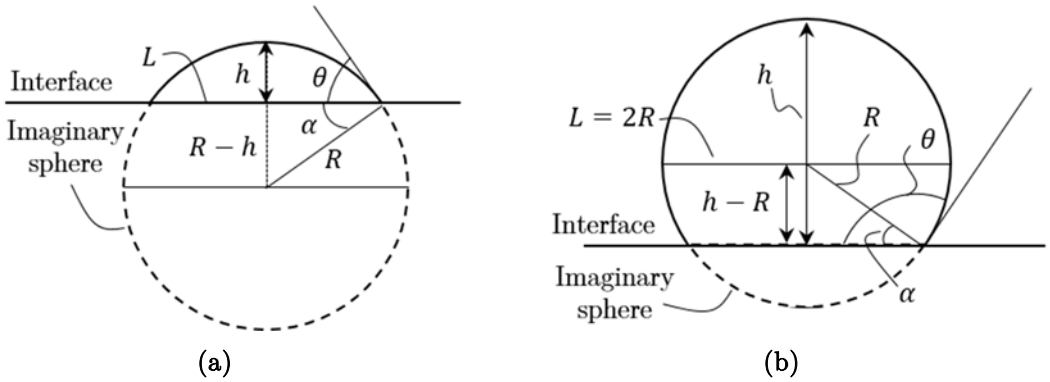

Figure B.1 Schematic representation of a drop placed on a (a) high wettability surface; (b) low wettability surface assuming that it is perfectly spherical, with the parameters involved in the mathematical expressions.

B.1. Contact angle calculation with h and L

In a hydrophilic sample, the relation between θ and α is expressed in equation (B.1).

$$\theta + \alpha = 90° \tag{B.1}$$

The parameters L, h and R follow as well the relation expressed in equation (B.2).

$$(R - h)^2 + \left(\frac{L}{2}\right)^2 = R^2 \tag{B.2}$$

Furthermore, α can be related to R and h as equation (B.3).

$$sin\,\alpha = \frac{R - h}{R} \tag{B.3}$$

Therefore, we can directly relate θ with R and h by isolating α from equation (B.1) and replacing it in equation (B.3), resulting in equation (B.4).

$$cos\,\theta = \frac{R-h}{R} \tag{B.4}$$

As we are interested in the expression that relates θ with the parameters h and L, we can isolate R as a function of h and L from equation (B.2) resulting in equation (B.5),

$$R = \frac{h^2 + \left(\frac{L}{2}\right)^2}{2h} \tag{B.5}$$

and replace (B.5) in (B.4), resulting the final expression to calculate θ by means h and L, measured by the confocal device, stated in equation (B.6).

$$\theta = acos\left(\frac{\frac{L^2}{4} - h^2}{h^2 + \frac{L^2}{4}}\right) \tag{B.6}$$

In a hydrophobic sample, there is a different relation between θ and α, expressed by equation (B.7).

$$\alpha + 90° = \theta \tag{B.7}$$

As in this case, the drop height is larger than its apparent diameter, we can relate L and R by equation (B.8).

$$L = 2R \tag{B.8}$$

Following the previous procedure, we can relate α with R and h, expressed by equation (B.9), to finally obtain the relation of θ with R and h.

$$sin\,\alpha = \frac{h-R}{R} \tag{B.9}$$

Isolating α from equation (B.7) and replacing it in equation (B.9), we obtain equation (B.10).

$$cos\,\theta = \frac{R-h}{R} \tag{B.10}$$

This equation can be restated as a function of R and L is we isolate R from equation (B.8) and we replace it in equation (B.10). Final expression to calculate θ as a function of L and h in a hydrophobic surface is obtained and stated by equation (B.11).

$$\theta = acos\left(\frac{L-2h}{L}\right) \tag{B.11}$$

B.2. Contact angle calculation with h and V

The second mathematical model is based on the calculation of θ as a function of h and L.

As the drop is assumed to be perfectly spherical, we introduced the volume of the spherical cap as equation (B.12) states.

$$V = \frac{\pi h^2}{3}(3R - h) \tag{B.12}$$

In a hydrophilic sample, by isolating R from equation (B.12) and replacing it in equation (B.4), we obtain the expression of θ as a function of both h and V stated by equation (B.13).

$$\theta = acos\left(\frac{3V - 2\pi h^3}{3V + \pi h^3}\right) \tag{B.13}$$

In a hydrophobic sample we obtain the same relation between θ and h and V since we need to relate (B.10), which is essentially (B.4), also with (B.13).

Bibliography

[1] N. Dalili, A. Edrisy, and R. Carriveau, "A review of surface engineering issues critical to wind turbine performance," *Renew. Sustain. Energy Rev.*, vol. 13, pp. 428–438, 2009.

[2] D. Dowson, *History of tribology*. 1998.

[3] B. Bhushan, *Introduction to Tribology*, Second edi. 2013.

[4] KRÜSS, "Surface free energy," 2015. [Online]. Available: http://www.kruss.de/services/education-theory/glossary/surface-free-energy/. [Accessed: 04-Jan-2018].

[5] KYOWA, "Surface tension," 2015. [Online]. Available: http://www.face-kyowa.co.jp/english/en_science/en_theory/en_what_Surface_tension/. [Accessed: 04-Jan-2018].

[6] Purdue University, "Surface tension," 2015. [Online]. Available: https://www.chem.purdue.edu/gchelp/liquids/tension.html. [Accessed: 18-Dec-2015].

[7] M. E. Schrader, "Young- Dupre Revisited," *Langmuir*, vol. 11, no. 9, pp. 3585–3589, 1995.

[8] T. Young, "An Essay on the Cohesion of Fluids," *Philos. Trans. R. Soc. A Math. Phys. Eng. Sci.*, vol. 95, pp. 65–87, 1805.

[9] F. Hejda, P. Solar, and J. Kousal, "Surface Free Energy Determination by Contact Angle Measurements – A Comparison of Various Approaches," *WDS'10 Proc. Contrib. Pap.*, no. 3, pp. 25–30, 2010.

[10] M. Żenkiewicz, "Methods for the calculation of surface free energy of solids," *J. Achiev. Mater. Manuf. Eng.*, vol. 24, no. 1, pp. 137–145, 2007.

[11] L. Wilhelmy, "Ueber die Abhängigkeit der Capillaritäts-Constanten des Alkohols von Substanz und Gestalt des benetzten festen Körpers," *Ann. Phys.*, vol. 195, no. 6, pp. 177–217, 2006.

[12] A. F. Taggart, T. C. Taylor, and C. R. Ince, "Experiments with flotation reagents," *Am. Inst. Min. Metall. Eng.*, vol. 87, no. 285, 1930.

[13] M. Hoorfar & A. W. Neumann, "AXISYMMETRIC DROP SHAPE ANALYSIS

(ADSA) FOR THE DETERMINATION OF SURFACE TENSION AND CONTACT ANGLE," *J. Adhes.*, vol. 80, no. 8, pp. 727–743, 2004.

[14] F. M. Fowkes, "Donor-Acceptor Interactions at Interfaces," *J. Adhes.*, vol. 4, no. 2, pp. 155–159, 1972.

[15] D. K. Owens and R. C. Wendt, "Estimation of the surface energy of polymers," *J. Appl. Polym. Sci.*, vol. 13, no. 8, pp. 1741–1747, 1969.

[16] F. M. Fowkes, "Attractive forces at interfaces," *Ind. Eng. Chem.*, vol. 56, no. 12, pp. 40–52, 1964.

[17] KRÜSS, "Owens, Wendt, Rabel and Kaelble (OWRK) method," 2015. .

[18] Biolin Scientific, "Applications," 2014. [Online]. Available: http://www.biolinscientific.com/attension/applications/?card=AA7. [Accessed: 04-Jan-2018].

[19] T. T. Chau, "A review of techniques for measurement of contact angles and their applicability on mineral surfaces," *Miner. Eng.*, vol. 22, no. 3, pp. 213–219, 2009.

[20] L. Wilhelmy, "Ueber die Abhängigkeit der Capillaritäts-Constanten des Alkohols von Substanz und Gestalt des benetzten festen Körpers," *Ann. Phys.*, vol. 195, no. 6, pp. 177–217, 1863.

[21] KRÜSS, "Wilhelmy plate method," 2015. [Online]. Available: http://www.kruss.de/services/education-theory/glossary/wilhelmy-plate-method/. [Accessed: 04-Jan-2018].

[22] KRÜSS, "Du Noüy ring method," 2015. [Online]. Available: http://www.kruss.de/services/education-theory/glossary/du-nouey-ring-method/. [Accessed: 04-Jan-2018].

[23] P. L. Du Nouy, "New apparatus for measuing surface tension," *J. Gen. Physiol.*, pp. 521–524, 1919.

[24] K. Lunkenheimer and K.-D. Wantke, "Determination of the surface tension of surfactant solutions applying the method of Lecomte du Noüy (ring tensiometer)," *Colloid Polym. Sci.*, vol. 259, no. 3, pp. 354–366, 1981.

[25] W. Harkins and H. Jordan, "A Method for the Determination of Surface and Interfacial Tension from the Maximum Pull on a Ring," *J. Am. Chem. Soc.*, vol. 52, no. 5, pp. 1751–1772, 1930.

[26] H. Fox and C. Chrisman, "The Ring Method of Measuring Surface Tension for Liquids of High Density and Low Surface Tension," *J. Phys. Chem.*, vol. 56, no. 2, pp. 284–287, 1952.

[27] KRÜSS, "Drop Shape Analysis," 2015. [Online]. Available: http://www.kruss.de/services/education-theory/glossary/drop-shape-analysis/.

[Accessed: 04-Jan-2018].

[28] J. J. Bikerman, "A Method of Measuring Contact Angles," *Ind. Eng. Chem. - Anal. Ed.*, vol. 13, no. 6, pp. 443–444, 1941.

[29] G. L. Mack and D. A. Lee, "The Determination of Contact Angles from Measurements of the Dimensions of Small Bubbles and Drops. I. The spheroidal segment method for acute angles," *J. Phys. Chem.*, vol. 40, no. 2, pp. 169–176, 1935.

[30] Face Kyowa, "What is Contact angle?," 2014. [Online]. Available: http://www.face-kyowa.co.jp/english/en_science/en_theory/en_what_contact_angle/. [Accessed: 04-Jan-2018].

[31] A. Bateni, S. S. Susnar, A. Amirfazli, and A. W. Neumann, "A high-accuracy polynomial fitting approach to determine contact angles," *Colloids Surfaces A Physicochem. Eng. Asp.*, vol. 219, no. 1–3, pp. 215–231, 2003.

[32] KRÜSS, "Young-Laplace fit," 2015. [Online]. Available: http://www.kruss.de/services/education-theory/glossary/young-laplace-fit/. [Accessed: 04-Jan-2018].

[33] A. F. Stalder, T. Melchior, M. Müller, D. Sage, T. Blu, and M. Unser, "Low-bond axisymmetric drop shape analysis for surface tension and contact angle measurements of sessile drops," *Colloids Surfaces A Physicochem. Eng. Asp.*, vol. 364, no. 1–3, pp. 72–81, 2010.

[34] X. Zhang, F. Shi, J. Niu, Y. Jiang, and Z. Wang, "Superhydrophobic surfaces: from structural control to functional application," *J. Mater. Chem.*, vol. 18, pp. 621–633, 2008.

[35] C. N. C. Lam, R. Wu, D. Li, M. L. Hair, and a W. Neumann, "Study of the advancing and receding contact angles: liquid sorption as a cause of contact angle hysteresis.," *Adv. Colloid Interface Sci.*, vol. 96, no. 1–3, pp. 169–91, 2002.

[36] A. Marmur, "Thermodynamic aspects of contact angle hysteresis," *Adv. Colloid Interface Sci.*, vol. 50, pp. 121–141, 1994.

[37] L. Gao and T. J. McCarthy, "Contact angle hysteresis explained.," *Langmuir*, vol. 22, no. 14, pp. 6234–6237, 2006.

[38] Face Kyowa, "Extension/contraction method," 2014. [Online]. Available: http://www.face-kyowa.co.jp/english/en_science/en_theory/en_what_contact_angle/#id_01. [Accessed: 04-Jan-2018].

[39] M. Bouteau, S. Cantin, F. Benhabib, and F. Perrot, "Sliding behaviour of liquid droplets on tilted Langmuir-Blodgett surfaces," *J. Colloid Interface Sci.*, vol. 317, no. 1, pp. 247–254, 2008.

[40] E. Ramé, "The Interpretation of Dynamic Contact Angles Measured by the Wilhelmy Plate Method," *J. Colloid Interface Sci.*, vol. 185, no. 1, pp. 245–251, 1997.

[41] M. Żenkienwicz, "Methods for the calculation of surface free energy of solids," *J. Achiev. Mater. Manuf. Eng.*, vol. 24, no. 1, pp. 137–145, 2007.

[42] KRÜSS, "Work of adhesion," 2015. [Online]. Available: http://www.kruss.de/services/education-theory/glossary/work-of-adhesion/. [Accessed: 04-Jan-2018].

[43] C. Della Volpe, D. Maniglio, M. Brugnara, S. Siboni, and M. Morra, "The solid surface free energy calculation: I. In defense of the multicomponent approach," *J. Colloid Interface Sci.*, vol. 271, pp. 434–453, 2004.

[44] D. Li and a. . Neumann, "A reformulation of the equation of state for interfacial tensions," *J. Colloid Interface Sci.*, vol. 137, no. 1, pp. 304–307, 1990.

[45] D. Y. Kwok, C. N. C. Lam, a. Li, K. Zhu, R. Wu, and a. W. Neumann, "Low-rate dynamic contact angles on polystyrene and the determination of solid surface tensions," *Polym. Eng. Sci.*, vol. 38, no. 10, pp. 1675–1684, 1998.

[46] R. J. Good and L. a. Girifalco, "A theory for estimation of surface and interfacial energies.," *J. Phys. Chem.*, vol. 24, no. 13, pp. 561–565, 1960.

[47] D. Y. Kwok and a. W. Neumann, *Contact angle measurement and contact angle interpretation*, vol. 81, no. 3. 1999.

[48] A. . Neumann, R. . Good, C. . Hope, and M. Sejpal, "An equation-of-state approach to determine surface tensions of low-energy solids from contact angles," *J. Colloid Interface Sci.*, vol. 49, no. 2, pp. 291–304, 1974.

[49] C. Rulison, "Two-component surface energy characterization as a predictor of wettability and dispersability," 2000.

[50] S. Wu, "Calculation of interfacial tension in polymers system," *J. Polym. Sci.*, vol. 34, no. 1, pp. 19–30, 1971.

[51] S. Wu, "Polar and Nonpolar Interaction in Adhesion," *J. Adhes.*, vol. 5, no. 1, pp. 39–55, 1973.

[52] R. J. Good and C. J. van Oss, "The Modern Theory of Contact Angles and the Hydrogen Bond Components of Surface Energies," M. E. Schrader and G. I. Loeb, Eds. 1992, pp. 1–27.

[53] R. J. Good, "Contact angle, wetting, and adhesion: a critical review," *J. Adhes. Sci. Technol.*, vol. 6, no. 12, pp. 1269–1302, 1992.

[54] C. J. Van Oss, M. K. Chaudhury, and R. J. Good, "Interfacial Lifshitz-van der Waals and polar interactions in macroscopic systems," *Chem. Rev.*, vol. 88, no. 6,

pp. 927–941, 1988.

[55] C. . Van Oss, R. . Good, and M. . Chaudhury, "The role of van der Waals forces and hydrogen bonds in 'hydrophobic interactions' between biopolymers and low energy surfaces," *J. Colloid Interface Sci.*, vol. 111, no. 2, pp. 378–390, 1986.

[56] W. a. Zisman, "Relation of the Equilibrium Contact Angle to Liquid and Solid Constitution," *Adv. Chem.*, vol. 43, no. 43, pp. 1–51, 1964.

[57] I. Palaci, "Atomic Force Microscopy Studies of Nanotribology and Nanomechanics," ÉCOLE POLYTECHNIQUE FÉDÉRALE DE LAUSANNE, 2007.

[58] UPC, UB, UAB, and ICFO, "Course measuring with light, Master in Photonics." 2014.

[59] Keyence, "ISO 25178." [Online]. Available: https://www.keyence.com/ss/products/microscope/roughness/surface/parameters.jsp. [Accessed: 03-Jan-2018].

[60] P. Hariharan, *Basics of interferometry*, Second. Elsevier Inc., 2007.

[61] D. Malacara, *Optical shop testing*, Third edit. Wiley, 2007.

[62] J. C. Wyant, "White light interferometry," *Proc. SPIE - Int. Soc. Opt. Eng.*, vol. 4737, pp. 98–107, 2002.

[63] R. Windecker, P. Haible, and H. J. Tiziani, "Fast coherence scanning interferometry for measuring smooth, rough and spherical surfaces," *J. Mod. Opt.*, vol. 42, no. 10, pp. 2059–2069, 1995.

[64] J. W. Schmit, K. Creath, and M. Kujawinska, "Spatial and temporal phase-measurement techniques: a comparison of major error sources in one dimension," in *Interferometry: Techniques and Analysis*, 1992, vol. 1755, pp. 202–211.

[65] J. H. Bruning, D. R. Herriott, J. E. Gallagher, D. P. Rosenfeld, a D. White, and D. J. Brangaccio, "Digital wavefront measuring interferometer for testing optical surfaces and lenses.," *Appl. Opt.*, vol. 13, no. 11, pp. 2693–2703, 1974.

[66] J. W. Hardy, J. E. Lefebvre, and C. L. Koliopoulos, "Real-time atmospheric compensation," *J. Opt. Soc. Am.*, vol. 67, no. 3, pp. 360–369, 1977.

[67] J. D. Monnier, "Optical interferometry in astronomy," *Reports Prog. Phys.*, vol. 66, 2003.

[68] J. E. Baldwin and C. a Haniff, "The application of interferometry to optical astronomical imaging.," *Philos. Trans. A. Math. Phys. Eng. Sci.*, vol. 360, no. 1794, pp. 969–986, 2002.

[69] D. Huang, E. A. Swanson, C. P. Lin, J. S. Schuman, W. G. Stinson, W. Chang, M. R. Hee, T. Flotte, K. Gregory, C. A. Puliafito, and et al., "Optical coherence

tomography," *Science (80-.).*, vol. 254, no. 5035, pp. 1178–1181, 1991.

[70] A. F. Fercher, "Optical coherence tomography," *J. Biomed. Opt.*, vol. 1, no. 2, p. 157, 1996.

[71] KRÜSS, "KRÜSS," 2015. [Online]. Available: http://www.kruss.de/. [Accessed: 04-Jan-2018].

[72] KYOWA, "KYOWA," 2015. [Online]. Available: http://www.face-kyowa.co.jp/english/. [Accessed: 04-Jan-2018].

[73] Dyne Testing, "Dyne Testing," 2015. [Online]. Available: http://www.dynetesting.com/. [Accessed: 04-Jan-2018].

[74] Biolin Scientific, "Attension Theta Topography." [Online]. Available: http://www.biolinscientific.com/attension/optical-tensiometers/theta-topography. [Accessed: 04-Jan-2018].

[75] Dyne Testing, "Theta Topography." [Online]. Available: http://www.dynetesting.com/contact-angle-measurement-equipment/contact-angle-with-3d-topography-measurements/. [Accessed: 04-Jan-2018].

[76] Nanovea, "Nanovea," 2015. [Online]. Available: http://nanovea.com/. [Accessed: 04-Jan-2018].

[77] Sensofar, "Sensofar," 2015. [Online]. Available: http://www.sensofar.com/metrology. [Accessed: 04-Jan-2018].

[78] ZYGO, "ZYGO," 2015. [Online]. Available: http://www.zygo.com/. [Accessed: 04-Jan-2018].

[79] Novacam, "Novacam," 2015. [Online]. Available: http://www.novacam.com/. [Accessed: 04-Jan-2018].

[80] Alicona, "Alicona," 2015. [Online]. Available: http://www.alicona.at/home/. [Accessed: 04-Jan-2018].

[81] Olympus, "Olympus," 2015. [Online]. Available: http://www.olympus.es/. [Accessed: 04-Jan-2018].

[82] KLA Tencor, "KLA Tencor," 2015. [Online]. Available: http://www.kla-tencor.com/. [Accessed: 04-Jan-2018].

[83] R. N. Wenzel, "Resistance of solid surfaces to wetting by water," *Ind. Eng. Chem.*, vol. 28, no. 8, pp. 988–994, 1936.

[84] S. Tension, "Solid surface energy data (SFE) for common polymers," 2017. [Online]. Available: http://www.surface-tension.de/solid-surface-energy.htm.

[85] S. Tension, "Surface tension values of some common test liquids for surface energy analysis," 2017. [Online]. Available: http://www.surface-tension.de/index.html.

[Accessed: 14-Nov-2017].

[86] B. D. Cassie and S. Baxter, "Wettability of porous surfaces," *Trans. Faraday Soc.*, vol. 40, no. 5, pp. 546–551, 1944.

[87] Ilovehatephotography, "Gerbera's optical image." .

[88] Wikipedia, "Lotus effect optical image." .

[89] L. Mazzola, E. Bemporad, and F. Carassiti, "An easy way to measure surface free energy by drop shape analysis," *Measurement*, vol. 45, pp. 317–324, 2012.

[90] L. Michigan Metrology, "3D S Parameters - Hybrid parameters." [Online]. Available: https://www.michmet.com/3d_s_hybrid_parameters.htm.

[91] Wikipedia, "Properties of water." [Online]. Available: https://en.wikipedia.org/wiki/Properties_of_water. [Accessed: 21-Dec-2017].

[92] Wikipedia, "Diiodomethane." [Online]. Available: https://en.wikipedia.org/wiki/Diiodomethane. [Accessed: 21-Dec-2017].

[93] Sensofar, "S-Neox."

[94] Wikipedia, "Liquid water absorption spectrum across a wide wavelength range." [Online]. Available: https://commons.wikimedia.org/w/index.php?curid=23793083. [Accessed: 21-Dec-2017].

[95] H. Keller-Rudek, G. K. Moortgat, R. Sander, and R. Sörensen1, "The MPI-Mainz UV/VIS Spectral Atlas of Gaseous Molecules of Atmospheric Interest." [Online]. Available: http://satellite.mpic.de/spectral_atlas/cross_sections/Halogeno-alkanes+radicals/Iodoalkanes(C,H,F,Cl,Br,I)/CH2I2.spc.

[96] H.-Y. Guo, Q. Li, H.-P. Zhao, K. Zhou, and X.-Q. Feng, "Functional map of biological and biomimetic materials with hierarchical surface structures," *RSC Adv.*, vol. 5, no. 82, pp. 66901–66926, 2015.

[97] S. Choo, H. J. Choi, and H. Lee, "Replication of rose-petal surface structure using UV-nanoimprint lithography," *Mater. Lett.*, vol. 121, pp. 170–173, 2014.

[98] C. Pizarro, J. Arasa, F. Laguarta, N. Tomàs, and A. Pintó, "Design of an interferometric system for the measurement of phasing errors in segmented mirrors," *Appl. Opt.*, vol. 41, no. 22, pp. 4562–4570, 2002.

[99] Edmund Optics Inc., "Allied Vision Guppy Pro F-503 1/2.5" CMOS Monochrome Camera," 2014. [Online]. Available: http://www.edmundoptics.com/cameras/firewire-cameras/allied-vision-guppy-pro-firewire-b-cameras/68571/. [Accessed: 04-Nov-2015].

[100] Frankfurt Laser, "FIBER-COUPLED LASER DIODES," 2015. [Online]. Available: http://www.frlaserco.biz/en/products/search/~nm.14~nc.40~did.1~content.29~ope

n.1~tags.48~cid.28/Fiber-Coupled-Laser-Diodes.html#vc=L2VuL3Byb2R1Y3RzL2RldGFpbC9-dHBsLmFqYXh-Y29kZS5GQkxELTYzNS0wLjAwNVctRkM0LUNvYXgvRkJMRC02MzUtMC4wMDVXLUZDNC1Db2F4Lmh0bWxAZGVm.

[101] Avago Technologies, "LED," 2015. [Online]. Available: http://es.farnell.com/avago-technologies/hlmp-eg08-y2000/led-5mm-red-27cd-626nm/dp/1660506?ost=166-0506&categoryIdBox=&selectedCategoryId=&categoryName=Todas+las+categor%C3%ADas&categoryNameResp=Todas+las+categor%C3%ADas. [Accessed: 19-Dec-2015].

[102] J. Chatterjee, "Limiting conditions for applying the spherical section assumption in contact angle estimation," vol. 259, no. 1, pp. 139–147, 2003.

[103] N. Domínguez, J. Arasa, and C. V Garcia, "Uso de interferometría con luz incoherente para la medida del perfil de gotas de agua; resultados preliminares," 2015.

Published work

Patent

Title: Method for measuring the topography and surface energy of a surface of a solid sample by confocal microscope and device for carrying it out.

Public inventors: Pizarro, C., Arasa, J., García, C., Domínguez, N.

Application number: EP16001763

Country: European Union

Applicant: SnellOptics

Journal publications

1. Domínguez, N., Castilla, P., Linzoain, M. E., Durand, G., García, C., Arasa, J., "New approach to the determination of the contact angle in hydrophobic samples with simultaneous correction of the effect of the roughness". Optical Engineering, 2018 (Submitted).

Conferences

1. Domínguez, N., Arasa, J., García, C., "Uso de interferometría con luz incoherente para la medida del perfil de gotas de agua; resultados preliminares". IX Reunión Española de Optoelectrónica, 2015, Salamanca, Spain.
2. Domínguez, N., García, C., Castilla, P., Pizarro, C., Blanco, P., Espínola, M., Arasa, J., "Contact angle calculation for sessile drops with data obtained from top-view measurements". European Optical Society Biennial Meeting (EOSAM), 2016, Berlin, Germany.
3. Domínguez, N., García, C., Castilla, P., Pizarro, C., Blanco, P., Espínola, M., Arasa, J., "Contact angle measurement by means a confocal device". Society of Photo-Optical Instrumentation Engineers (SPIE), 2017, Munich, Germany.
4. Domínguez, N., García, C., Castilla, P., Pizarro, C., Blanco, P., Espínola, M., Arasa, J., "New method for evaluating the surface energy value of rough surfaces with a confocal microscope" Society of Photo-Optical Instrumentation Engineers Photonics Europe (EPE18), 2018 (Submitted).